



Faculty of Science and Technology

MASTER'S THESIS

Study program/ Specialization:

Offshore Technology/ Marine and
Subsea Technology

Spring semester, 2017

Open access

Writer: Artemii A. Sukhov

A handwritten signature in blue ink, appearing to be 'AS', written over a dotted line.

(Writer's signature)

Faculty supervisor: Professor Muk Chen Ong (University of Stavanger)

External supervisor(s): Dr. Jie Wu (SINTEF Ocean)

Thesis title:

VIV Prediction of Steel Lazy Wave Riser

Credits (ECTS): 30

Key words:

VIV, riser, SLWR, fatigue damage,
SINTEF, simulation, sheared current, TDP,
VIVANA, buoyancy element.

Pages: 84

+ enclosure: 6

Stavanger, June 29, 2017

Abstract

Deepwater oil and gas production is complicated by the structural complexity and uncertainty in prediction of the riser's behavior. To date, Steel Lazy Wave Riser (SLWR) has been chosen as one of the most attractive riser designs in deeper waters and harsher environments since its buoyancy part absorbs the motions of the platform/vessel decoupling the Touchdown Point (TDP). When subjected to currents, risers may suffer Vortex-Induced Vibrations (VIV). VIV are caused by alternating shedding of vortices from both sides of the structure. If the frequency of vortex shedding is close to the riser's natural frequency, it may lead to rapid accumulation of bending stresses causing to fatigue damage.

The vortex shedding process for bare and buoyancy part of SLWR is different due to the difference in diameters. Consequently, the VIV responses of the buoyancy section (which consists of the parts of both diameters) will be governed by the interaction of these two processes. The main factors influencing this interaction are the length of buoyancy section, diameter of the buoyancy elements, their arrangement, etc. Thus, there is a strong need to perform VIV analyses for different staggered buoyancy element configurations in terms of the riser fatigue performance.

The riser may oscillate in both Cross-Flow (CF) and In-Line (IL) directions. Most of the riser VIV analyses have been performed in pure CF motions since it was assumed that the IL response's contribution to fatigue damage is insignificant compared to CF one. However, it has been indicated that the IL fatigue damage becomes significant for long cylindrical structures (Baarholm et al., 2006). Thus, in order to consider the contribution from the IL, CF responses and also from their combinations, the VIV analysis including combined CF and IL motions should be performed.

In this thesis, based on the experimentally obtained hydrodynamic data, three different SLWR configurations have been built and analyzed using the VIV prediction program VIVANA. Since the vortex shedding frequency behavior around the structure is uncertain, there are two options to determine the excitation zones used in this program. Their principles are based on the following assumptions: frequencies act on the structure concurrently (space sharing option) or consequently (time sharing option).

With reference to the above mentioned, the following analyses have been performed in the present work:

- Investigation of sensitivity of different buoyancy element configurations on the CF fatigue damage;
- Investigation of the combined CF and IL prediction for the base case configuration;
- Investigation of the space sharing and time sharing options for all configurations.

As a result, all the analyses have been successfully performed; some key findings are listed below:

- The sensitivity analysis results have shown an insufficient fatigue performance of two SLWR configurations with staggered buoyancy elements due to the high bending stresses in the buoyancy sections;
- In the base case VIV analysis with combined CF and IL motions (using both uniform and sheared current profiles), the fatigue damage calculated at 45, 135 and 180 (IL) degrees to the flow direction was dominating for some of the cases;
- The fatigue damage results obtained using the space sharing option, have been generally bigger compared to the time sharing case.

In the present work, all obtained results have been stated and discussed; recommendations for further work have been also given.

Acknowledgements

I am grateful to all people who contributed to my master's thesis.

First of all I want to thank Professor O.T. Gudmestad and Professor A.B. Zolotukhin for establishment of this double-degree program, which gave me an inestimable experience of studying abroad.

I would like to say thank you to my supervisor and Professor Muk Chen Ong (UiS) for his patience and motivation during writing of my thesis.

I am very thankful to Dr. Jie Wu (SINTEF Ocean, Trondheim, Norway) for his priceless support, for giving new ideas to me and providing the important literature and data for my thesis.

Also I want to say a thousand thanks to MSc student Malakonda Reddy Lekkala for his great help and sharing the essential knowledge with me.

I am endlessly thankful to my amazing parents for their motivation, love and support during my studying abroad.

Also I am very grateful to all my friends for their encouragement, for being with me in a rough time, this work would be impossible without you.

Last but not least, thanks to Norway, for being such a wonderful and inspiring country.

Contents

Abstract	2
Acknowledgements	4
Contents	5
List of Figures	7
List of Tables	9
Nomenclature	10
1 Introduction	13
1.1 Background and motivation.....	13
1.2 Steel lazy wave riser.....	14
1.3 Objectives.....	16
2 Literature study	17
2.1 VIV theory.....	17
2.1.1 Mechanism of VIV.....	17
2.1.2 Key parameters.....	18
2.1.3 Lock-in.....	22
2.2 VIV investigation methods.....	23
2.2.1 Numerical investigations.....	23
2.2.2 Model tests.....	24
2.3 SLWR investigations.....	32
2.3.1 Buoyancy elements interaction with riser.....	32
2.3.2 Riser-seafloor interaction.....	34
2.4 Combined IL and CF response.....	36
3 Computer-based VIV prediction program VIVANA	39
3.1 Introduction.....	39
3.2 Hydrodynamic force coefficients.....	40
3.2.1 Added mass coefficients.....	40
3.2.2 Excitation and damping coefficients.....	42
3.3 Frequency response method.....	45
3.4 Time sharing and space sharing.....	46
3.4.1 Space sharing.....	47
3.4.2 Time sharing.....	48

4	VIV analysis of a typical deepwater SLWR	49
4.1	The riser model.....	50
4.2	The soil model.....	52
4.3	Analysis results for uniform flow.....	52
4.3.1	Response frequencies and mode numbers.....	53
4.3.2	Response amplitudes.....	53
4.3.3	Fatigue damage.....	57
4.4	Analysis results for non-uniform flow.....	59
5	Sensitivity study: different buoyancy element arrangement	63
5.1	Hydrodynamic data acquisition.....	63
5.2	Riser models with staggered buoyancy elements.....	65
5.2.1	Static configurations.....	66
5.3	Fatigue damage analysis.....	68
5.3.1	First SLWR configuration.....	68
5.3.2	Second SLWR configuration.....	70
5.3.3	Fatigue damage comparison.....	73
6	Results and discussion	75
6.1	Discussion of the base case analysis.....	75
6.1.1	Increase of the IL fatigue damage.....	75
6.1.2	Influence of the Strouhal number on the response frequency and mode number.....	76
6.2	Discussion of the sensitivity study.....	78
6.2.1	Maximum fatigue damage variations.....	78
6.2.2	Maximum fatigue in the buoyancy section and at TDP.....	79
7	Conclusion and recommendations for future work	80
	References	82
	Appendix A. Input files	86
	Appendix B. Working files	86
	Appendix C. Hydrodynamic data	87
	Appendix D. Current data	90

List of Figures

Figure 1.1 A typical view of SLWR (Retrieved from: https://en.bardotgroup.com/).....	13
Figure 1.2 An example configuration of SLWR (Li and Nguyen, 2010).....	15
Figure 1.3 TDP movement comparison between SCR and SLWR (Cheng and Cao, 2013)	15
Figure 2.1 Staggered alternate vortex shedding: IL and CF response (Kenny, 1993).....	17
Figure 2.2 Classical vortex patterns behind a fixed cylinder (Sumer and Fredsøe, 2006)...	19
Figure 2.3 Relationship between Strouhal number and Reynolds number for circular cylinders (Lienhard, 1966; Achenbach and Heinecke, 1981).....	20
Figure 2.4 Non-dimensional amplitude versus reduced velocity for three cylinders with different weight (Vikestad, 1998).....	22
Figure 2.5 Lock-in or synchronization of vortex shedding cross-flow oscillations, added mass is assumed to follow the VIVANA model (Larsen et al., 2002).....	23
Figure 2.6 Free oscillation test set-up (Larsen, 2011).....	24
Figure 2.7 Added mass as function of the reduced velocity (Vikestad, 1998).....	25
Figure 2.8 Time history for the oscillating cylinder with A/D=0 initial condition (Larsen, 2011).....	26
Figure 2.9 Time history for the cylinder with high A/D initial condition (Larsen, 2011)...	26
Figure 2.10 Forced oscillation test set-up (Larsen, 2011).....	27
Figure 2.11 Overview of the test setup (Braaten and Lie, 2005).....	28
Figure 2.12 Test rig sketch (Braaten and Lie, 2005).....	29
Figure 2.13 Clump weight and heave compensator (Braaten and Lie, 2005).....	30
Figure 2.14 Riser instrumentation: a) strain gouge and b) accelerometer (Braaten and Lie, 2005).....	30
Figure 2.15 Maximum of temporal displacement standard deviation: a) for uniform flow and b) for sheared flow (Trim et al., 2005).....	31
Figure 2.16 Staggered buoyancy configurations over the riser (Rao et al., 2015).....	33
Figure 2.17 Response frequencies associated with bare part and buoyancy part respectively for five configurations (Rao et al., 2015).....	34
Figure 2.18 Illustration of models for riser/seafloor interaction (Larsen and Passano, 2006).....	35
Figure 2.19 Displacement orbits associated with different values of θ (Shi et al., 2010)...	36
Figure 3.1 Contour plot of the CF added mass coefficients based on forced motions (Gopalkrishnan, 1993).....	40
Figure 3.2 VIVANA model for added mass as a function frequency for CF response (Passano et al., 2014).....	41
Figure 3.3 Contour plot of the IL added mass coefficients (Aronsen, 2007).....	41
Figure 3.4 VIVANA model for added mass as a function of frequency for IL response (Passano et al., 2014).....	42
Figure 3.5 Contour plot curves for the CF excitation coefficient (Gopalkrishnan, 1993)...	43
Figure 3.6 Contour plot curves for the IL excitation coefficient (Gopalkrishnan, 1993)....	43
Figure 3.7 The CF excitation force coefficient curve defined from three points (Passano et al., 2014).....	44
Figure 3.8 The in-line excitation force coefficient curve defined from 3 points, pure IL response (Passano et al., 2014).....	44
Figure 3.9 Parameters to define specific excitation coefficient curves for CF response analysis (Passano et al., 2014).....	45
Figure 3.10 Space sharing process (Passano et al., 2014).....	47

Figure 3.11 Illustration of the time sharing process (Passano et al., 2014).....	48
Figure 3.12 Excitation zones according the time sharing process (Passano et al., 2014)....	48
Figure 4.1 Points around the riser's circumference for fatigue calculation.....	50
Figure 4.2 Steel lazy wave riser configuration modelled in VIVANA (static shape).....	51
Figure 4.3 Monolithic buoyancy module for the base case analysis.....	52
Figure 4.4 CF response amplitudes (space sharing).....	54
Figure 4.5 IL response amplitudes (space sharing).....	54
Figure 4.6 CF response amplitudes of bare part (time sharing).....	54
Figure 4.7 CF response amplitudes of buoyancy part (time sharing).....	55
Figure 4.8 Maximum CF response amplitudes (time sharing).....	55
Figure 4.9 IL response amplitudes of bare part (time sharing).....	56
Figure 4.10 IL response amplitudes of buoyancy part (time sharing).....	56
Figure 4.11 Maximum IL response amplitudes (time sharing).....	57
Figure 4.12 Accumulated fatigue damage for the space sharing method.....	57
Figure 4.13 Accumulated fatigue damage for the time sharing method.....	58
Figure 4.14 Realistic non-uniform current profiles (Wu et al., 2017).....	59
Figure 4.15 Accumulated CF and IL fatigue damage for the space sharing option (including probabilities of occurrence).....	60
Figure 4.16 Accumulated CF and IL fatigue damage for the time sharing option (including probabilities of occurrence).....	60
Figure 4.17 Maximum fatigue damage comparison for the space sharing option (excluding probabilities of occurrence).....	61
Figure 4.18 Maximum fatigue damage comparison for the time sharing option (excluding probabilities of occurrence).....	62
Figure 5.1 Test configurations (Wu et al., 2017).....	64
Figure 5.2 Design excitation coefficient curves (Wu et al., 2017).....	65
Figure 5.3 The main parameters of the riser configurations (Wu et al., 2016).....	66
Figure 5.4 Riser static configurations.....	67
Figure 5.5 The 1 st riser configuration modelled in VIVANA.....	68
Figure 5.6 Accumulated fatigue damage comparison between the time and space sharing options for the 1 st SLWR configuration (including probabilities of occurrence).....	69
Figure 5.7 Maximum fatigue damage comparison for the 1 st configuration using the space sharing method (current are without probabilities of occurrence).....	70
Figure 5.8 Maximum fatigue damage comparison for the 1 st configuration using the time sharing method (current are without probabilities of occurrence).....	70
Figure 5.9 The 2 nd riser configuration modelled in VIVANA.....	71
Figure 5.10 Accumulated fatigue damage comparison between the time and space sharing options for the 2 nd SLWR configuration (including probabilities of occurrence)...	71
Figure 5.11 Maximum fatigue damage comparison for the 2 nd configuration using the space sharing method (current are without probabilities of occurrence).....	72
Figure 5.12 Maximum fatigue damage comparison for the 2 nd configuration using the time sharing method (current are without probabilities of occurrence).....	72
Figure 5.13 CF fatigue damage comparison between the base case, 1 st and 2 nd SLWR configurations against the riser arc length using the space sharing method.....	73
Figure 5.14 CF fatigue damage comparison between the base case, 1 st and 2 nd SLWR configurations against the riser arc length using the space sharing method.....	74
Figure 6.1 Strouhal number values along the riser for first 6 current profiles.....	77
Figure 6.2 Strouhal number values along the riser for points from 7 th to the 21 st profile...	77

List of Tables

Table 2.1 Main test parameters (Braaten and Lie, 2005).....	29
Table 4.1 Riser model properties.....	51
Table 4.2 Soil model properties (SINTEF Ocean Company).....	52
Table 4.3 Fatigue damage results for combined CF and IL case.....	58
Table 5.1 Riser and buoyancy element properties (Wu et al., 2017).....	64
Table 5.2 Summarized input parameters (Wu et al., 2017).....	65
Table 5.3 Arrangement of the buoyancy elements.....	67
Table 5.4 Accumulated CF fatigue damage results.....	73
Table 6.1 Key results of selected cases for the analysis (space sharing option).....	75
Table 6.2 Key analysis results for the space sharing option.....	76
Table 6.3 VIV data for the analysis (space sharing option).....	78
Table 6.4 VIV data for the analysis (time sharing option).....	79
Table C.1 Excitation zone properties.....	87
Table C.2 Added mass properties.....	87
Table C.3 Excitation coefficient properties for the base case.....	88
Table C.4 Excitation coefficient properties for the bare part of the 1 st configuration.....	88
Table C.5 Excitation coefficient properties for the buoyancy part of the 1 st configuration.....	89
Table C.6 Excitation coefficient properties for the bare part of the 2 nd configuration.....	89
Table C.7 Excitation coefficient properties for the buoyancy part of the 2 nd configuration.....	89
Table D.1 Realistic current profiles.....	90

Nomenclature

Abbreviations

VIV	Vortex Induced Vibrations
SLWR	Steel Lazy Wave Riser
SCR	Steel Catenary Riser
TDP	Touchdown Point
VIVANA	Vortex Induced Vibrations Analysis Program
HPHT	High Pressure High Temperature
API	American Petroleum Institute
DNV	Det Norske Veritas
IL	In-Line
CF	Cross-Flow
FDM	Finite Difference Method
FEM	Finite Element Method
FVM	Finite Volume Method
CFD	Computational Fluid Dynamics
NDP	Norwegian Deepwater Programme
RIFLEX	Static and Dynamic Analysis Program for Slender Marine Structures
RMS	Root Mean Square
MARINTEK	Norsk Marinteknisk Forskningsinstitutt
SINTEF	Selskapet for Industriell og Teknisk Forskning
NTNU	Norges Teknisk-Naturvitenskapelige Universitet

Roman symbols

Re	Reynolds number
St	Strouhal number
V_r	Reduced velocity
\hat{f}	Non-dimensional frequency

k	Surface roughness
D	External diameter of cylinder
m	Mass per unit length
$\left(\frac{A}{D}\right)_{IL/CF}$	Amplitude ratio for IL or CF
U	Flow velocity
f_v	Vortex shedding frequency
f_0	Natural frequency
m_{a0}	Added mass in still water
f_{osc}	Oscillation frequency
C_e	Excitation coefficient
EI	Bending stiffness
EA	Axial stiffness
G	Shear stiffness
E	Young modulus
L_B	Length of buoyancy element
L_C	Length between two near-by buoyant parts
$F_{e,IL/CF}$	Excitation force for IL or CF direction
$\left(\frac{A}{D}\right)_{C_e=0}$	Amplitude when excitation is equal to zero
M	Mass matrix
C	Damping matrix
K	Stiffness matrix
R	External load
\ddot{i}	Acceleration
\dot{i}	Velocity
r	Displacement
M_H	Hydrodynamic mass matrix
X	Load vector
M_S	Structural mass matrix
C_H	Hydrodynamic damping matrix
C_S	Structural damping matrix
x	Response vector
E_i	Excitation parameter

U_N	Flow speed normal to the structure
D_H	Hydrodynamic diameter
s	Coordinate along the riser
$L_{e,i}$	Candidate frequency
E_n	Excitation parameter for frequency n
N	Amount of cycles
S	Stress amplitude
m	Slope of the SN curve
c_i	Current profile
$P(c_i)$	Probability of occurrence for each current profile
L	Riser length
L/D	Aspect ratio
D_b	Buoyancy element outer diameter
D_r	Bare riser outer diameter
C_a	Added mass coefficient

Greek symbols

ρ	Density
ν	Kinematic viscosity
μ	Dynamic viscosity
π	3.14159
θ	Phase angle
ω	Load frequency

Chapter 1

Introduction

1.1 Background and motivation

Oil and gas production in deep and ultra-deep water depths creates many issues, such as the design of reliable and economically efficient riser systems. For most of the deepwater riser systems acting in zones with harsh current conditions, such as the Norwegian Sea, Gulf of Mexico etc., VIV is the main design challenge. Strong current can create vortex-induced vibrations that cause to rapid riser fatigue damage accumulation. With increased water depth, riser designs become more complicated; and riser engineers face a lot of uncertainties of VIV behavior determination (Trim et al., 2005).

In recent years, a big number of various riser solutions have been designed. In terms of great depth and severe environment, the most preferable riser concept nowadays is the steel lazy wave riser. Design of SLWR is similar to Steel Catenary Riser (SCR). The only difference is that the SLWR is equipped with the special buoyancy elements, which makes the middle part to be suspended forming the arch. This riser solution has been proven its advantages over SCR, specifically better fatigue performance, decreased hang-off payload and the less bending stresses accumulation at TDP. The typical SLWR design is shown in Figure 1.1.

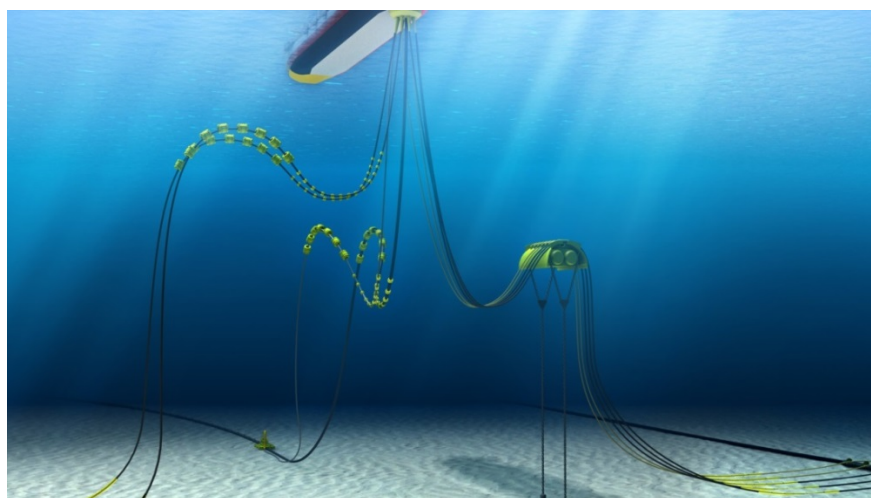


Figure 1.1 A typical view of SLWR (Retrieved from: [https://en.bardotgroup.com/collections/surf-packages-a-global-offer-epc.](https://en.bardotgroup.com/collections/surf-packages-a-global-offer-epc))

A great scope of experimental and numerical investigations has been performed over SLWR (Lie et al., 2012; Li et al., 2011). Prediction of riser responses has been made using the semi-empirical VIV examination tools such as VIVANA (Wu et al., 2016). However, due to the complexity of the buoyancy section of SLWR, that part of a riser becomes critical when experiencing VIV. Moreover, VIV investigations of the touchdown area of SLWR, including pipe-seafloor interaction have not been thoroughly studied yet. These aspects have formed the motivation of the present work. This thesis is devoted to detailed VIV analysis of the buoyancy and touchdown sections of SLWR including the sensitivity study of different buoyancy element arrangement and pipe-seafloor interaction models.

1.2 Steel lazy wave riser

Steel catenary riser is the common type of marine risers in offshore industry, which connects production (drilling) facility with subsea equipment and transfers hydrocarbons from seafloor to the platform. SCRs are widely used among offshore operators especially in deepwater due to their cost-effectiveness, good performance in High Pressure and High Temperature (HPHT) and sour service conditions, relative simplicity and robustness. Design of SCR is performed in accordance with the American Petroleum Institute (API) or Det Norske Veritas (DNV) guidelines. However, as water depth becomes deeper, SCRs are faced with the following design issues (Cheng and Cao, 2013):

- Riser compression at the Touch Down Point (TDP) due to the increased weight;
- Over payload at the hang-off point of the vessel;
- Sensitivity of SCRs to the vessel's heave motion (coupled system);
- As a result, significant TDP movement which leads to increased bending stresses and strength loss.

All these factors may cause significant environmental problems such as an oil spill in consequence of the riser failure.

To mitigate these issues, SLWRs have been designed. The main distinctive feature of SLWR is the set of attached buoyancy modules on a middle section of a riser. This set of BMs gives an additional lifting force which makes the intermediate part of riser suspended in water. According to (Li and Nguyen, 2010), this buoyancy force is around twice higher than the submerged weight of the bare riser part with buoyancy modules including the internal fluid. As shown in Figure 1.2, the typical construction of SLWR includes three parts: hang-off catenary, the buoyancy catenary, and the touchdown catenary.

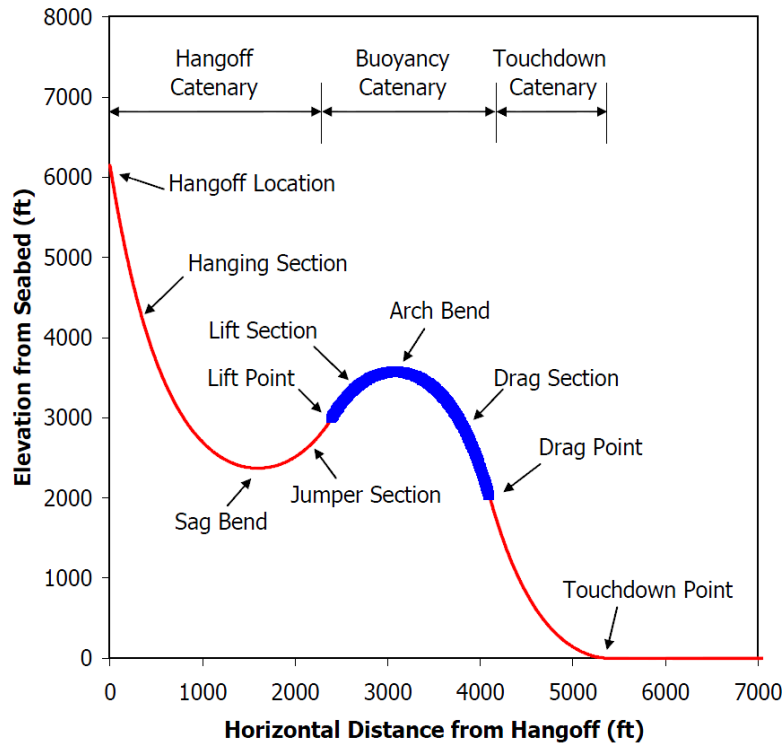


Figure 1.2 An example configuration of SLWR (Li and Nguyen, 2010)

The comparison between SCR and SLWR has been performed by Cheng and Cao, 2013. The aim of their research was to estimate the decoupling efficiency of the SLWR by using the TDP shift against the horizontal and vertical hang off point movement. The less TDP moves, the more efficient the system is. Figure 1.3 illustrates the TDP movement of SLWR in contrast with SCR. The same water depths and riser departure angles have been taken for this analysis. The line slope defines the shift of TDP per unit offset. It is seen that the SCR has significantly bigger TDP movement than the SLWR. Another important observation is that TDPs in both cases are more influenced by heave motions rather than surge motions.

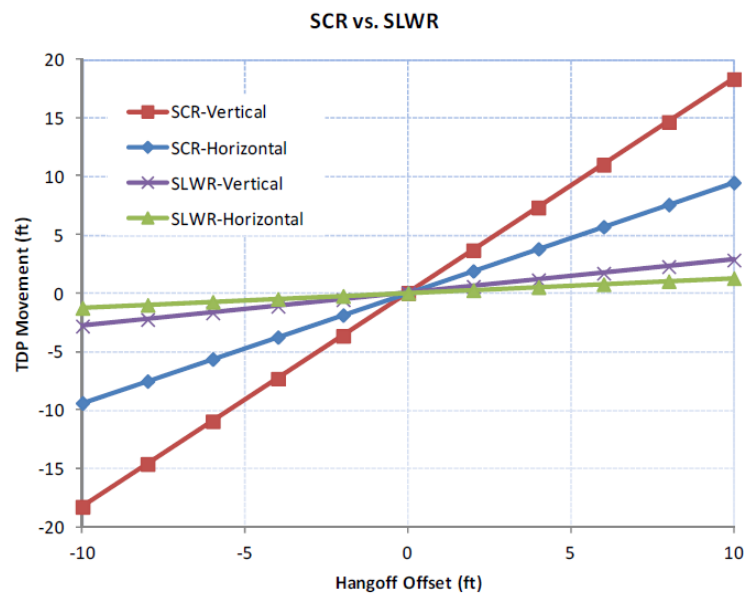


Figure 1.3 TDP movement comparison between SCR and SLWR (Cheng and Cao, 2013)

It has been also shown that with increased length of buoyancy part as well as with deeper equivalent riser payload water depth (distance from the hang off location to the riser sag bend, see Figure 1.2), the SLWR shows better decoupling efficiency: the TDP movement is decreased leading to increased fatigue life of the riser touch down region.

However, this study does not include the detailed VIV analysis of SLWR and riser interaction with different soils has not been considered as well. According to Larsen and Passano (2006), in most cases, the maximum bending stresses in SCRs from VIV are observed at touch down area. Consequently, the riser fatigue life must also be dependent on the seabed properties, and qualitative pipe-seafloor interaction model is, hence, required. Since the design of SLWR is similar to SCR (disregarding the buoyancy section), there is a strong need to perform the VIV analysis of the SLWR considering the pipe-soil interaction. This analysis will check the robustness of the SLWR.

1.3 Objectives

This master's thesis is devoted to the detailed analysis and discussion of the aspects concerning the deepwater SLWR and it includes the following analyses:

- VIV analysis of deepwater SLWRs using VIVANA semi-empirical program: to simulate the behavior of SLWR subjected to VIV. As a result, response frequencies and amplitudes, mode numbers and fatigue damage along the riser will be obtained;
- Investigation of the buoyancy element and bare riser interaction: to perform a sensitivity study of the different buoyancy elements arrangement in terms of the riser fatigue life;
- Investigation of the soil-riser interaction at TDP: to perform a VIV analysis taking into consideration riser-soil interaction (elastic spring model will be considered in this thesis). As a result, more realistic picture of bending stresses near TDP will be obtained;
- Investigation of the combined IL and CF response of SLWR: to perform the VIVANA analysis considering combined IL and CF response of long deepwater riser to obtain total hydrodynamic forces acting on the riser in both directions.
- Comparison of two different excitation zone identification methods in VIVANA: space sharing and time sharing. The results will be explained in terms of the maximum fatigue damage.

Chapter 2

Literature study

2.1 VIV theory

VIV is a widely occurring phenomenon in various industrial practices dealing with long flexible structures: chimneys, mooring anchors and marine risers. It is significant design issue for such structures because these vibrations can lead to big oscillations and fatigue breakdown.

2.1.1 Mechanism of VIV

When the fluid passes a submerged blunt cylindrical body, it creates vortices downstream of it. These vortices are shed periodically from either side of the body and result in a Von Karman vortex street (see Figure 2.1). The harmonic load developed from the alternatively shedding induces vibrations with the same frequency as the frequency of the vortex shedding. After being shed, the regular pattern of vortices moves further downstream with subsequent dissipation of the energy. The interaction between vortices and the cylinder is called vortex-induced vibration (Sumer and Fredsøe, 2006).

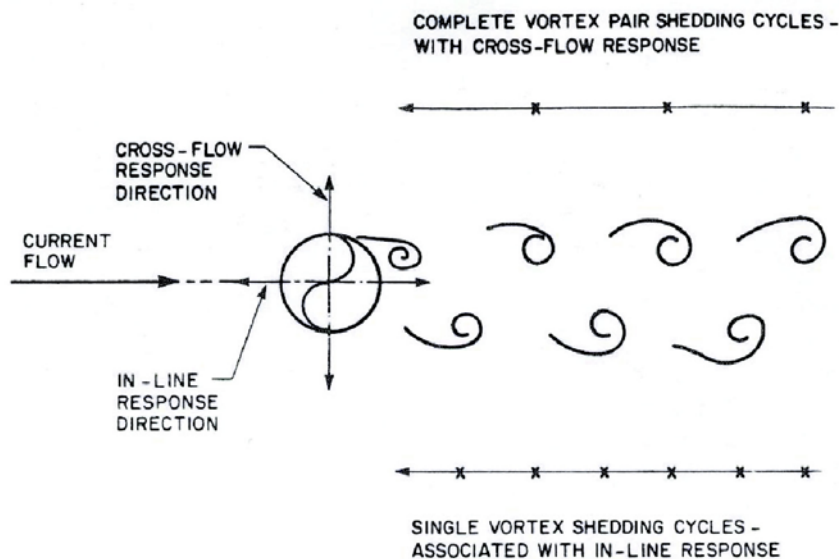


Figure 2.1 Staggered alternate vortex shedding: IL and CF response (Kenny, 1993)

2.1.2 Key parameters

There are several parameters which are used to characterize the process of vortex-induced vibrations:

- Reynolds number, Re ;
- Strouhal number, St ;
- Reduced velocity, V_r ;
- Non-dimensional frequency, \hat{f} ;
- Roughness ratio, $\frac{k}{D}$;
- Mass ratio, $\frac{m}{\rho D^2}$;
- Non-dimensional displacement amplitude ratio, $\frac{A}{D}$.

Reynolds number

Reynolds number is represented by relation of inertia and friction forces acting on a body. It defines the vortex pattern for various flow regimes.

$$Re = \frac{\text{inertia force}}{\text{friction force}} = \frac{UD}{\nu} = \frac{UD\rho}{\mu}, \quad (2.1)$$

where U – flow velocity, D – characteristic size of the structure (in case of cylindrical body, D is its diameter), ν , μ are kinematic and dynamic viscosities correspondingly, ρ is the fluid density.

Classification of different flow regimes and vortex patterns is shown in Figure 2.2.

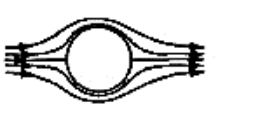


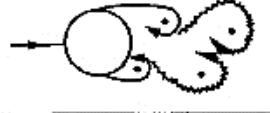
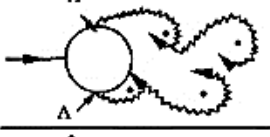
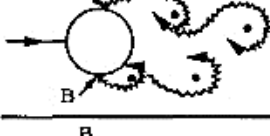
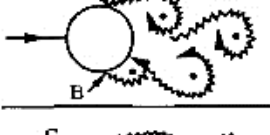

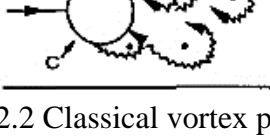
	No separation. Creeping flow	$Re < 5$
	A fixed pair of symmetric vortices	$5 < Re < 40$
	Laminar vortex street	$40 < Re < 200$
	Transition to turbulence in the wake	$200 < Re < 300$
	Wake completely turbulent. A: Laminar boundary layer separation	$300 < Re < 3 \times 10^5$ Subcritical
	A: Laminar boundary layer separation B: Turbulent boundary layer separation; but boundary layer laminar	$3 \times 10^5 < Re < 3.5 \times 10^5$ Critical (Lower transition)
	B: Turbulent boundary layer separation; the boundary layer partly laminar partly turbulent	$3.5 \times 10^5 < Re < 1.5 \times 10^6$ Supercritical
	C: Boundary layer comple- tely turbulent at one side	$1.5 \times 10^6 < Re < 4 \times 10^6$ Upper transition
	C: Boundary layer comple- tely turbulent at two sides	$4 \times 10^6 < Re$ Transcritical

Figure 2.2 Classical vortex patterns behind a fixed cylinder (Sumer and Fredsøe, 2006)

Strouhal number

The Strouhal number is non-dimensional parameter and it defines the vortex shedding frequency of a fixed cylinder.

$$St = \frac{f_v D}{U}, \quad (2.2)$$

where f_v is the vortex shedding frequency for a fixed cylinder.

Strouhal number varies significantly for different values of Reynolds number (see Figure 2.3).

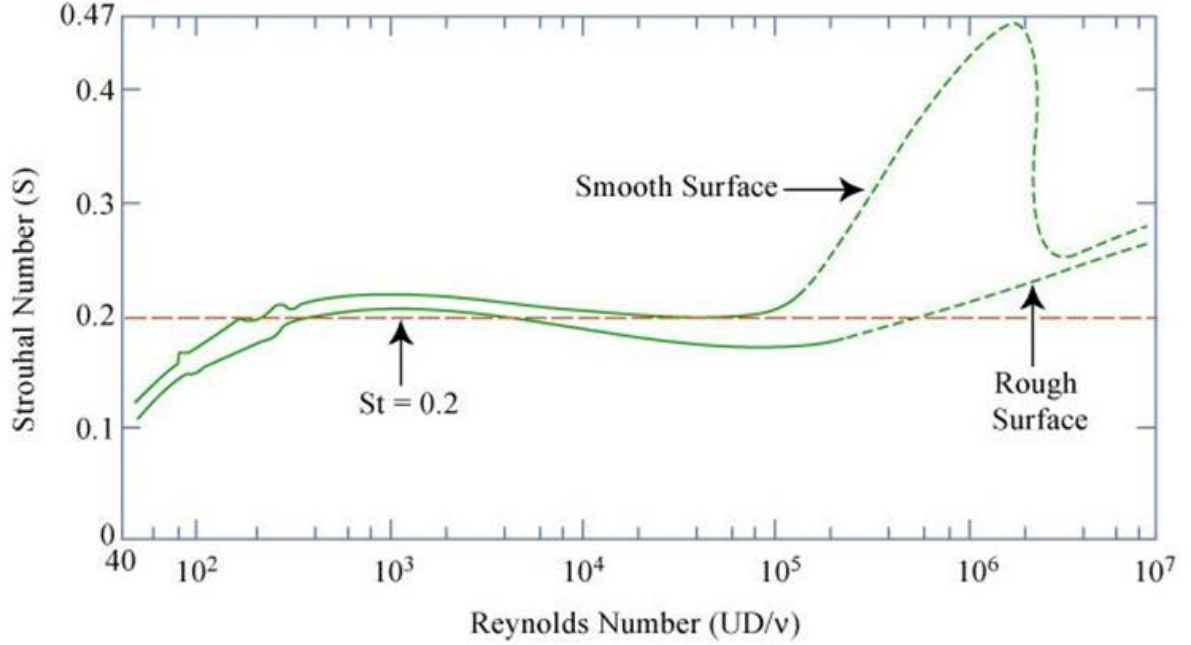


Figure 2.3 Relationship between Strouhal number and Reynolds number for circular cylinders (Lienhard, 1966; Achenbach and Heinecke, 1981)

According with Figure 2.3, due to the short ranged vortex shedding, the value of Strouhal number is stable and close to 0.2 in the subcritical regime. In the critical regime the value of St alters due to a wide ranged vortex shedding. In the supercritical regime where the wake is highly turbulent and aperiodic, a curve behavior is rather similar. At higher Reynolds number where the vortex shedding becomes periodic, the values of St increase to around 0.27.

Reduced velocity

The reduced velocity is defined as the ratio of the path length in flow direction per cycle to the model width.

$$V_r = \frac{\text{path length per cycle}}{\text{width}} = \frac{U}{f_0 D}, \quad (2.3)$$

where f_0 is the natural frequency in still water:

$$f_0 = \frac{1}{2\pi} \sqrt{\frac{k}{m + m_{a0}}}, \quad (2.4)$$

where k is stiffness, m is the mass of the cylinder, m_{a0} is the added mass in still water. If the oscillation frequency is used in still water, V_r will be as follows:

$$V_r = \frac{U}{f_{osc} D} = \frac{1}{\hat{f}}, \quad (2.5)$$

where \hat{f} is non-dimensional frequency (described in the next section), f_{osc} is the oscillation frequency:

$$f_{osc} = \frac{1}{2\pi} \sqrt{\frac{k}{m + m_{a0}}}, \quad (2.6)$$

where m_a is the added mass valid for the certain flow and oscillation condition.

Non-dimensional frequency

The non-dimensional frequency is the parameter defining the condition for a cylinder with forced motions. Also \hat{f} is a key parameter to control the added mass.

$$\hat{f} = \frac{f_{osc} D}{U}. \quad (2.7)$$

Roughness ratio

The roughness ratio characterizes the surface of the cylinder.

$$\text{Roughness ratio} = \frac{k}{D}, \quad (2.8)$$

where k is surface roughness.

Strouhal number is strongly dependent on surface roughness in the critical flow regime (see Figure 2.3).

Mass ratio

The mass ratio for a cylinder is defined as a relation between its mass per unit length m and ρD^2 .

$$\text{mass ratio} = \frac{m}{\rho D^2}. \quad (2.9)$$

The mass ratio is important parameter for the added mass effects on the cylinder. This is illustrated in Figure 2.4, where the non-dimensional response amplitude A/D is presented as function of the reduced velocity.

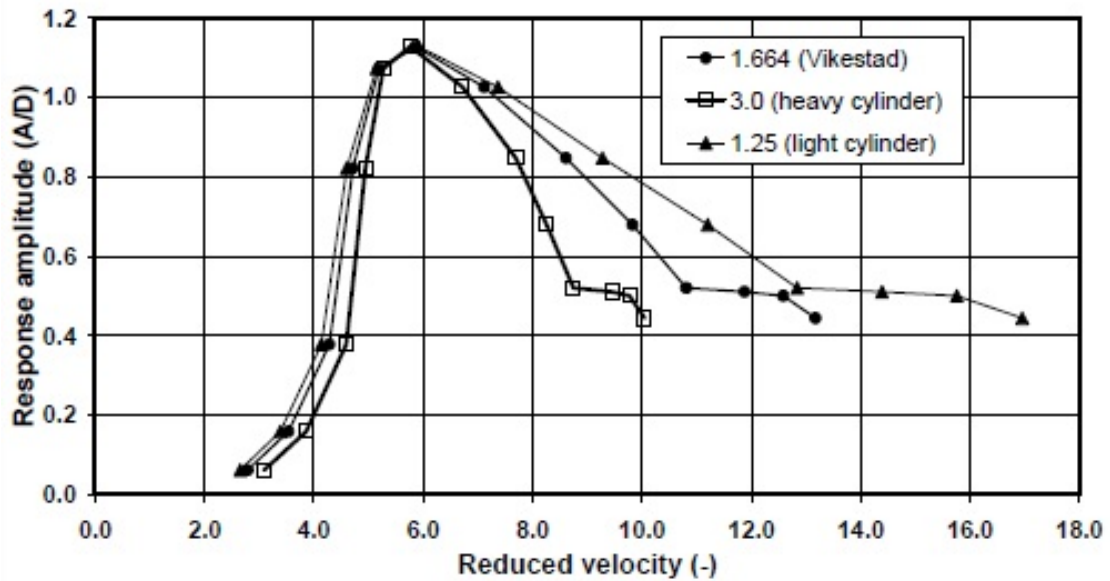


Figure 2.4 Non-dimensional amplitude versus reduced velocity for three cylinders with different weight (Vikestad, 1998)

Non-dimensional displacement amplitude ratio

The response amplitude A/D is the parameter characterizing the displacement amplitude in free vibration experiments and oscillation amplitude in forced oscillation experiments (Gopalkrishnan, 1993).

$$\left(\frac{A}{D} \right)_{IL/CF} \quad (2.10)$$

2.1.3 Lock-in

The typical lock-in situation means that for the constant Strouhal number the vortex shedding frequency becomes close to the natural frequency of the oscillating cylinder. Vortex shedding will start to correlate along cylinder axis and the forces acting on the cylinder will dramatically increase. This can cause resonant conditions and the cylinder will vibrate with large amplitudes. If the flow velocity increases/decreases, the vortex shedding frequency will return back to the linear curve of Strouhal number relation. Thus, lock-in shows that the response frequency is a function of flow velocity (see Figure 2.5).

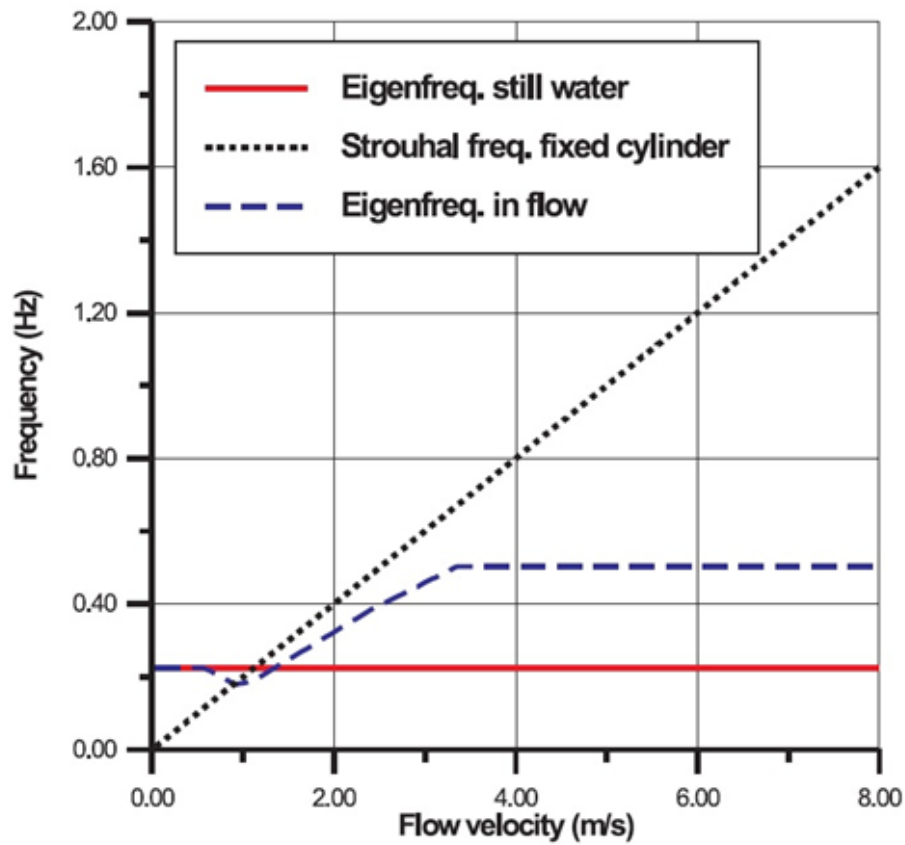


Figure 2.5 Lock-in or synchronization of vortex shedding cross-flow oscillations, added mass is assumed to follow the VIVANA model (Larsen et al., 2002)

Due to the earlier observations, it is found that the oscillation frequency is not equal to the eigenfrequency of a cylinder in the still water due to the added mass variations. As mentioned before, the added mass depends on the flow and the oscillation conditions. In such case, the oscillation frequency will become a compromise between vortex shedding frequency and natural frequency of the cylinder.

2.2 VIV investigation methods

It is known that the strong currents cause VIV of the risers, which lead to detrimental effects such as amplified drag load and fatigue accumulation in metal. The current influences along the riser length causing its oscillations which in turn restricts the offshore operations. The riser data acquisition at the well site can be hampered due to the harsh metocean conditions and high water depth. Thus, a lot of attempts were made by scientists to analyze the riser behavior when subjected to VIV. The investigations of vortex shedding influence on slender marine structures can be made numerically or experimentally.

2.2.1 Numerical investigations

Numerical models are aimed on solving and analyzing the problems, generally connected to fluid flow. Fluid motion is defined by Navier-Stokes equations. It is a set of non-linear partial

differential equations derived from mass, energy and momentum conservation laws. The discretization method is used to solve this set. Solution is made by approximation of these equations at some set of discrete locations in space and time. There are few different methodologies of discretization. The main ones are the Finite Difference Method (FDM), the Finite Element Method (FEM) and the Finite Volume Method (FVM).

The most common way to perform these numerical analyses is the usage of Computational Fluid Dynamics (CFD). CFD is a computerized tool that performs numerical calculations and analysis of fluid mechanics. It serves to investigate the fluid-structure interaction (including VIV) using boundary conditions. However, the CFD calculations are time-consuming, thus the analysis is typically performed by supercomputers or another way of examination is chosen (Huang and Chen, 2007).

2.2.2 Model tests

In the recent years, a number of experiments have been made to give better understanding of VIV phenomenon. Tests have been performed at various conditions in order to compare different behaviors of submerged cylinders. It is known that responses of cylindrical bodies depend on several parameters (Vikestad, 1998). Thus, the main purpose of the empirical investigations is to determine the effect of these parameters. In this section, several fundamental tests such as rigid cylinder free/forced oscillation tests are briefly described. Besides that, the Norwegian Deepwater Programme (NDP) experiment with an elastic cylinder is also presented.

Rigid cylinder free oscillation tests

The free oscillation test is one of the classical ways to illustrate VIV. Figure 2.6 shows the elastically supported cylinder subjected to a constant current. Three different frequencies can be observed in this experiment: the vortex shedding (Strouhal) frequency f_v , the still water eigenfrequency f_0 and the oscillating frequency f_{osc} (Formulae 2.2, 2.4 and 2.6 respectively).

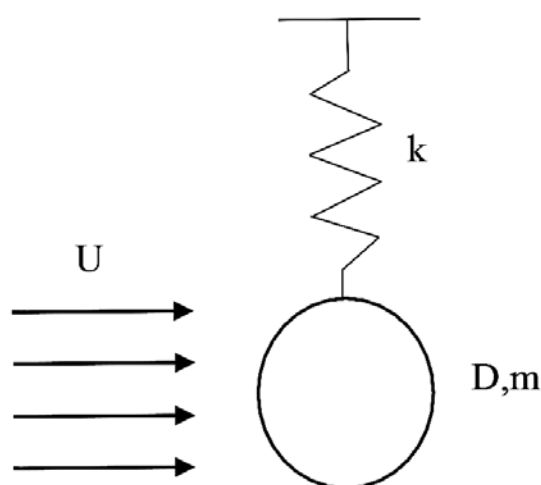


Figure 2.6 Free oscillation test set-up (Larsen, 2011)

As it was mentioned before, the lock-in occurs when the Strouhal frequency becomes close to the eigenfrequency, and the cylinder starts to oscillate with the frequency that differs from f_v and f_0 due to the varying added mass. Vikestad (1998) performed series of experiments which showed that the added mass corresponds to the response frequency, meaning that the lock-in happens at true resonant conditions. Figure 2.7 shows the measured added mass in contrast with the reduced velocity (see Formula 2.5).

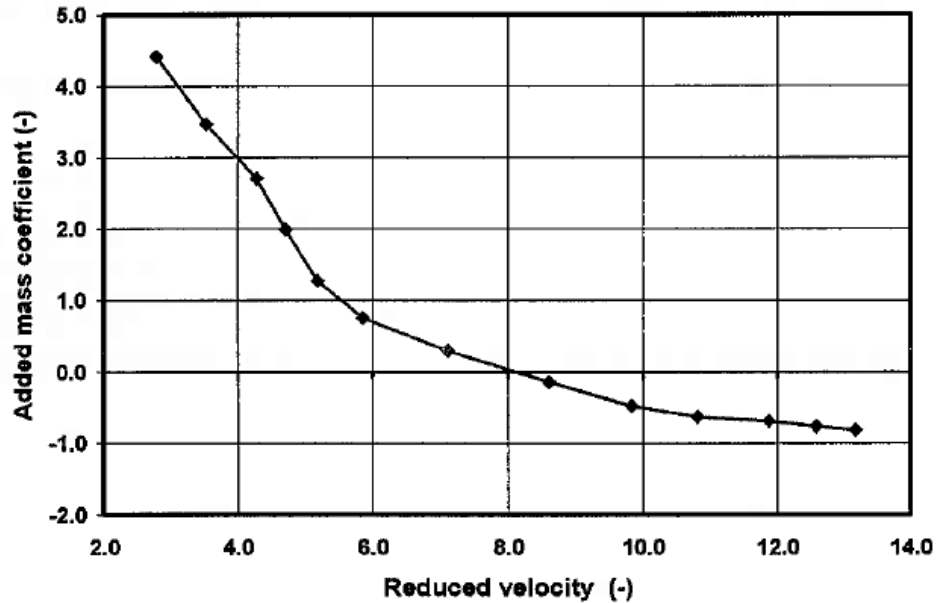


Figure 2.7 Added mass as function of the reduced velocity (Vikestad, 1998)

According to Figure 2.7, the added mass (as a component of the hydrodynamic force) can take the negative values depending on the phase between the total hydrodynamic force and the cylinder motions. Another important observation from Vikestad's experiments is that the added mass variation influences on the dry mass of the cylinder. Lighter cylinders will have a wider range of the response than the heavier ones (see Figure 2.4).

It is known that the dynamic lift force (see Figure 2.8) creates the oscillations and is defined as the component of the hydrodynamic force that is in phase with the cylinder velocity. In case of positive C_e , the excitation force will transfer energy to the oscillating cylinder, and the damping will occur if the $C_e < 0$. Figures 2.8 and 2.9 show the time history for the cylinders with different initial amplitudes subjected to VIV: zero A/D_0 and high A/D_0 respectively. In the first case, positive lift force will increase the response amplitude until the steady state is obtained ($C_e=0$). In the second case, big oscillations will lead to hydrodynamic damping (response will be reduced) until the same balance is obtained. These observations have been proven that the excitation coefficient depends on the response amplitude.

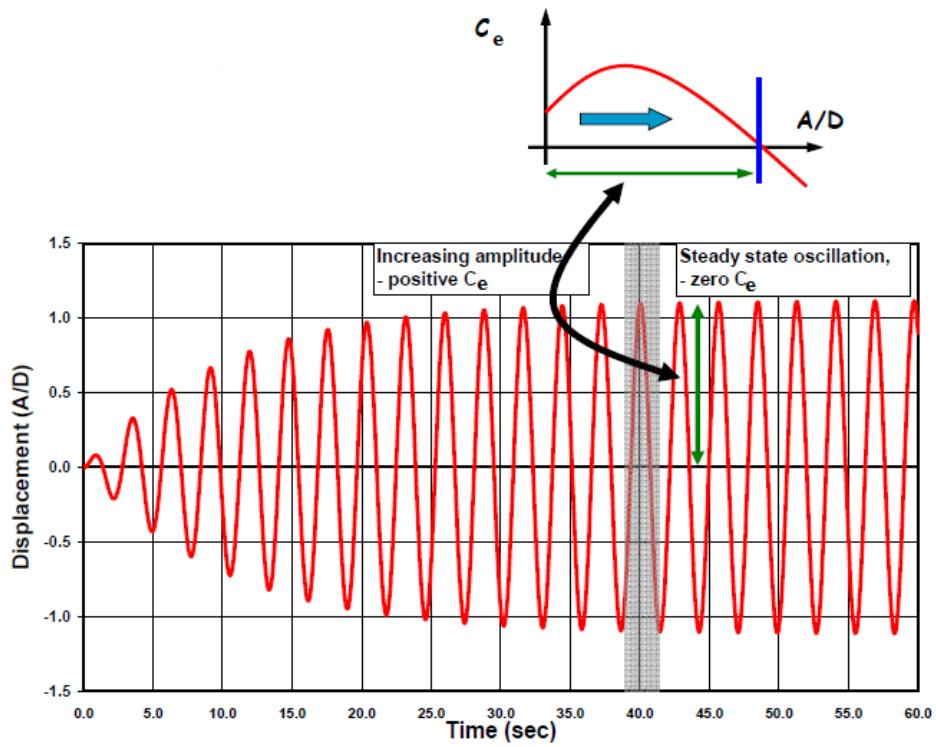


Figure 2.8 Time history for the oscillating cylinder with $A/D=0$ initial condition (Larsen, 2011)

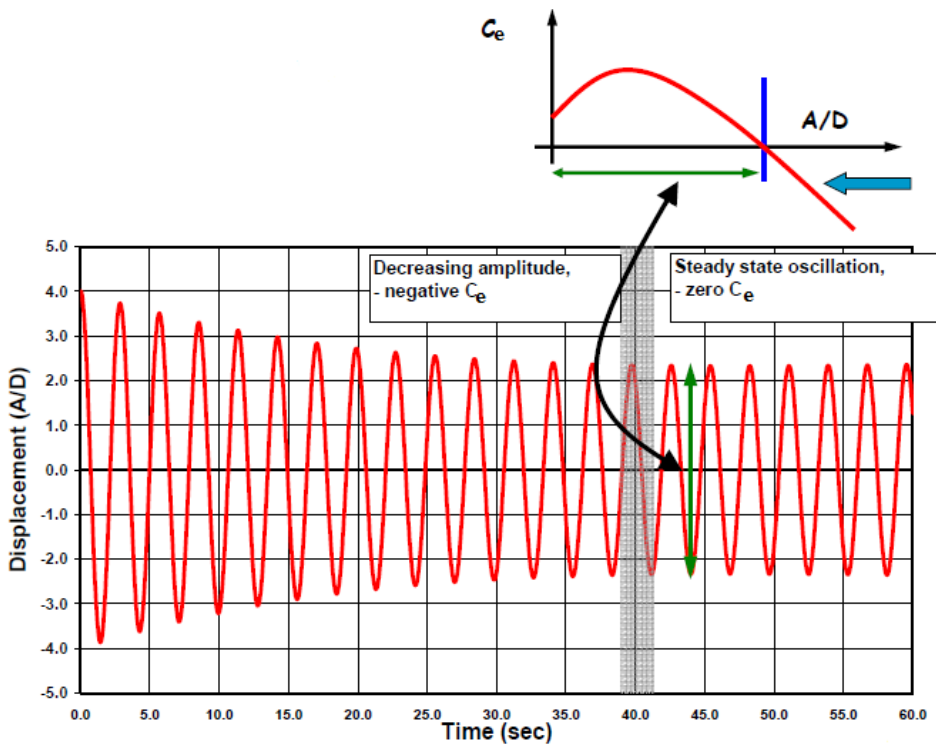


Figure 2.9 Time history for the cylinder with high A/D initial condition (Larsen, 2011)

The purpose of free oscillation tests is to obtain the following parameters:

- IL/CF frequencies;
- IL/CF amplitudes;
- Drag coefficients for an oscillating cylinder.

Since the forces during the free oscillation tests are equal to zero, the dynamic CF and IL force coefficients cannot be obtained. Since the forces in the transient phase (see Figures 2.8 and 2.9) may differ from the forces under stationary oscillation conditions, this approach is uncertain. Thus, there is a need to perform forced oscillation tests (described lower) to achieve a complete set of parameters.

Rigid cylinder forced oscillation tests

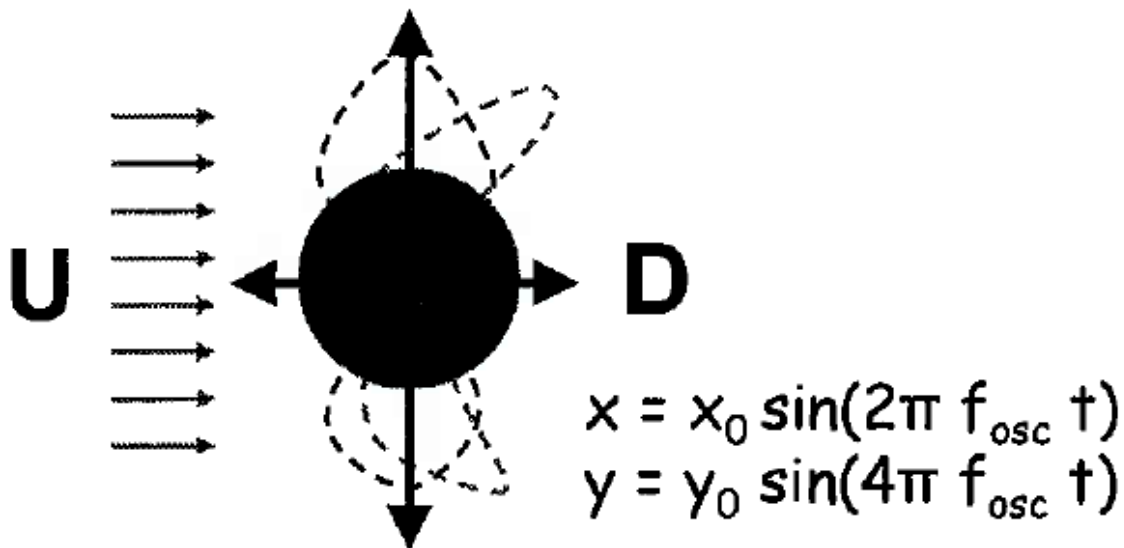


Figure 2.10 Forced oscillation test set-up (Larsen, 2011)

Figure 2.10 shows the experimental set-up for the forced oscillation test. The cylinder is subjected to uniform flow and is given a predefined oscillation motions. These motions can be both IL or CF, or combined IL and CF. In this case, forces acting on the cylinder can be measured as well as the force components that are in phase with the velocity (lift coefficients) and with the acceleration (added mass coefficients). The experimental results are typically represented by the contour plots (see Figures 3.5, 3.6). Obtained curves for the coefficients are the two-parameter functions of non-dimensional frequency and amplitude ratio.

In sum, the forced oscillation tests allow us to obtain all necessary VIV parameters such as the added mass, lift, drag and dynamic force coefficients. These coefficients are the core of many VIV prediction programs used today.

Norwegian Deepwater Programme (NDP) experiment

Norwegian Deepwater Programme (NDP) performed high mode VIV-tests in the MARINTEK Offshore basin in December 2003. A long riser was tested at different towing speeds and flow types (uniform and sheared). Cross-flow and in-line responses were measured for different riser configurations, such as bare riser and the riser with strakes.

The main objectives of the model test were (Braaten and Lie, 2005):

- To improve understanding of high-mode VIV, i.e. the responses of long (high L/D) cylinder (riser imitation) in various current speeds and profiles.
- To determine transfer standard for classification and validation of predictive codes for VIV riser response and fatigue damage inclusively and also for CFD (Computational Fluid Dynamics) codes.
- To estimate the suppression effectiveness of varying strake coverages.

Test arrangement

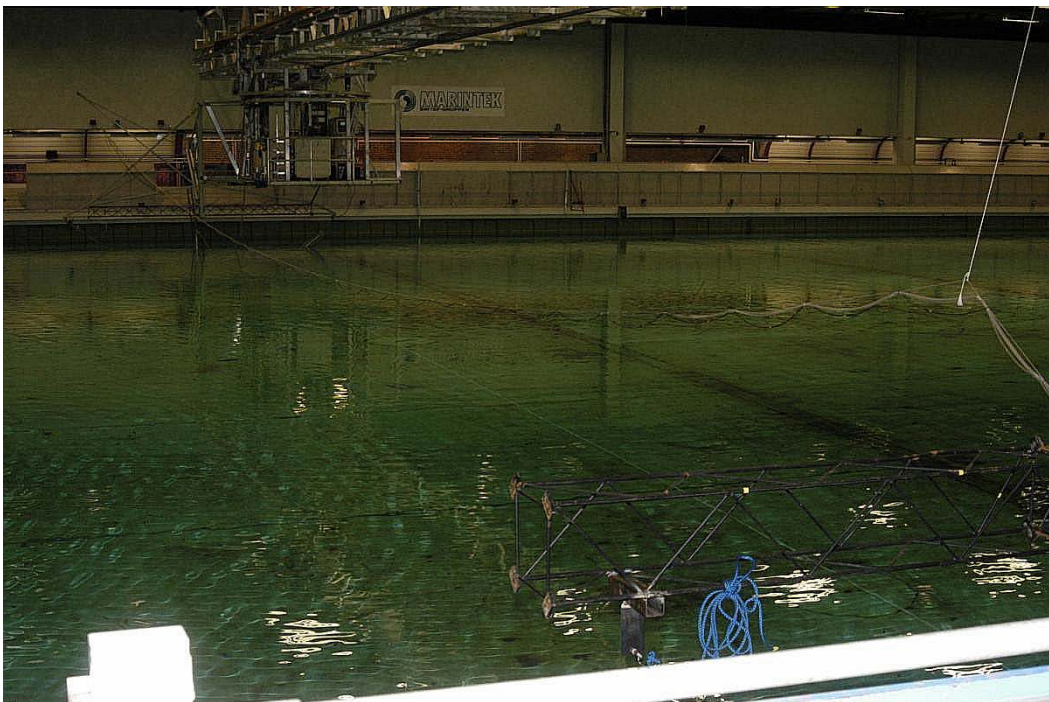


Figure 2.11 Overview of the test setup (Braaten and Lie, 2005)

The tests were carried out in The Ocean Laboratory at MARINTEK. The basin has the following dimensions:

- Width is 50 m;
- Length is 80 m;
- Depth is 10 m.

A 38 m horizontal cylinder was tested for VIV at different towing speeds (from 0.3 m/s to 2.4 m/s) in uniform and shear flow. Cylinder material is reinforced glass fiber pipe with outer diameter 27 mm, 3 mm wall thickness and the mass ratio of around 1.6. Figure 2.11 shows an overview of the test set-up. The main fluid, structural parameters are represented in Table 2.1.

Table 2.1 Main test parameters (Braaten and Lie, 2005)

Total cylinder length, m	38
Outer diameter, mm	27
Wall thickness, mm	3
Bending stiffness, EI, Nm ²	598.8
Axial stiffness, EA, N	5.09*10 ⁵
Shear stiffness, G, GPa	120
Young modulus, E, GPa	36.2
Mass of cylinder (water filled), kg/m	0.933
Mass of cylinder (air filled), kg/m	0.761
Mass of displaced volume, kg/m	0.576
Mass ratio	1.62
Towing speed, U, m/s	0.3 – 2.4
Strouhal number, St	0.2
Axial tension magnitude, N	4000 - 6000
S-N curve constant	11.63
Slope of the S-N curve	3

Riser ends' vibrations are diminished due to the installation of mass-dominated test rig with very small natural frequencies. At the lower end of an inclined pendulum, clump weights were attached to both ends of the cylinder. The upper end was towed by means of transverse crane system (gondola). The principal sketch of the test rig is shown in Figure 2.12.

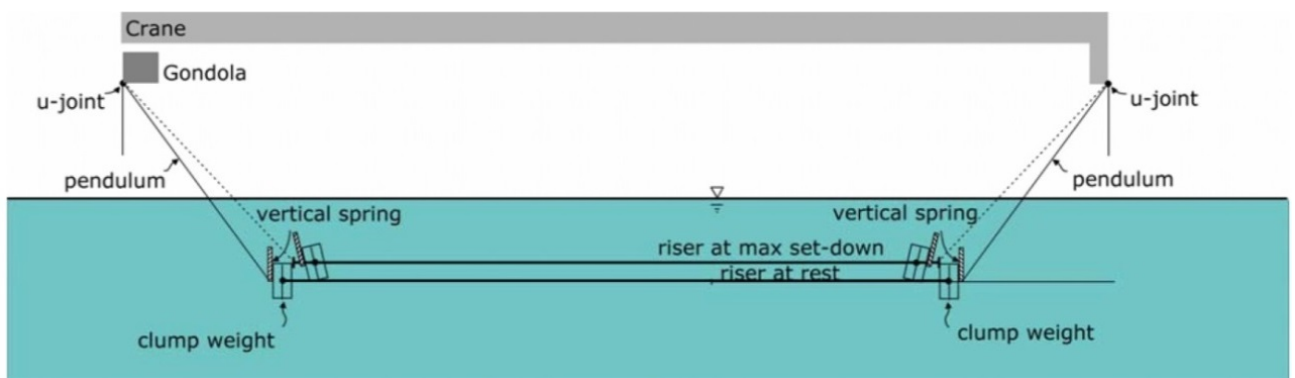


Figure 2.12 Test rig sketch (Braaten and Lie, 2005)

The test rig components are the following:

- Clump weights with vertical springs for control of the riser ends motions. Weights also have a heave compensator which maintains stiffness and natural periods in the cylinder direction (see Figure 2.13).
- An inclined pendulum arm which connects the clump weight to the crane system. The pendulum controls the rotational motions of the clump weights.
- A horizontal framework where the springs in the towing directing are connected to the test rig.

The bending strains were measured at 40 positions along the cylinder (24 are for CF and IL direction, other 16 are only for IL) and 8 locations were made to estimate acceleration signals for both CF and IL direction (see Figure 2.14 a, b). Various tensions were applied to the pipe to control its stiffness.

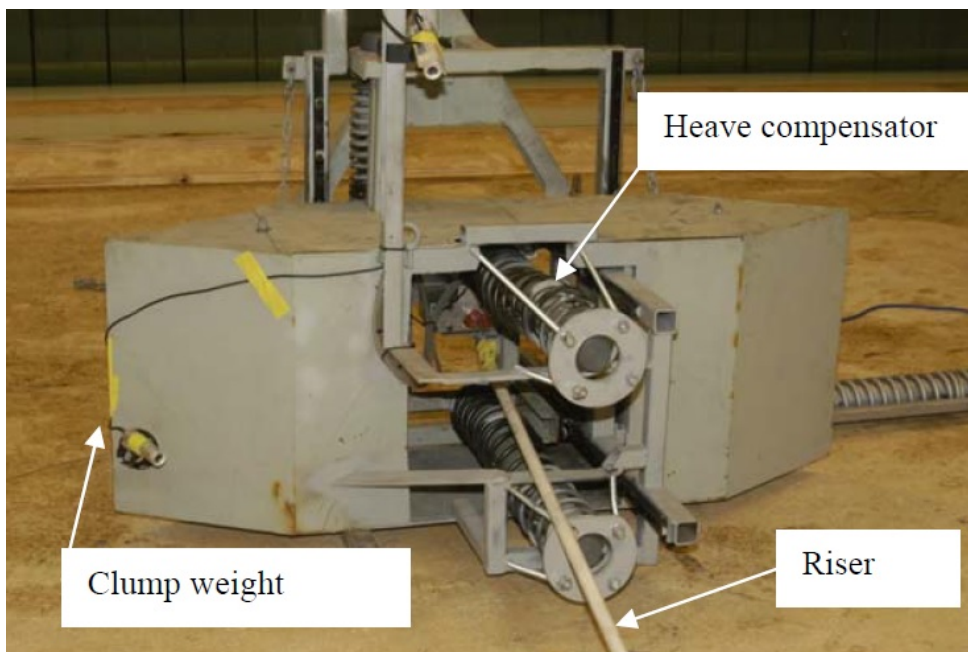
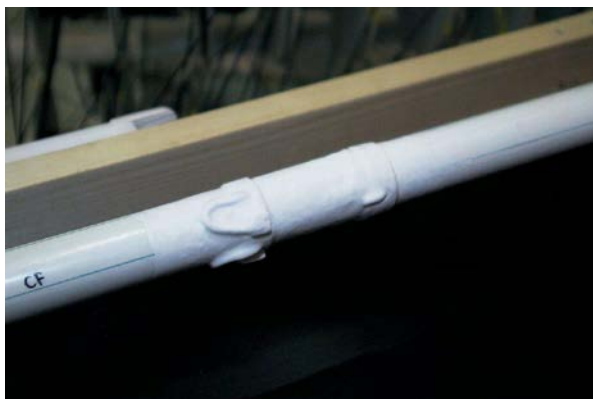


Figure 2.13 Clump weight and heave compensator (Braaten and Lie, 2005)



a



b

Figure 2.14 Riser instrumentation: a) strain gauge and b) accelerometer (Braaten and Lie, 2005)

NDP test results

The total amount of test runs is 341 with towing speeds from 0.3 m/s to 2.4 m/s (step 0.1 m/s). Typical uniform and triangular sheared flows were considered.

The following parameters were obtained during the test (Trim et al., 2005):

- Mean and maximum of displacement standard deviation over the riser.
- Peak frequency of the dominant mode with respect to displacement.
- Dominant modes with respect to displacement and curvature.
- Maximum accumulated fatigue damage.

VIV displacement amplitude

Figure 2.15 shows the CF and IL response amplitudes for uniform and sheared flow. Due to the results, CF displacement dominates (approximately 3 times bigger) the IL displacement for all towing speeds. The sheared CF displacements are shade less than for uniform flow. The similar trends are observed for both graphs versus flow speed.

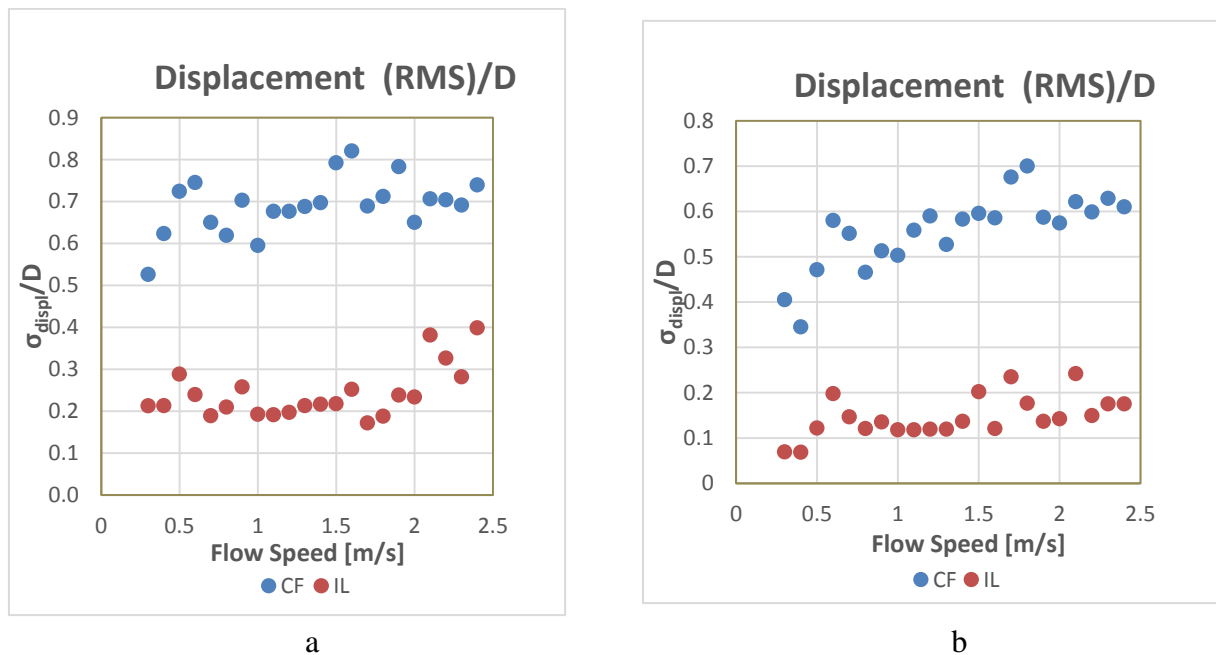


Figure 2.15 Maximum of temporal displacement standard deviation:
a) for uniform flow and b) for sheared flow (Trim et al., 2005)

Response frequency

Both for uniform and sheared flows, the peak frequency of the IL dominant mode tends to grow linearly with increasing towing velocity and dominates (approximately 2 times bigger) the CF dominant mode. The obtained results show that the response frequency of the oscillating cylinder will not be equal to the vortex-shedding frequency.

Modal character

Based on the results, CF and IL dominant mode numbers tend to increase with growing flow velocity for uniform and sheared flow. IL modes are generally twice higher than CF modes.

2.3 SLWR investigations

2.3.1 Buoyancy elements interaction with riser

Use of SLWR system in the offshore industry has proven its advantages over the SCR system and became preferable solution in severe environment. However, when operating at great depths and strong currents, SLWR is exposed to many difficulties linked to VIV.

Since SLWR has the buoyancy section with floating elements of bigger diameter, when subjected to current, both bare and buoyancy parts of a riser will be excited at two different frequencies. Excitation frequency of the bare section is generally bigger than in the buoyancy section since the ratio of buoyancy element length and its diameter is small. The detailed VIV analysis of both parts is, hence, needed to obtain the global response of the riser. Special focus should be devoted to the buoyancy part. There are the following challenges the buoyancy section faces with when submerged into seawater (Jhingran et al., 2012):

- Since the buoyant part of a riser is relatively horizontal (small depth variation along this region), it is subjected to a constant current. The most severe VIV have been observed in constant current (Chakrabarti, 2005). Thus, the VIV analysis for this section should be performed as for horizontal pipe;
- Due to the low tension in the suspended part of a riser (at the sag bend area, see Figure 1.2), relatively high curvature is observed at VIV conditions. This leads to increased fatigue damage in this region.

These observations have been induced scientists to perform more experiments and simulations to achieve the optimal design of the buoyancy elements. Such works were performed by Wu et al., 2016 and Jhingran et al., 2012 and others and can be used for additional reading. Key design elements of a buoyancy section are the following:

- Material of the buoyancy elements;
- Length of the buoyancy section;
- The buoyancy elements configuration;
- The buoyancy elements arrangement;
- Position of the buoyancy elements along the riser;
- The buoyancy element aspect ratio $\frac{L_{buoyancy}}{D_{buoyancy}}$.

Shell experiment

One of the experimental SLWR riser investigations has been performed by Shell Oil Company in the SINTEF Ocean basin in 2011 (Lie et al., 2012). The main purpose of the experiment was to examine the effect of VIV (response frequency, displacement amplitude and RMS curvature) on SLWR with different buoyancy elements arrangement subjected to uniform current. Bare and buoyancy parts outer diameters have been chosen 30 mm and 80 mm respectively. Figure 2.16 illustrates different buoyancy configurations which have been

investigated. The length of one buoyancy element is defined as L_B while the length between two near-by buoyancy elements is represented by L_C . In this experiment, the length of one buoyancy element has been taken as 0.4086 m. As an example, configuration $L_C/L_B=5/2$ means that the bare part between two adjacent buoyancy sections is 5 times the length of single buoyancy element: $5 \cdot 0.4086 = 2.043$ m, while the length of the buoyancy section is $2 \cdot 0.4086 = 0.8172$ m.

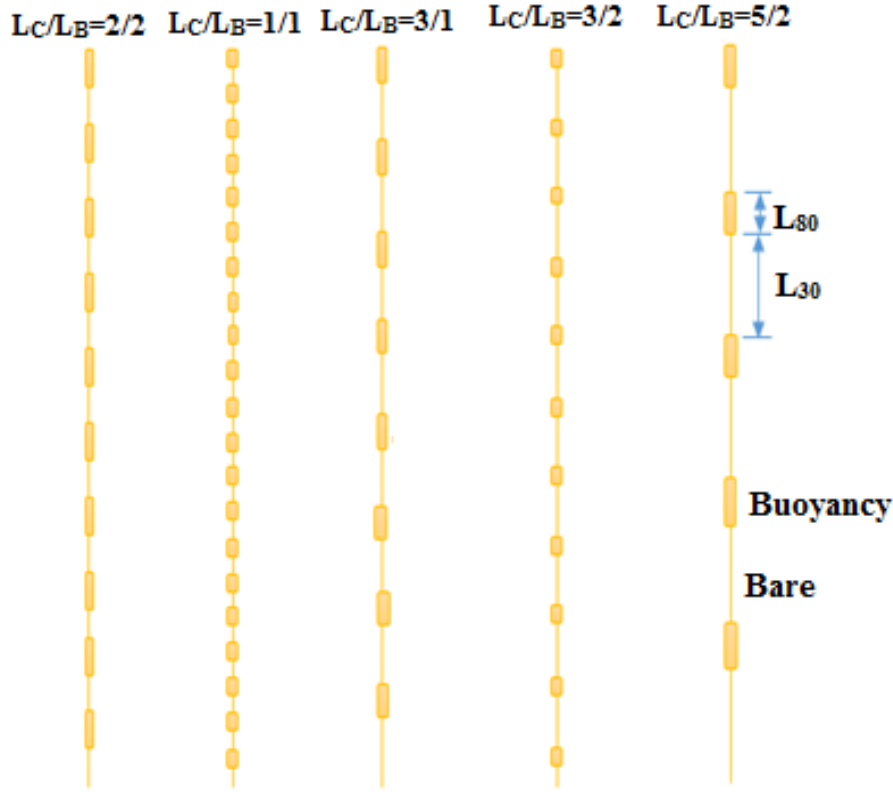


Figure 2.16 Staggered buoyancy configurations over the riser (Rao et al., 2015)

Experiment Results

The following key results have been obtained during the experiment (Wu et al., 2016; Jhingran et al., 2012):

- Due to the different diameters of bare and buoyancy parts, two excitation frequencies appear simultaneously. Bare riser responses at higher frequency than buoyancy parts (see Figure 2.17); the Strouhal number is higher for bare part;
- Due to the hydrodynamic damping, the damping in the governing equation becomes inconstant, and the structural system becomes nonlinear because of the interinfluence between damping and amplitude;
- It has been observed, that the non-linear interaction frequency is governed by the following equation:

$$f_{\text{inter}} = f_{\text{bare}} + 2 \cdot f_{\text{buoyancy}}, \quad (2.11)$$

where f_{bare} , $f_{buoyancy}$ are the frequencies associated with bare and buoyancy sections respectively;

- The non-dimensional frequency is generally higher for bare part of the riser due to the small buoyancy element aspect ratio $\frac{L_{buoyancy}}{D_{buoyancy}} \approx 5$.

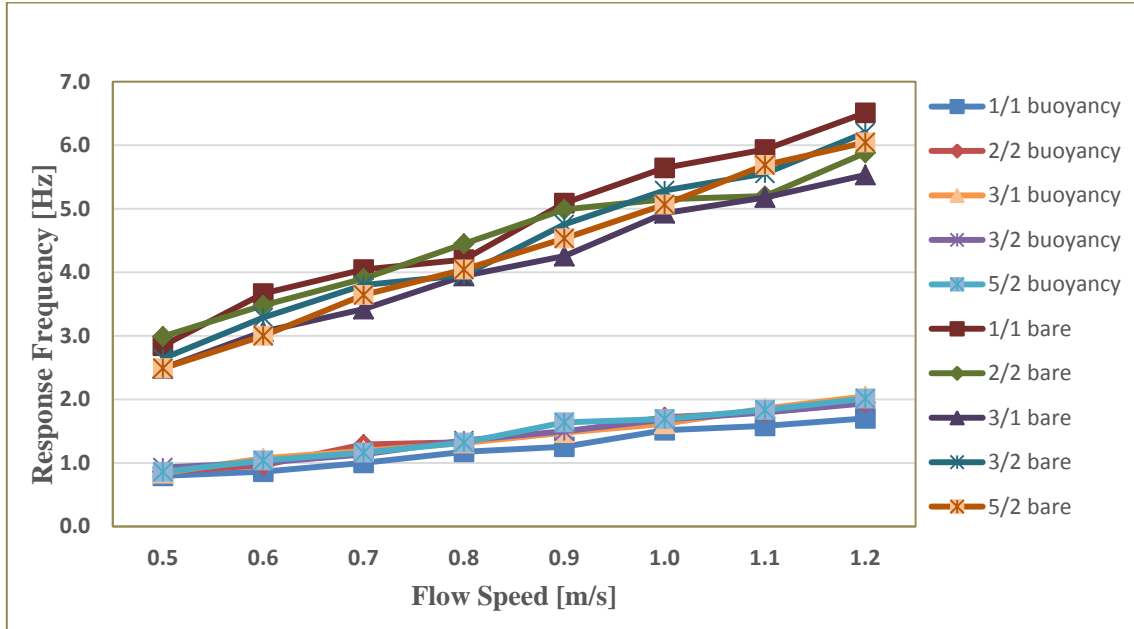


Figure 2.17 Response frequencies associated with bare part and buoyancy part respectively for five configurations (Rao et al., 2015)

2.3.2 Riser-seafloor interaction

When the riser contacts the seafloor at TDP, interaction forces appear between soil and riser. This interaction is usually represented by the set of springs, perpendicular to the riser. These springs characterize the horizontal and axial seafloor restraints against the motions of riser at touch down area.

The riser-soil interaction depends on the riser motions and the properties of soil. There are several geotechnical factors which should be taken into consideration while making an analysis:

- Non-linear stress-strain behavior of soil;
- Remolding;
- Backfilling;
- Hysteresis;
- Consolidation;
- Strain rate;
- Gapping and trenching.

At deep water depths, the soils are typically soft (e.g. soft clays or sands). The horizontal and vertical riser motions at the contact area may lead to the trenches of few riser diameters width. Thus, it is important to collect all geotechnical data from the site for the successful interaction modelling. The most important soil parameters are the following:

- Undrained shear strength (for clay soils);
- Plasticity;
- Particle size;
- Permeability;
- Relative density (for sand soils);
- Soil chemistry (for external corrosion investigations).

These characteristics are important for the consideration of soil suction and the dynamic response, including viscous damping effects.

Pipe-soil interaction models

As has been mentioned above, the peak dynamic stresses in riser due to vortex shedding have been observed at the touch down zone. Hence, the riser fatigue life strongly depends on the seabed properties. Figure 2.18 illustrates few proposed models of pipe-soil interaction. These models allow us to calculate stresses appearing in riser at touch down area and estimate its fatigue life.

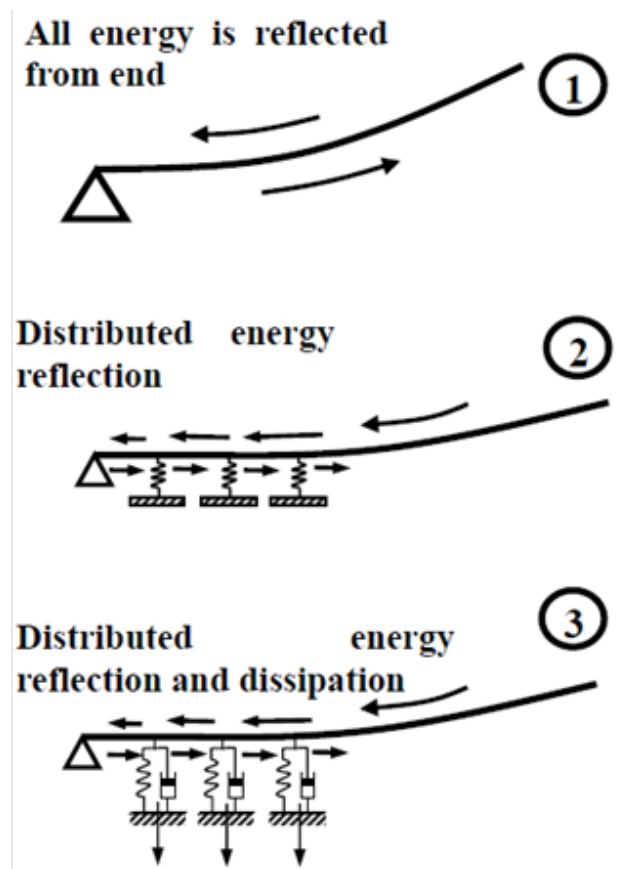


Figure 2.18 Illustration of models for riser/seafloor interaction (Larsen and Passano, 2006)

The truncated model

This is one of the simplest models for the riser VIV analysis at touch down area. The riser end is connected to a rigid moment free support which is located at TDP. The riser part which rests on the seabed is not considered in this model, and the support serves as boundary condition. This support will reflect all energy delivered by the riser.

The elastic spring model

More accurate representation of bending stresses at the touch down area can be achieved by the elastic spring model. Each spring will reflect the part of the riser energy which will give less stress peak in comparison with the truncated model. However, the elastic spring method considers longer bottom segment of the riser, and another stress peak may be expected, depending on the properties of soil.

The spring and damper model

This model takes into consideration the viscoelastic damping of soil and thus is admitted as the most correct model. Not all the energy will be reflected in this case but some part of it will be damped. Consequently, the stress peak in this model will be lower compared to the elastic model.

2.4 Combined IL and CF response

It is known that the long marine riser subjected to flow will oscillate due to the alternating vortex shedding. This in turn will induce time varying forces, acting in CF direction (lift force) and IL direction (drag force). The lift force will oscillate with the Strouhal frequency, but the frequency of the drag force will be twice higher.

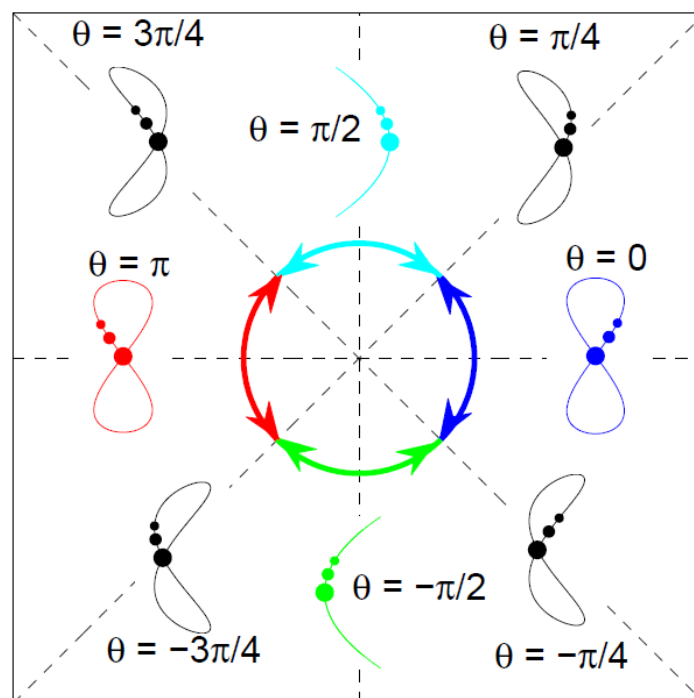


Figure 2.19 Displacement orbits associated with different values of θ (Shi et al., 2010)

The phase angle between CF and IL responses will govern the shape of the displacement orbit. Figure 2.19 illustrates the displacement orbits for different phase angles $\theta(t)$. The horizontal and vertical axes represent IL and CF displacements, respectively. Depending on the phase angle, the trajectory can vary from the figure-eight ($\theta=0$) to the C-shape ($\theta=\pi/2$). Three dots show the direction of the cylinder's motion (from bigger to smaller).

Currently, pure CF VIV phenomenon is well understood (especially at low and moderate modes) due to the numerous analyses and experiments (e.g. Sarpkaya, 1978; Vandivier and Jong, 1987; Blevins, 1990; Gopalkrishnan, 1993). However, understanding of the responses at higher modes is still challenging and requires more parameters to be involved in the model tests. It was observed, that the high mode VIV responses may significantly contribute to fatigue damage of the cylindrical body (Trim et al., 2005).

Pure harmonic IL motions have been studied by Aronsen (2007). He performed a set of tests similar to Gopalkrishnan's experiments. The purpose of the experiment was to obtain the IL excitation coefficients database to predict pure IL responses of pipeline free spans subjected to VIV. These tests showed that the IL responses may appear at lower flow speeds than the CF ones. The reason is that the IL motions will take place at twice higher frequency than the CF oscillations. However, in reality, the slender beam cannot oscillate in pure IL or CF direction. Both components will always appear.

Initially, scientists assumed IL motions to be insignificant due to the smaller response amplitude. However, Baarholm et al. (2006) have asserted that the IL oscillations are equally important as the CF ones in terms of the riser fatigue life. Based on the Hanøytangen experiments, they estimated the ratio between CF and IL amplitudes (A_{IL}/A_{CF}) and found that this ratio strongly depends on the mode order.

$A_{IL}/A_{CF} = 0.5$ for lower modes, but for higher modes this value is equal to 0.3. Consequently, the following relative fatigue damage results have been obtained:

- Low current speed, tensioned string: $\frac{\text{Fatigue}_{IL}}{\text{Fatigue}_{CF}} = 16$;
- High current speed, untensioned beam: $\frac{\text{Fatigue}_{IL}}{\text{Fatigue}_{CF}} = 0.43$.

These results have shown that the IL vibrations will tend to higher bending stresses at tension-controlled modes, while the CF fatigue will dominate at bending-stiffness-controlled modes. Since the mode number and response amplitude are almost independent, stresses caused by IL responses will be higher for lower mode orders.

The fluid-structure interaction changes significantly when the pipe is oscillating in both CF and IL directions (Jauvtis and Williamson, 2004). The case of combined IL and CF motions has attracted many scientists to perform various investigations (e.g. Aronsen, 2007; Dahl, 2008; Soni, 2008). It has been observed that the IL responses are influenced by the CF motions. Compared to the pure IL case, IL amplitudes are larger in combination with CF oscillations. The hydrodynamic coefficients in this case will be larger than those obtained

from Aronsen's pure IL motion tests. Higher order displacement components are observed in IL direction. This will cause larger hydrodynamic forces acting in both CF and IL directions (Yin, 2013). Hence, there is a need to validate the hydrodynamic coefficients database for combined CF and IL response.

Chapter 3

Computer-based VIV prediction program VIVANA

3.1 Introduction

VIVANA is semi-empirical program developed by the SINTEF Ocean Company (formerly MARINTEK) and the Norwegian University of Science and Technology (NTNU). The main purpose of this program is to perform frequency domain VIV analysis of responses of slender marine structures (risers, mooring lines etc.) under the influence of currents. Both cross-flow and in-line responses can be investigated. The standard VIVANA algorithm includes the following steps:

- Static analysis;
- Eigenvalue analysis;
- Identification of possible excitation frequencies;
- Dedication of excitation zones;
- Calculation of CF responses;
- Calculation of IL responses;
- Calculation of fatigue damage.

Fluid-structure interaction in this program is provided by the following hydrodynamic coefficients:

- Added mass coefficients;
- Excitation coefficients;
- Damping coefficients.

These coefficients were obtained experimentally from the rigid and flexible cylinder tests (described in Chapter 2). On the other hand, the program is based on numerical approach for examination of structural dynamics of the slender marine bodies. Thus, VIVANA is called as semi-empirical program.

3.2 Hydrodynamic force coefficients

3.2.1 Added mass coefficients

The added mass coefficients are found from the experiments with the rigid cylinder in free motions (Vikestad, 1998) and under forced motions (Gopalkrishnan, 1993). These experiments are described below. The added mass coefficients in VIVANA are based on the results of Gopalkrishnan's test. The experimental results showed that the added mass depends on the oscillation frequency and the response amplitude. However, only frequency-dependent added mass is taken into account in VIVANA (it is assumed that the added mass is independent from the response amplitude). Typically, the results are represented by the contour plots which show the combinations of the amplitudes and frequencies for the same value of added mass coefficient. Figure 3.1 shows the added mass contour plot for CF vibrations. The amplitude ratio $A/D=0.5$ (red line) is chosen in VIVANA to simplify the added mass as a function of the non-dimensional frequency. The VIVANA model for the added mass is shown in Figure 3.2.

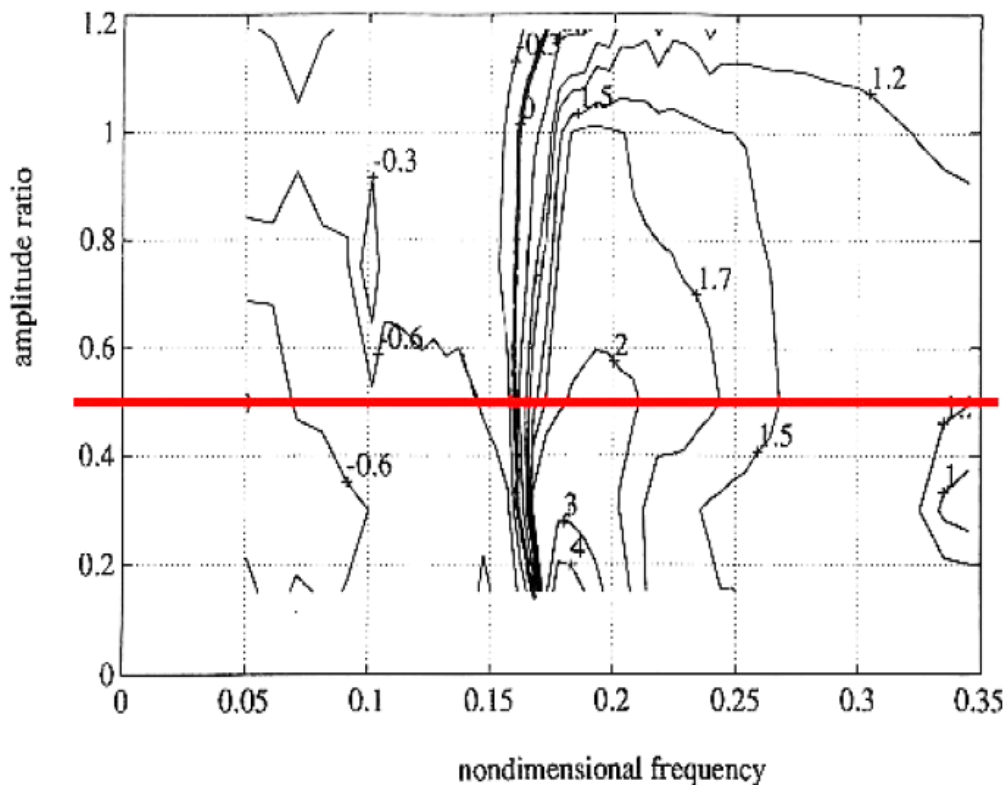


Figure 3.1 Contour plot of the CF added mass coefficients based on forced motions (Gopalkrishnan, 1993)

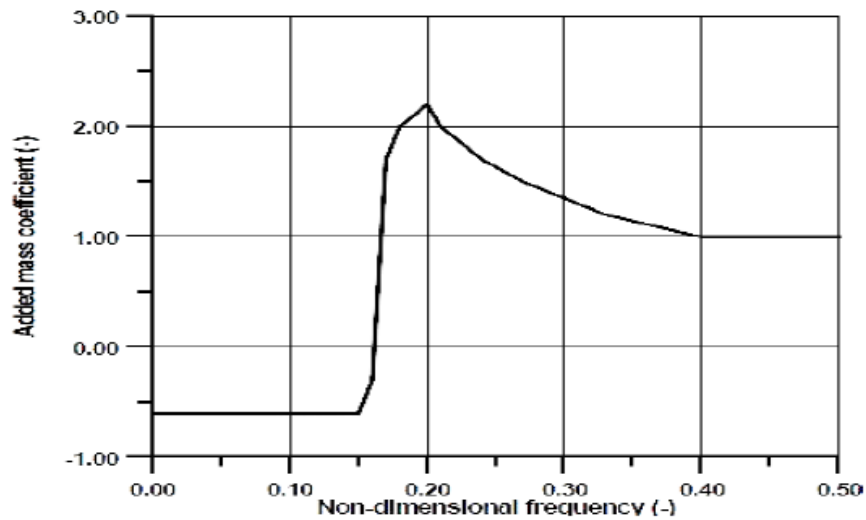


Figure 3.2 VIVANA model for added mass as a function frequency for CF response (Passano et al., 2014)

The added mass values for IL harmonic oscillations were experimentally obtained by Aronsen (2007). Figure 3.3 shows the results of the experiment represented by the contour lines of the added mass coefficients. As it was mentioned before, the added mass is approximated to be dependent only from the non-dimensional frequency. The amplitude ratio $A/D=0.075$ (red line) has been taken in VIVANA to simplify the added mass model. Figure 3.4 represents the simplified added mass as function of the non-dimensional frequency.

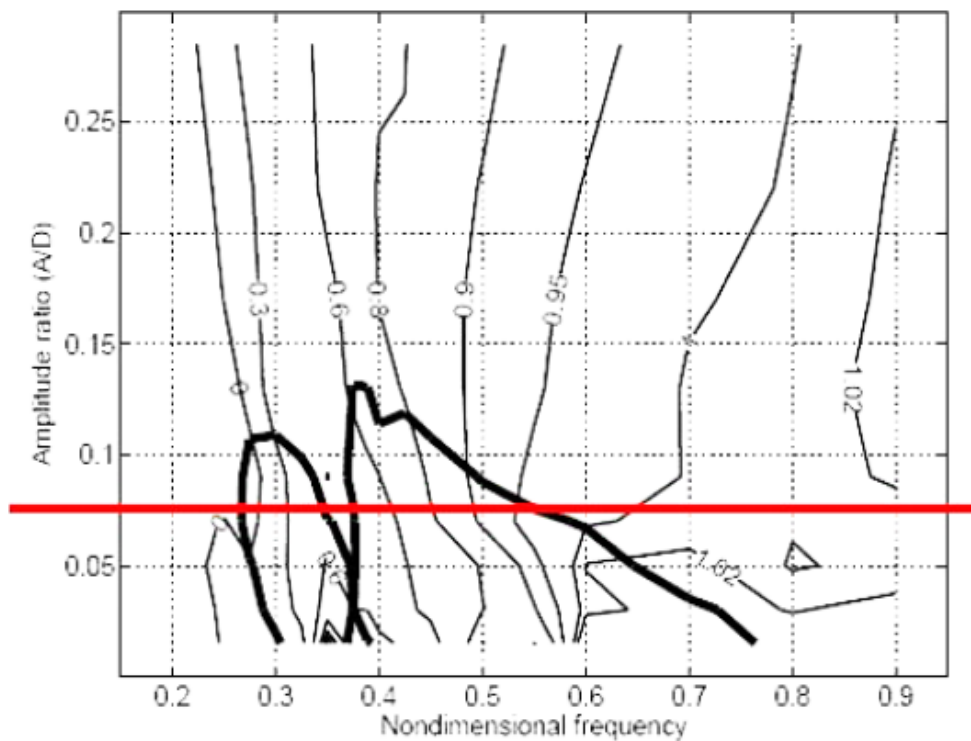


Figure 3.3 Contour plot of the IL added mass coefficients (Aronsens, 2007)

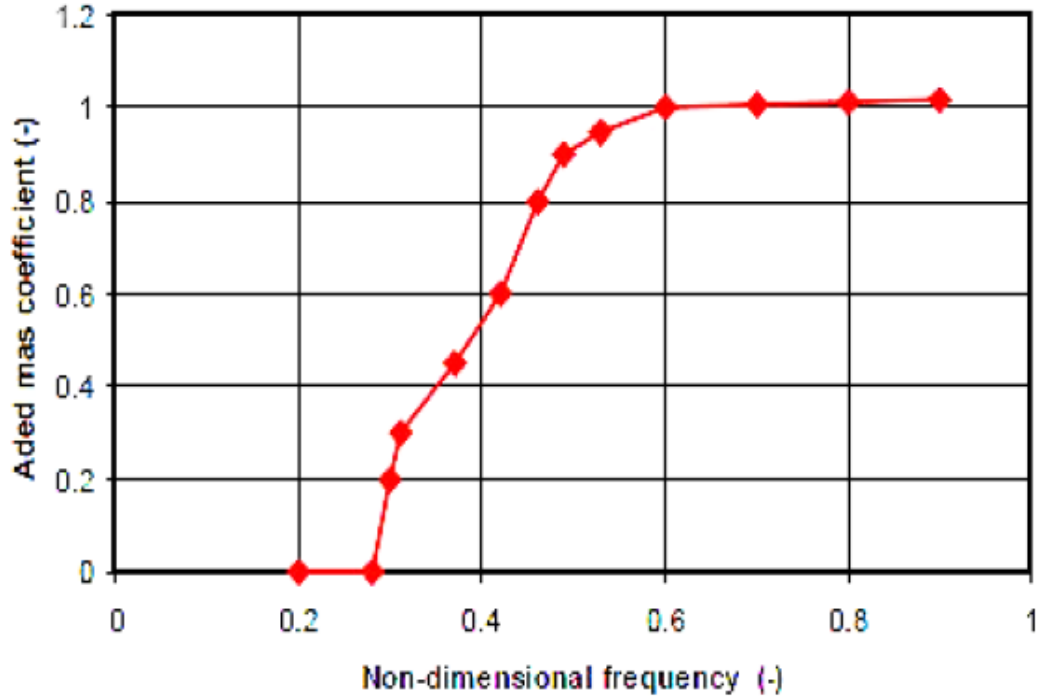


Figure 3.4 VIVANA model for added mass as a function of frequency for IL response (Passano et al., 2014)

3.2.2 Excitation and damping coefficients

The excitation coefficients, as well as the added mass coefficients, are obtained from Gopalkrishnan's forced oscillation tests. The force acting on the cylinder can be separated into two components: one is in phase with the acceleration (added mass coefficient); the other is in phase with the velocity (excitation coefficient). The excitation force (for IL and CF directions) per unit length of an element can be expressed as:

$$F_{e,IL/CF} = \frac{1}{2} \rho C_{e,IL/CF} D_H U_N^2, \quad (3.1)$$

where U is the flow velocity, D is the external diameter of the cylinder, C_e is the excitation coefficient, ρ is the water density.

Figures 3.5 and 3.6 show the contour plot curves for CF and IL excitation coefficients respectively. The red lines represent the excitation regions i.e. the intervals of the non-dimensional frequency where slender marine structures can be excited. For pure CF case, this interval is $0.125 < \hat{f} < 0.3$. For the pure IL case, $0.2 < \hat{f} < 0.9$.

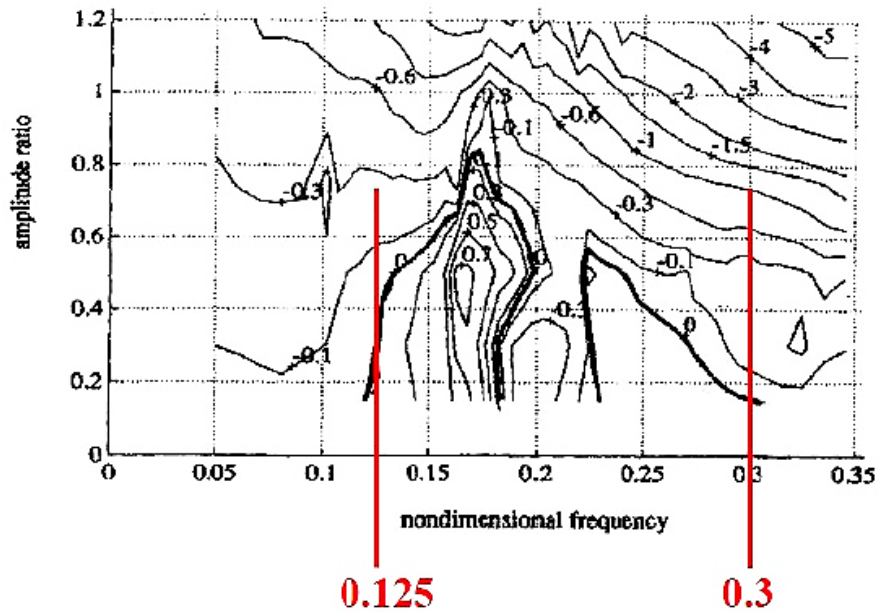


Figure 3.5 Contour plot curves for the CF excitation coefficient (Gopalkrishnan, 1993)

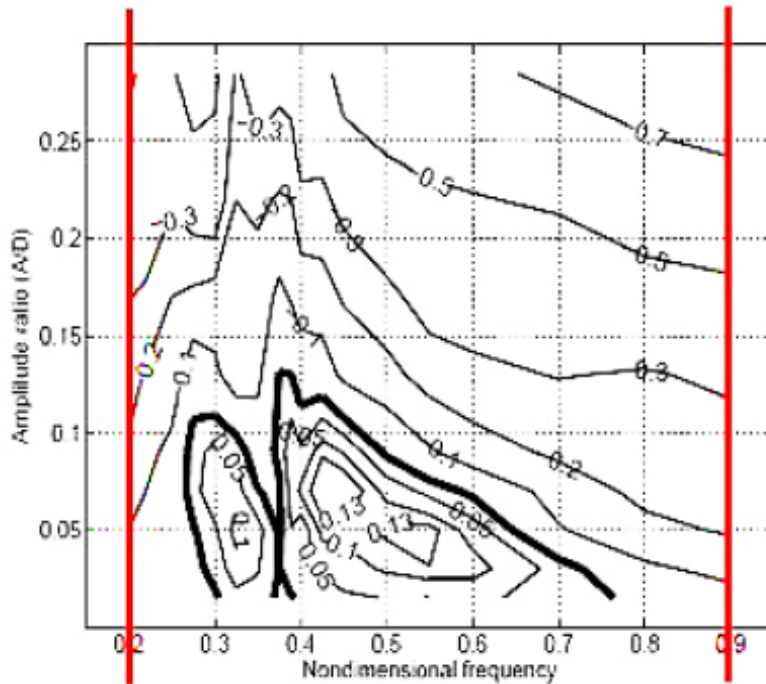


Figure 3.6 Contour plot curves for the IL excitation coefficient (Gopalkrishnan, 1993)

As shown in Figures 3.7 and 3.8, the excitation force coefficients are represented as two-parameter function of amplitude ratio and non-dimensional frequency. VIVANA's built-in model simplifies these counter plots by applying a set of parameters which represents the excitation coefficient as a function of the amplitude. In this model, the maximum value of C_e is at the point B, meaning that the curves AB and BC can be found as two second order polynomial when the points A, B and C are defined. The parameters for IL/CF excitation force coefficients are represented here as functions of the frequency, as shown in Figure 3.9 (CF case only). The IL excitation force coefficient curve is slightly different from CF case since it has been assumed that the excitation coefficient is equal to zero for zero amplitude (see Figure 3.8).

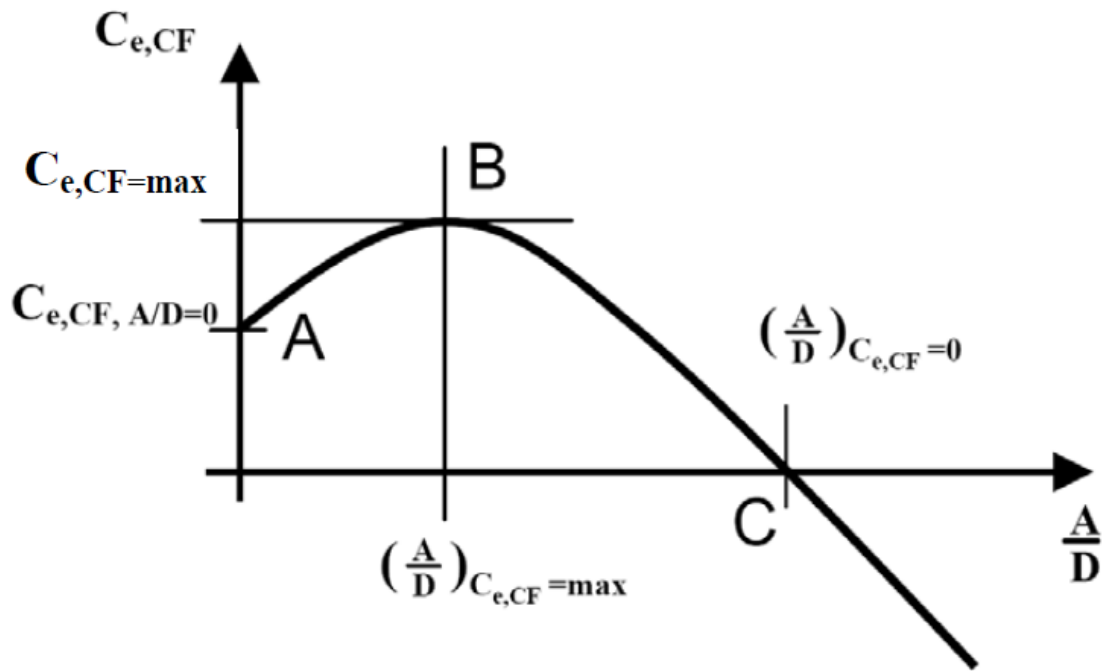


Figure 3.7 The CF excitation force coefficient curve defined from three points (Passano et al., 2014)

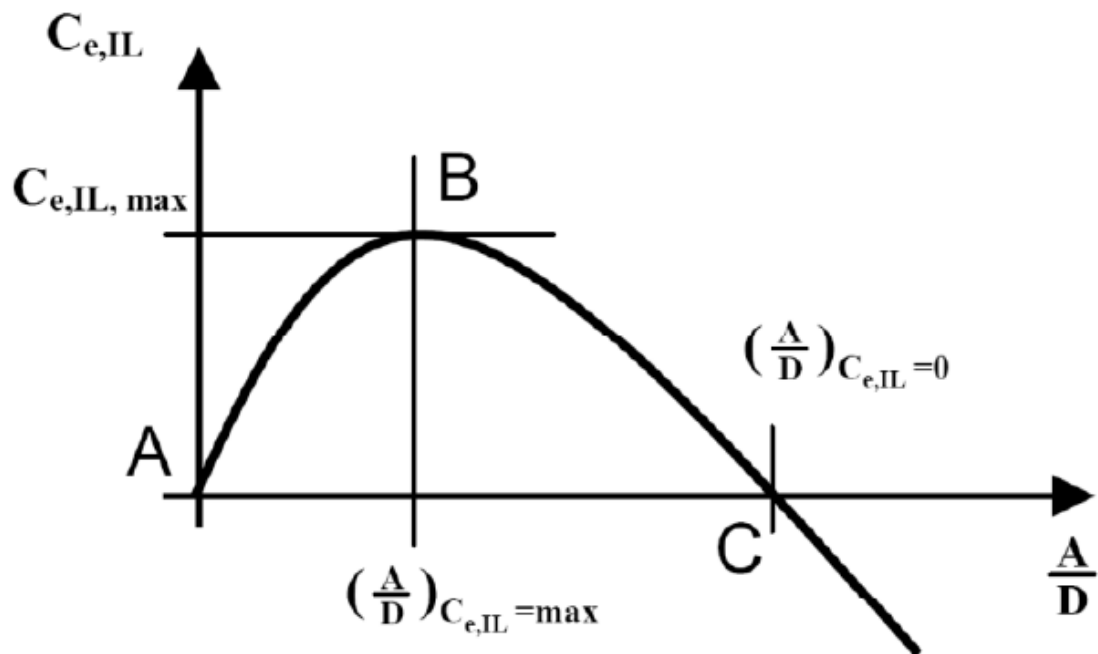


Figure 3.8 The in-line excitation force coefficient curve defined from 3 points, pure IL response (Passano et al., 2014)

It is known that VIV is a self-limiting process even if no mechanical damping occurs (Passano et al., 2014). As shown in Figures 3.7 and 3.8, the lift coefficient (C_e) becomes negative after the amplitude reaches the certain value. In this case, the hydrodynamic damping will occur, and the excitation coefficients will turn into the damping coefficients. Zero lift coefficient ($C_e=0$) means that no energy is transported between the cylinder and the fluid and the oscillations become stationary (lock-in conditions).

Parameters for CF excitation force coefficients

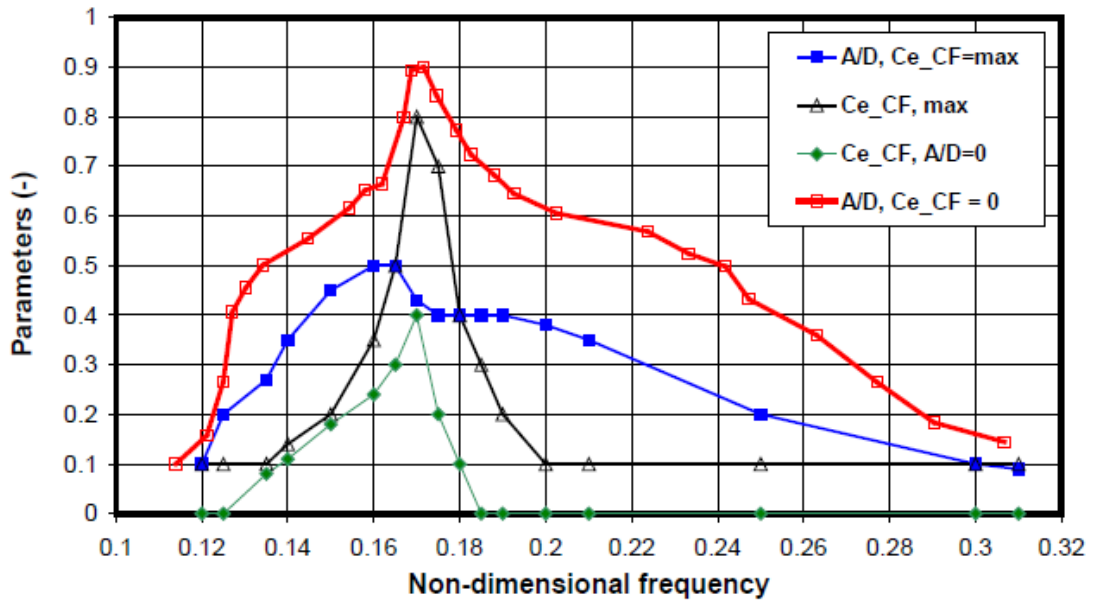


Figure 3.9 Parameters to define specific excitation coefficient curves for CF response analysis (Passano et al., 2014)

3.3 Frequency response method

VIVANA is based on the numerical FEM for solving the equation of motion of a structure subjected to VIV. As mentioned earlier, frequency response method is used in VIVANA to compute the dynamic response at dominant frequency. The program is based on assumption that VIV occur at the discrete frequencies, which in turn are represented by natural frequencies (eigenfrequencies). Thus, FEM approach will give the dynamic equilibrium equation as:

$$M\ddot{r} + C\dot{r} + Kr = R, \tag{3.2}$$

where M, C and K are the mass, damping and stiffness matrixes respectively; \ddot{r} , \dot{r} and r are acceleration, velocity and displacement respectively.

The external load R will in this case be harmonic. However, the loads at any degrees of freedom may not be in phase. The load pattern can be described by a complex load vector X with harmonic time variation.

$$R = Xe^{i\omega t}, \tag{3.3}$$

where ω is the load frequency.

The response vector r is also represented by complex vector x with harmonic time variation. Hence we have:

$$r = xe^{i\omega t} \quad (3.4)$$

By introducing the hydrodynamic mass M_H and damping matrices C_H , the dynamic equilibrium can be written as:

$$-\omega^2(M_S + M_H)x + i\omega(C_S + C_H)x + Kx = X, \quad (3.5)$$

where C_S is the structural damping, also known as the Rayleigh damping. M_S is the structural mass.

The lift coefficient depends on the response amplitude, and the dynamic equation is hence solved by iterations with fixed response frequency. The excitation force must be cophasal with the local response velocity. If the oscillation amplitude is big, damping will occur.

The response vector x is complex, and a harmonic response at all nodes hence can be described (including responses at different phases). It means that the response will appear from both standing and travelling wave contributions. Mathematically, this response vector is equivalent to a complex mode obtained from the damped eigenvalue problem.

The purpose of the iteration is to identify the response pattern and amplitude in order to achieve consistency between the level of response, excitation coefficients and the local flow conditions, i.e. to obtain the response vector governing that the amplitudes and phases are correct at all positions.

3.4 Time sharing and space sharing

When the long marine cylindrical body is subjected to a current with varying profile, there are several response frequencies appear in the cylinder. Each frequency is excited within its zone and it is called dominating frequency for the particular excitation zone. However, these zones may overlap and the response may be governed by more than one frequency. But due to the experience, the vortex shedding process always acts at one dominating frequency no matter how many frequencies compete between each other (Larsen et al., 1997).

These competing frequencies may appear concurrently (simultaneously acting frequencies) or consecutively (acting during certain amount of time). Thus, there are two approaches (assumptions) of the excitation zone determination in VIVANA: time sharing and space sharing (described in the next sections).

3.4.1 Space sharing

The total response will be governed by candidate eigenfrequencies which act simultaneously along the cylinder. To identify which candidate frequency will dominate, an excitation parameter E_i has been defined (Passano et al., 2014):

$$E_i = \int_{L_{e,i}} U_N^3(s) \cdot D_H^2(s) \cdot \left(\frac{A}{D}\right)_{c_e=0} ds \quad , \quad (3.6)$$

where U_N is the flow speed normal to the structure, D_H is the hydrodynamic diameter, s is a coordinate along the riser, $\left(\frac{A}{D}\right)_{c_e=0}$ is the non-dimensional amplitude in the moment when the lifting coefficient turns its value from positive to negative, $L_{e,i}$ is the candidate frequency.

This parameter is necessary for the case with uniform flow, where each acting frequency will have similar U_N and D_H . All candidates will be prioritized by the magnitude of an excitation parameter.

Primary response frequency i.e. frequency with largest excitation parameter will take its whole zone of acting. In case of a highly sheared current, this dominating frequency may not cover the total length of the cylindrical body, and the other acting frequencies will take place in the other parts of the structure reduced by the main response frequency (see Figure 3.10). None of these excitation zones overlaps each other (Passano et al., 2014).

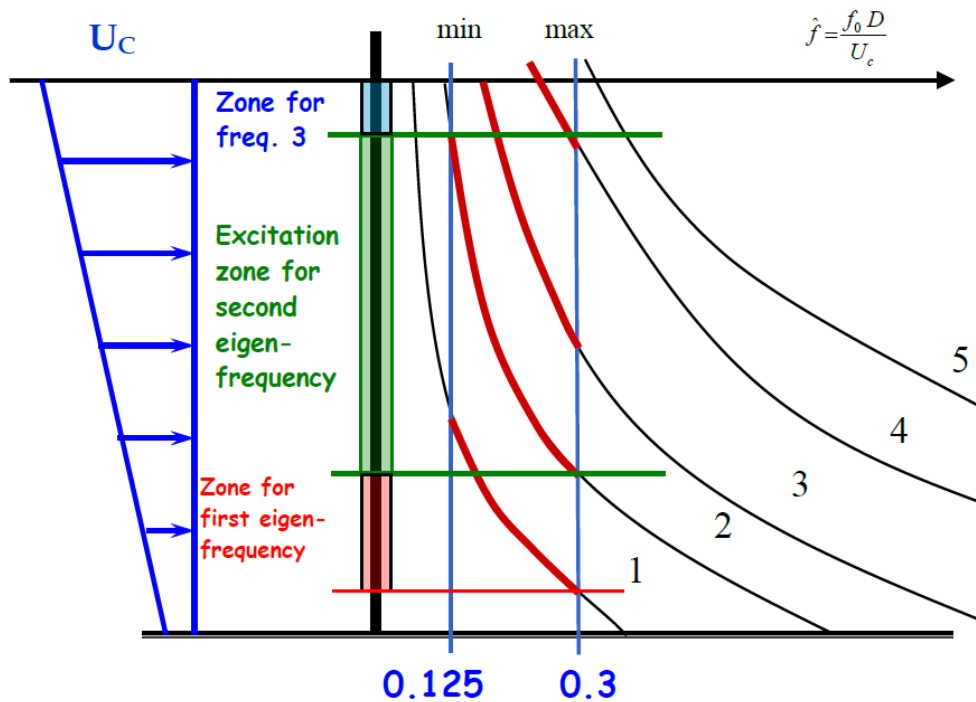


Figure 3.10 Space sharing process (Passano et al., 2014)

3.4.2 Time sharing

In the time sharing method, each response frequency will act within its whole excitation zone; however, only one frequency can be active in the same time. The duration of acting is governed by the value of an excitation parameter E_i (see Section 3.4.1) and is following:

$$T_i = T \frac{E_i}{\sum_{n=1}^k E_n}, \quad (3.7)$$

where E_n is the excitation parameter for frequency n , k is the total number of acting frequencies.

After some time, the other competing frequency will replace the previous one and start to control the motion along the structure (see Figure 3.11).

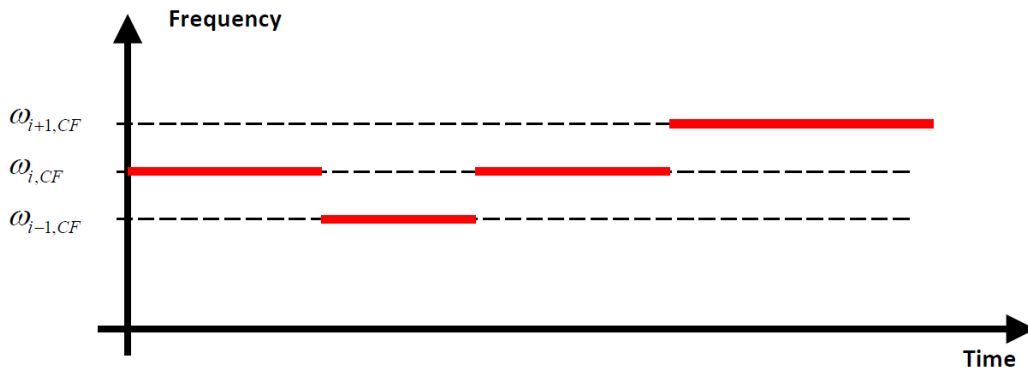


Figure 3.11 Illustration of the time sharing process (Passano et al., 2014)

Compared to the space sharing method, the excitation zones may overlap, but they cannot be active simultaneously (see Figure 3.12).

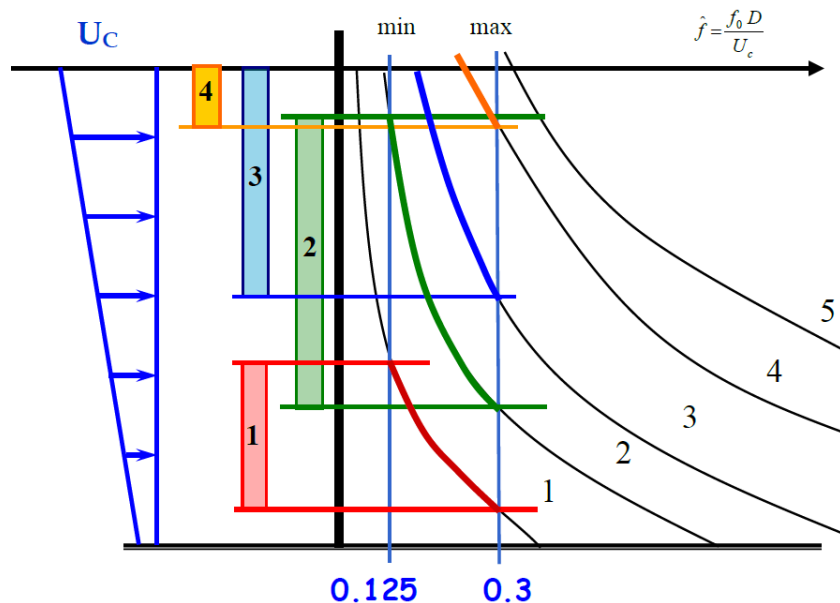


Figure 3.12 Excitation zones according to the time sharing process (Passano et al., 2014)

Chapter 4

VIV analysis of a typical deepwater SLWR

There are several VIV examinations that have been performed on the SCRs considering the riser-soil interactions. The aim of these investigations is to estimate the riser fatigue life at the touch down area including the riser-soil interaction forces.

One of the most indicative methods has been proposed by Larsen and Passano (2006) applies VIVANA (described in Chapter 3) with RIFLEX module. As VIVANA program, RIFLEX is based on FEM and is developed to analyze (static and dynamic analysis) the slender marine structures subjected to waves and currents. The dynamic analysis in VIVANA is carried out in frequency domain. However, the riser behavior in the water is highly non-linear. Such non-linear effects as tension variations, large deformations, pipe-soil interaction are significant and can be considered in time domain. The combination of RIFLEX and VIVANA allows us to perform reliable VIV analysis including non-linear structural effects.

As it was mentioned before, designs of SLWR and SCR are quite similar excepting the buoyancy part of the lazy wave riser. Thus, there is a strong need to perform the VIV analysis of SLWR considering the pipe-soil interaction forces. In the present thesis, SLWR VIV analysis has been performed using VIVANA program. This analysis includes the following aspects:

- Combined CF and IL motions;
- The elastic spring soil model;
- Different buoyancy element configurations;
- Time and space sharing methods;
- Realistic non-uniform current profiles.

In order to understand behavior and fatigue performance of deepwater SLWR, the base case analysis has been performed. Two types of flow have been considered in this analysis:

- Uniform flow (0.4 m/s);
- Different realistic non-uniform current profiles with probabilities of occurrence.

The combined CF and IL motions have been considered in this analysis. Two approaches have been used for the excitation zones identification: time and space sharing.

Stress amplitudes have been found in time and frequency domain (rain-flow counting and Rayleigh distribution respectively), and fatigue damage is calculated at 8 circumferentially-spaced points on the riser's cross-section (see Figure 4.1). Both IL and CF influences have been considered. The fatigue calculation is based on the user-defined SN curves and the riser responses computed in VIVANA. SN curve is obtained using the following formula:

$$N \cdot S^m = C, \quad (4.1)$$

where m is slope of the curve, N is the amount of cycles, S is the stress amplitude, C is the constant defining the SN curve. SN curve parameters for this particular case are the following: $m = 3$, $C = 11.533$ (data from the SINTEF Ocean Company).

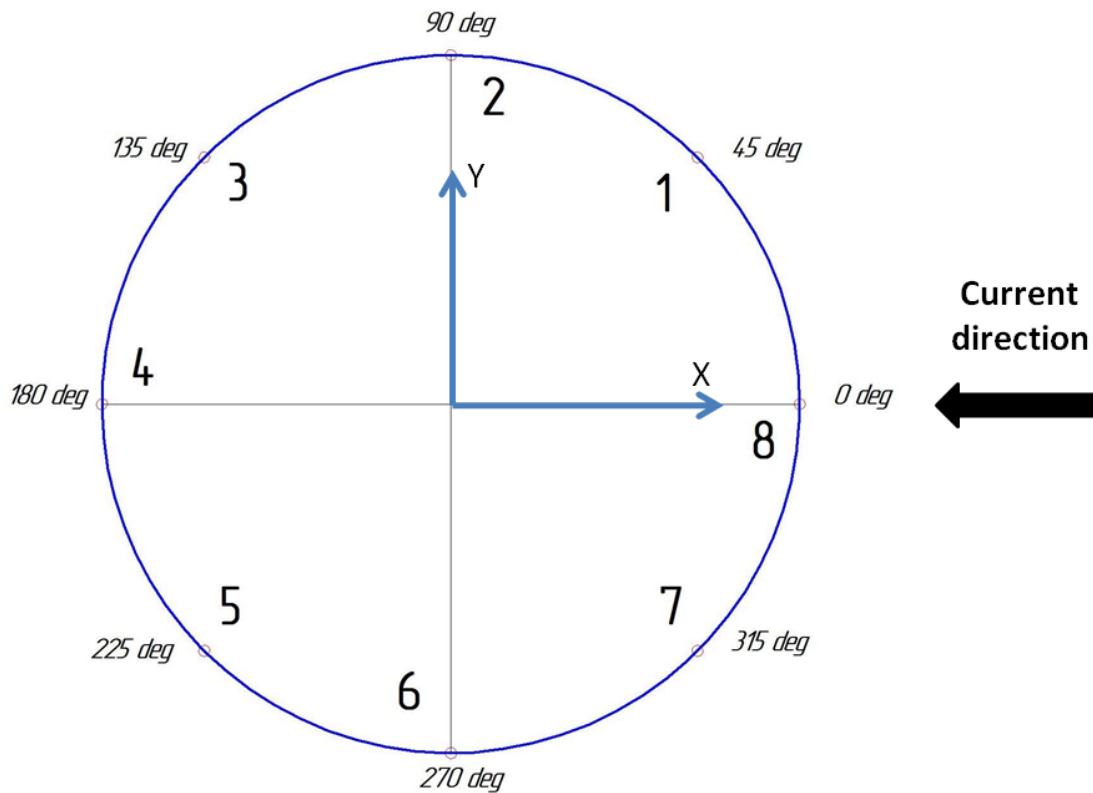


Figure 4.1 Points around the riser's circumference for fatigue calculation

4.1 The riser model

The riser model is constructed based on the data from the SINTEF Ocean Company. The main riser characteristics are presented in Table 4.1. All hydrodynamic data can be found in Appendix C.

Table 4.1 Riser model properties

Total riser length, m	3000
Inner diameter, mm	25.4
Pipe thickness, mm	2.63
Density of pipe material, kg/m ³	7850
Thickness of the buoyancy element, mm	7.62
Density of the buoyancy element, kg/m ³	700
Mass of the pipe, kg/m	0.2459
Mass of the buoyancy element, kg/m	1.199
Young modulus, E, GPa	207
Shear stiffness, G, GPa	80
Axial stiffness, EA, N	4.794*10 ⁶
Bending stiffness, EI, Nm ²	4.75*10 ⁴
Torsional stiffness, N/rad	3.671*10 ⁴

Figure 4.2 illustrates the deepwater SLWR configuration modelled in VIVANA. Buoyancy section for the base case is represented by simplified monolithic buoyancy element distributed along the whole zone (see Figure 4.3).

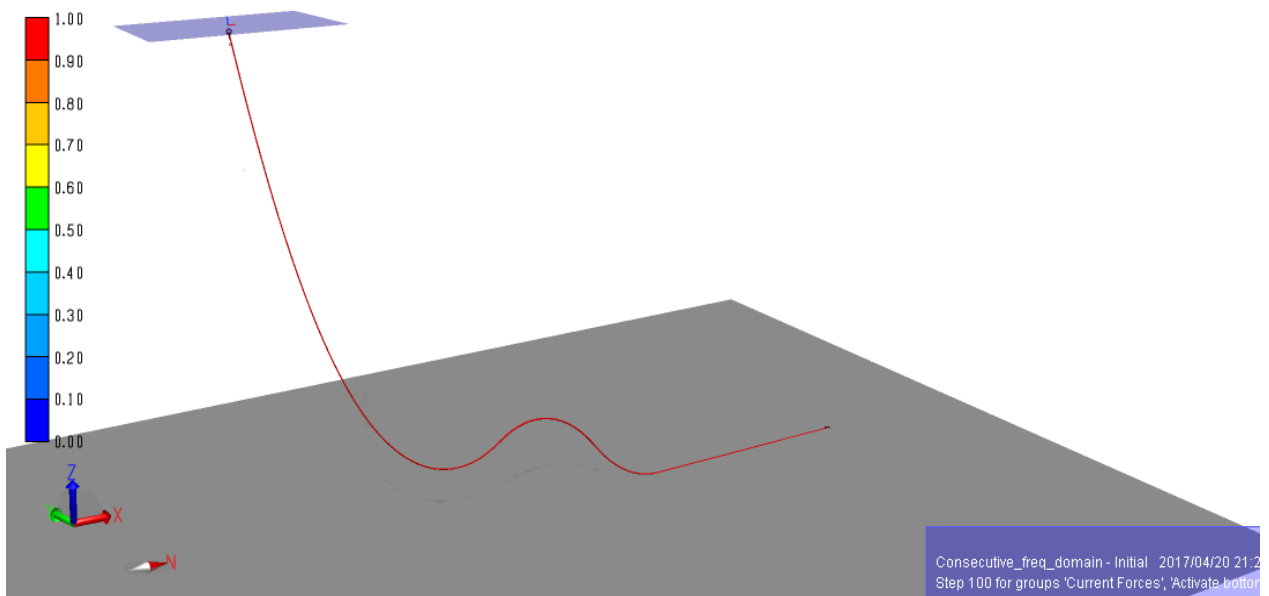


Figure 4.2 Steel lazy wave riser configuration modelled in VIVANA (static shape)

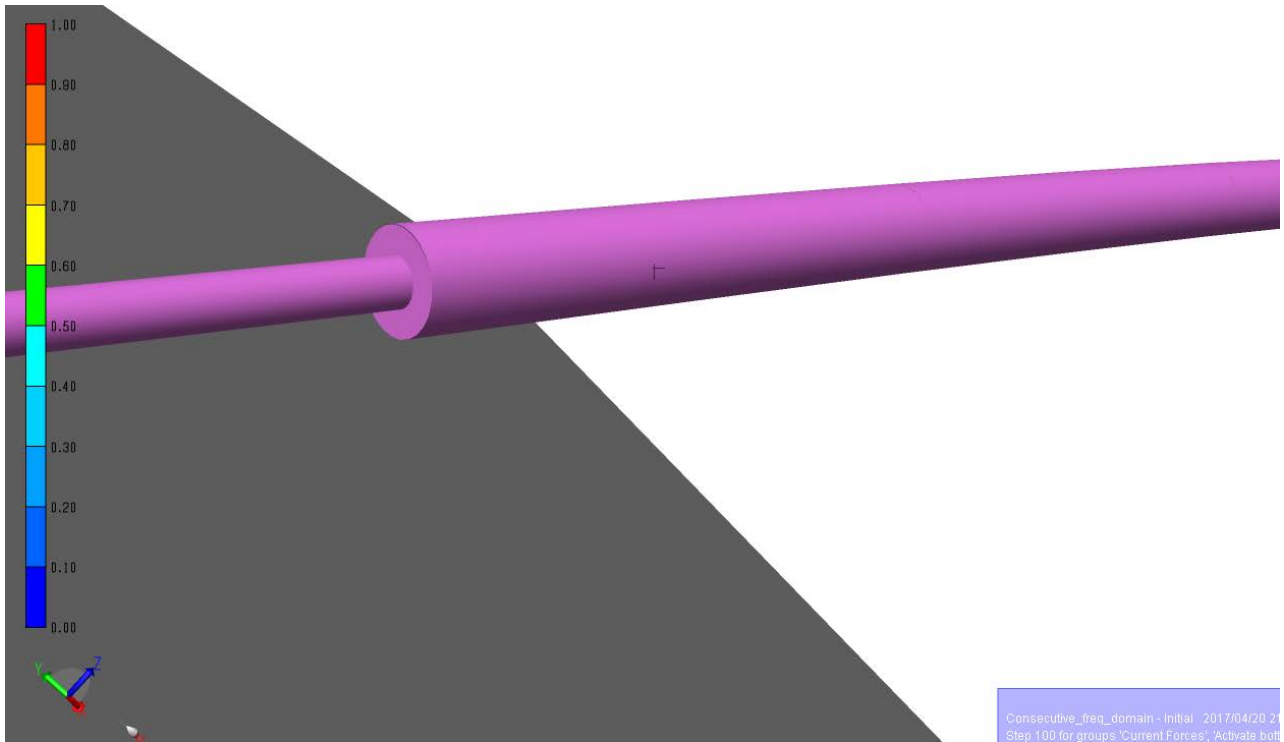


Figure 4.3 Monolithic buoyancy module for the base case analysis

4.2 The soil model

In the present VIVANA model, soil is represented by the set of the linear elastic springs providing contact with the seafloor and its friction in different directions (data is provided by the SINTEF Ocean Company). Table 3 represents the data used for the soil modelling. No damping is used in this analysis; each spring will only reflect some part of the riser energy. Riser displacements are proportional to the soil-riser interaction forces. Chosen model is suitable for this analysis since it considers the bottom segment of the riser (in the present work, the bottom segment is varying between 650-750 meters depending on the SLWR configuration).

Table 4.2 Soil model properties (SINTEF Ocean Company)

Spring stiffness direction	Stiffness value, N/m
Vertical	$5 \cdot 10^4$
Axial	$2 \cdot 10^5$
Lateral	$2 \cdot 10^5$

4.3 Analysis results for uniform flow

Combined CF and IL motions were considered for this analysis. Both time and space sharing methods have been performed. Results were obtained and compared in terms of the response amplitude, mode number, response frequency and the total accumulated fatigue damage.

4.3.1 Response frequencies and mode numbers

Since the riser has buoyancy section with bigger diameter, this section will have a smaller shedding frequency (see Formula 2.2). This means that the lower frequency and mode will be excited by the buoyancy part.

For the space sharing option, both bare and buoyancy part are excited by single frequencies. For the CF motions, the frequency with magnitude 0.146 Hz and mode number 22 dominates along the bare part of the riser. Buoyancy part is dominated by frequency with magnitude 0.118 Hz and mode number 18. This means that the frequencies 0.146 Hz and 0.118 Hz have the largest excitation parameter among all candidate frequencies along the bare and buoyancy parts of the riser respectively. Dominating IL frequencies as well as the mode numbers are primarily twice larger than the CF ones and will not be mentioned in this section.

For the case with the time sharing option as expected several different frequencies with magnitudes 0.124 Hz, 0.132 Hz, 0.138 Hz and 0.146 Hz have been alternatively excited and acting along the bare cylinder. Mode numbers have been varied from 19 to 22. Dominating frequencies for the buoyancy part are 0.056 Hz, 0.063 Hz, 0.070 Hz, 0.076 Hz, 0.083 Hz, 0.089 Hz, 0.097 Hz and 0.103 Hz with modes from 9 to 16. The frequencies as well as the mode numbers are proportional to the diameters of the riser's cross-sections. Since the bare and buoyancy parts of riser have outer diameters 0.459 m and 0.977 m respectively, so the frequencies of bare and buoyancy parts should differ by a factor of around 2 (during the constant current speed; see Formula 2.2). This agrees well to the obtained results. There are also two frequencies of 0.110 Hz and 0.118 Hz (with mode numbers 17 and 18 respectively) which dominate along both bare and buoyancy parts.

4.3.2 Response amplitudes

Space sharing option showed that the CF response amplitudes have the peak (0.53 m) in the hang-off catenary part of SLWR (see Figure 4.4). Bare and buoyancy parts of the riser are represented by blue and red lines respectively. Decrease of the amplitude corresponds to the buoyancy section of riser. Amplitudes end at TDP where the riser touches the seafloor. The IL response amplitudes have the maximum (0.12 m) at boundaries of the buoyancy section (see Figure 4.5). The buoyancy catenary part of SLWR has smaller displacements due to bigger diameter. Both CF and IL maximum response amplitudes are dominated by the frequencies of bare part of the riser.

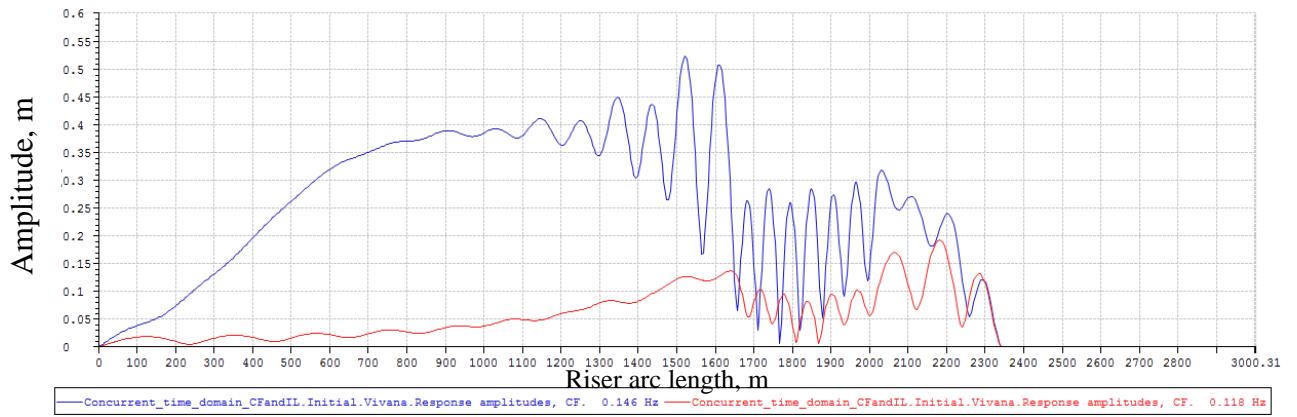


Figure 4.4 CF response amplitudes (space sharing)

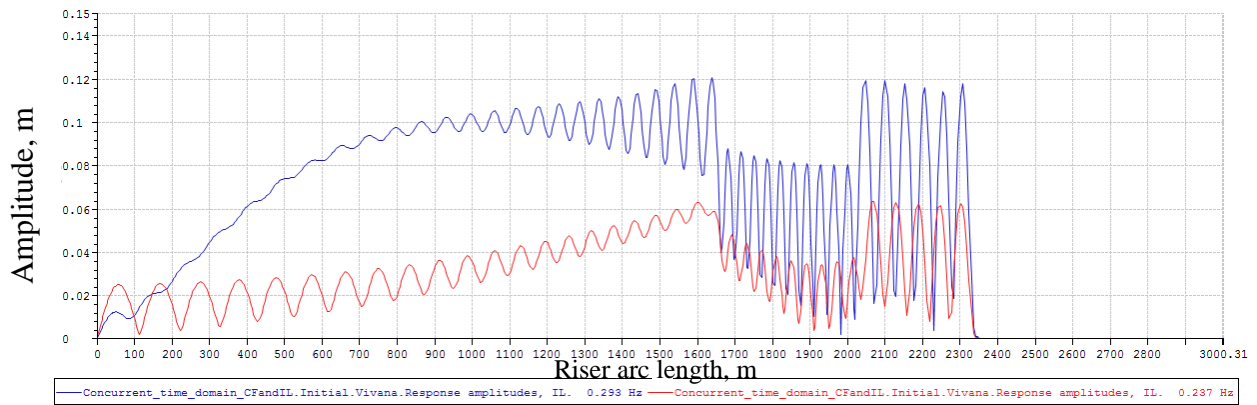


Figure 4.5 IL response amplitudes (space sharing)

The other picture is seen in the time sharing option. Figures 4.6 and 4.7 illustrate the CF response amplitudes for bare and buoyancy parts respectively.

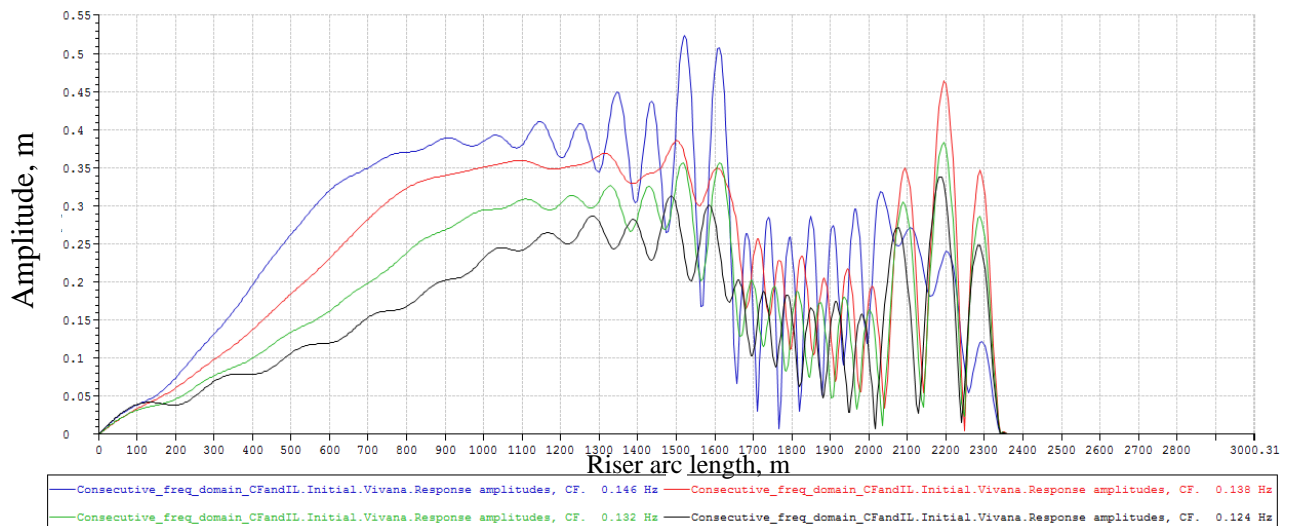


Figure 4.6 CF response amplitudes of bare part (time sharing)

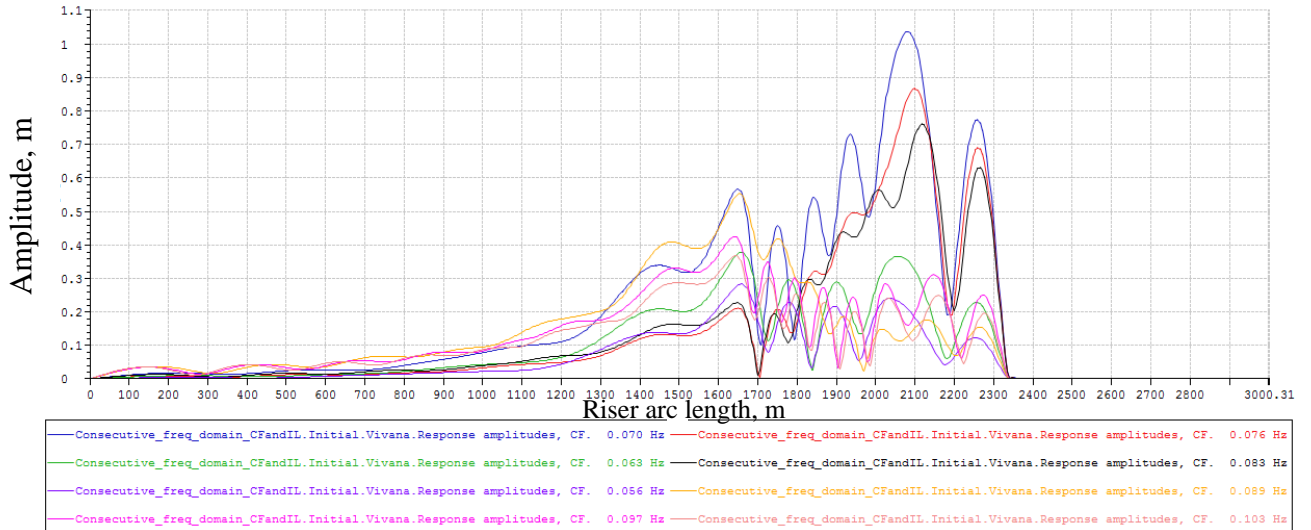


Figure 4.7 CF response amplitudes of buoyancy part (time sharing)

The maximum CF response amplitudes for the time sharing option are shown in Figure 4.8. As in the space sharing case, bare part of the riser has the maximum CF response (0.53 m) at frequency 0.146 Hz. Buoyancy part has the maximum CF amplitude (1.03 m) at frequency with magnitude 0.070 Hz.

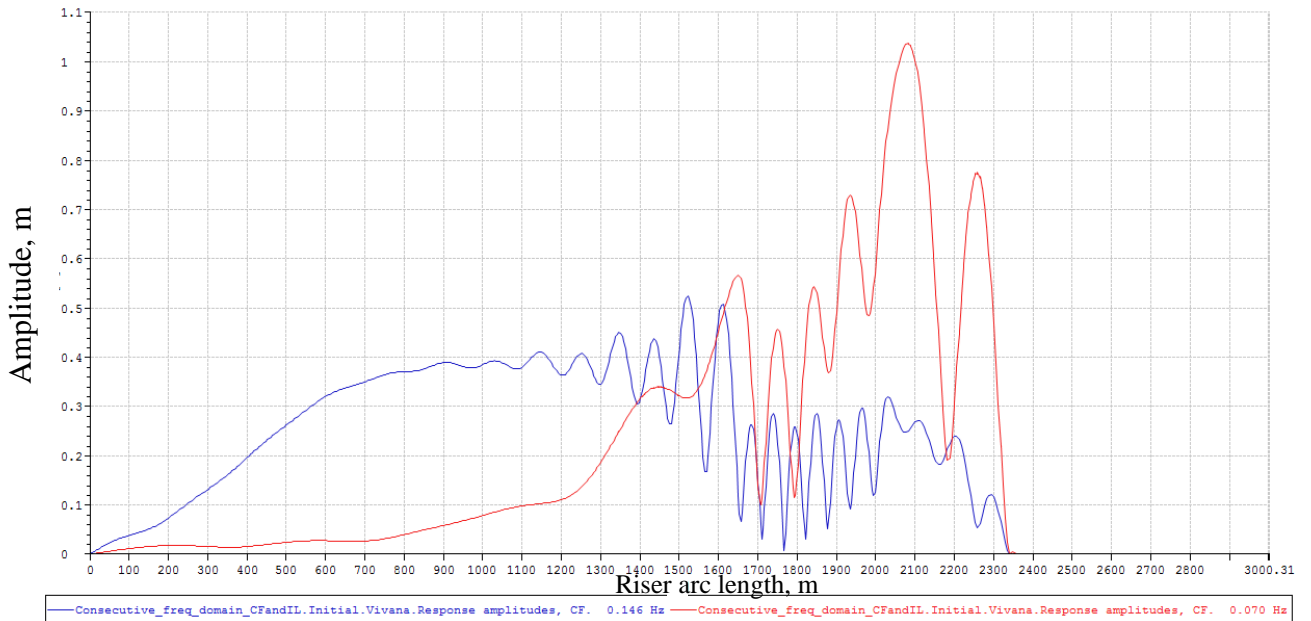


Figure 4.8 Maximum CF response amplitudes (time sharing)

The IL response amplitudes for bare and buoyancy parts are illustrated in Figures 4.9 and 4.10 respectively. Generally, CF response amplitudes (for bare and buoyancy parts) are larger than IL ones by a factor of 3.

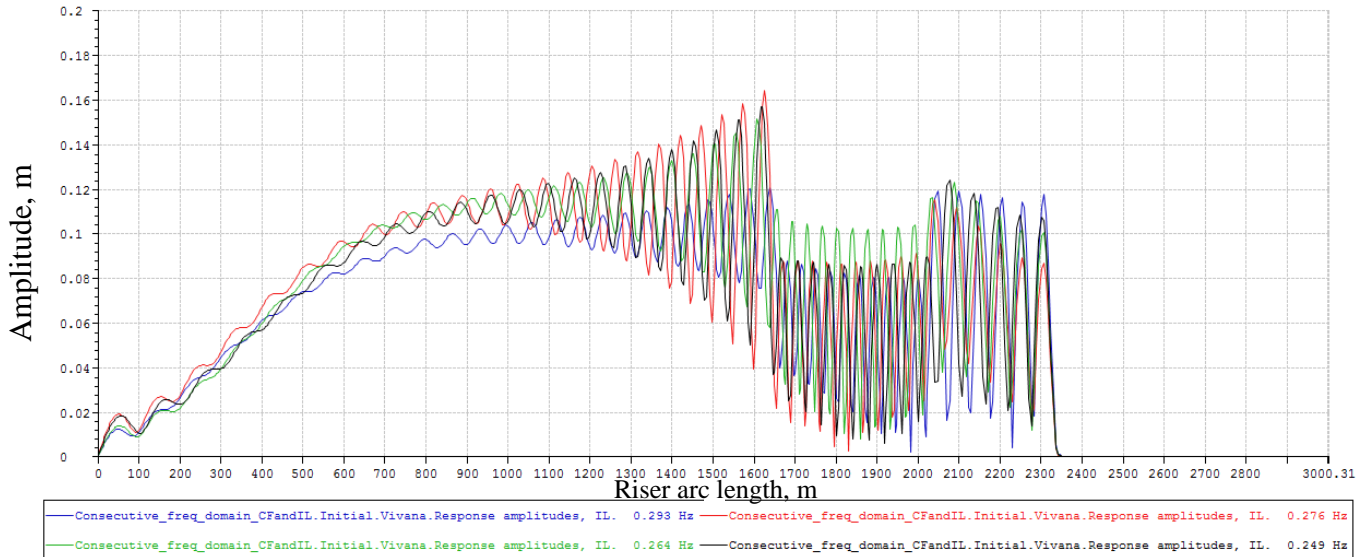


Figure 4.9 IL response amplitudes of bare part (time sharing)

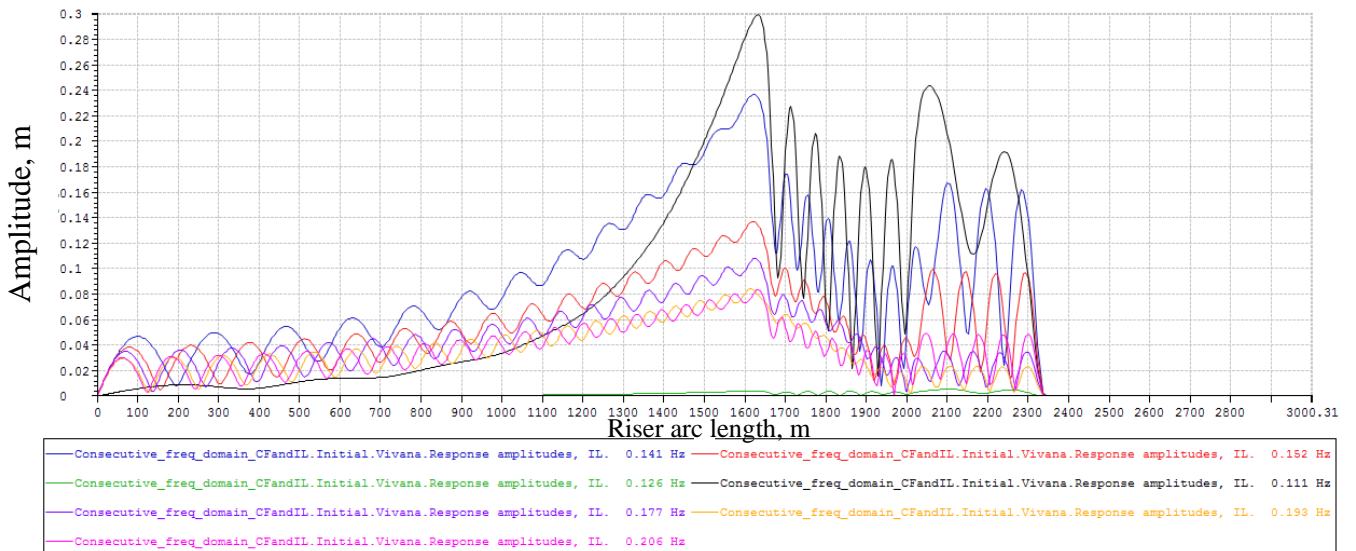


Figure 4.10 IL response amplitudes of buoyancy part (time sharing)

Maximum IL response amplitudes for the time sharing method are shown in Figure 4.11. The absolute maximum (0.3 m) is located in the hang-off catenary section of SLWR near the buoyancy catenary and belongs to the IL frequency 0.111 Hz.

Unlike the space sharing method, in the time sharing option, both CF and IL maximum response amplitudes are governed by the frequencies of buoyancy section.

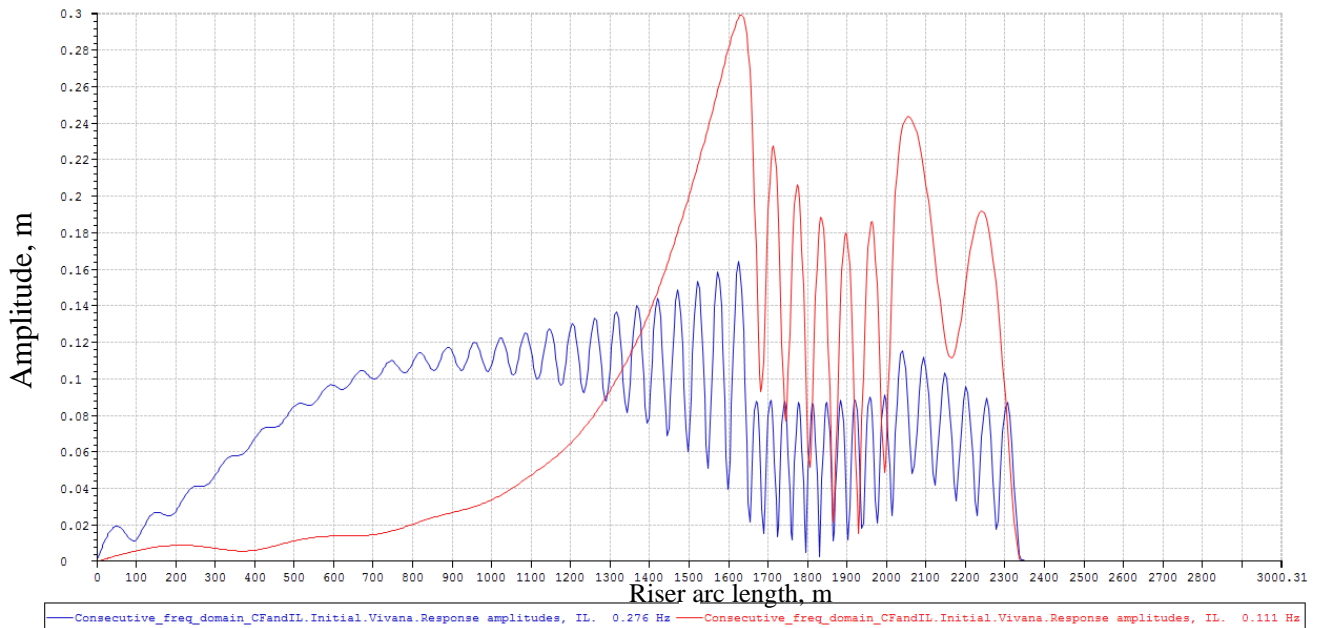


Figure 4.11 Maximum IL response amplitudes (time sharing)

4.3.3 Fatigue damage

As it was mentioned before, fatigue damage has been calculated for 8 points around the cylinder’s cross-section (see Figure 4.1). Points 1, 2, 3, 4 are diametrically opposite to the points 5, 6, 7, 8, respectively, and they have almost identical values of the fatigue damage. Thus, in this analysis, fatigue damage is calculated at 45 degrees, 90 degrees (CF case), 135 degrees and 180 degrees (IL case), which corresponds to the points from 1 to 4.

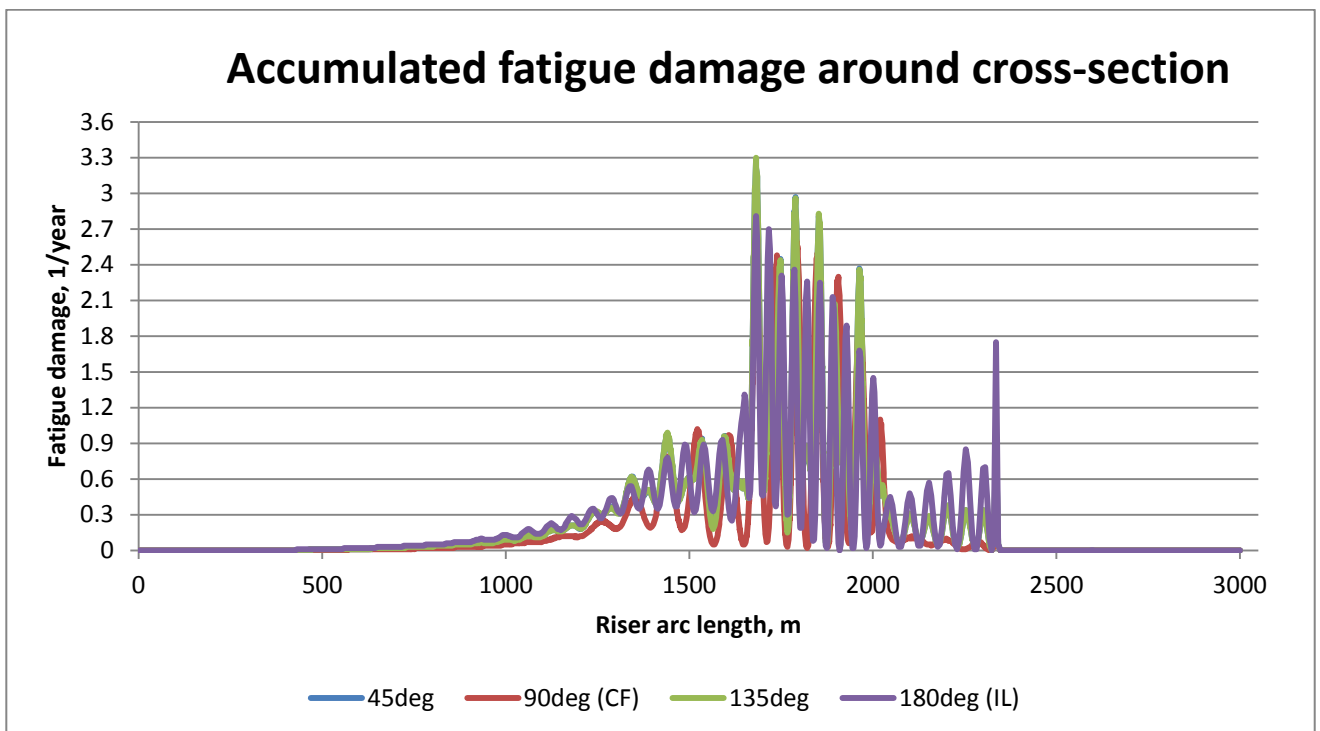


Figure 4.12 Accumulated fatigue damage for the space sharing method

Figure 4.12 illustrates the accumulated fatigue damage around cross-section for the space sharing option considering combined CF and IL motions in uniform flow. Two different peaks are observed: highest one corresponds to the buoyancy section and another is at TDP. The maximum value of fatigue (3.3 1/year) corresponds to 45 and 135 degrees (points 1 and 3). The peak at TDP is a consequence of the riser-soil interaction forces. The highest value of this peak (1.77 1/year) is observed at 180 degrees (IL motions).

Time sharing method also showed peaks in both buoyancy section and TDP, but in this case, the maximum accumulated fatigue damage (0.75 1/year) is observed at 180 degrees (see Figure 4.13). Peak value at TDP is 0.69 1/year and is found at 90 degrees.

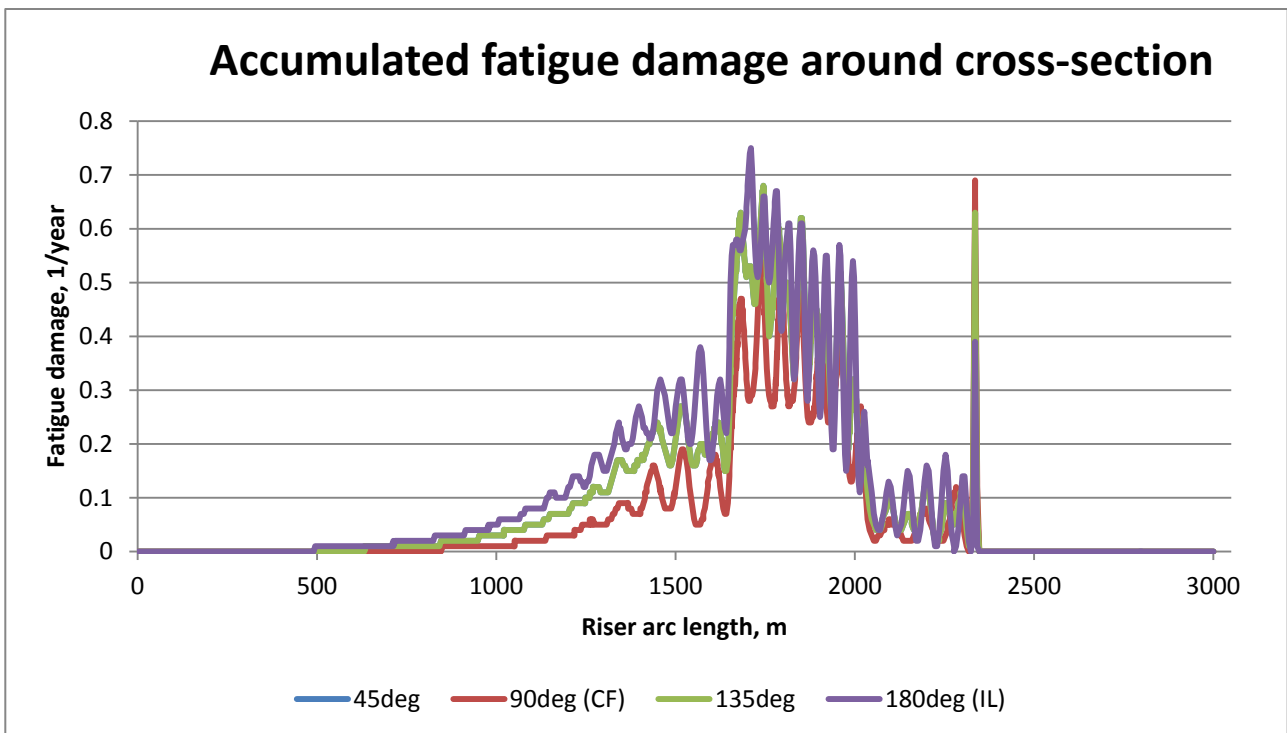


Figure 4.13 Accumulated fatigue damage for the time sharing method

Based on the results, the absolute maximum fatigue damage from the space sharing method is ~4.4 times larger than damage calculated from the time sharing. The results have been summarized in Table 4.3.

Table 4.3 Fatigue damage results for combined CF and IL case

Method	Max. fatigue damage in the buoyancy section	Max. fatigue damage at TDP
Space sharing	3.3 1/year (135 deg.) – max fatigue along the riser	1.77 1/year (180 deg.)
Time sharing	0.75 1/year (180 deg.) – max fatigue along the riser	0.69 1/year (90 deg.)

It should be noted that the fatigue damage at TDP for the time sharing method is more significant than for the space sharing option.

4.4 Analysis results for non-uniform flow

In this case, 21 realistic non-uniform current profiles have been used for the analysis (see Figure 4.14). Each current has its own probability of occurrence (Wu et al., 2017; see Appendix D). The heading of current is perpendicular to the riser for all cases. The analysis has been made in terms of the fatigue damage comparison around the points on the riser's circumference for the time and space sharing methods.

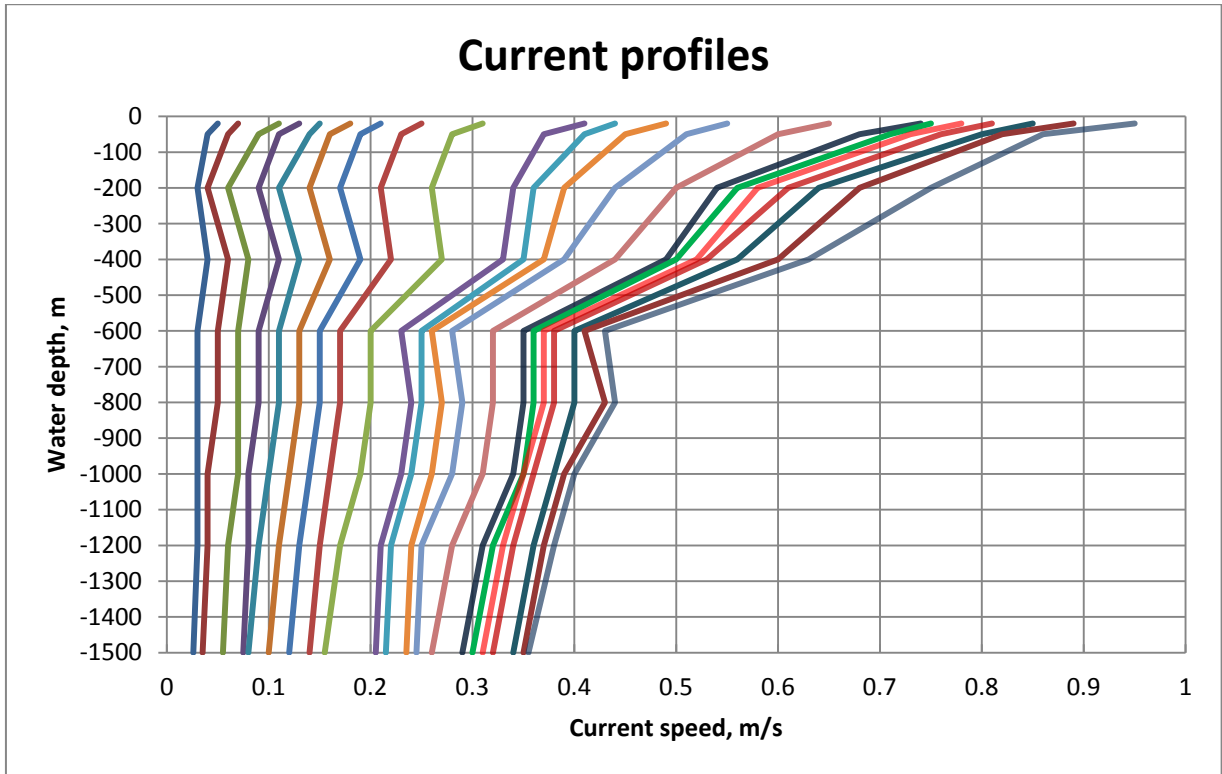


Figure 4.14 Realistic non-uniform current profiles (Wu et al., 2017)

The accumulated fatigue along the riser (including currents probabilities of occurrence) can be found by the following formula:

$$fat(z) = \sum_{c_i=1}^{21} fat(z, c_i) \cdot P(c_i), \quad (4.2)$$

where $fat(z, c_i)$ is the fatigue damage at the point z of the riser for a given current profile c_i and $P(c_i)$ is the probability of occurrence for each profile.

In the space sharing option, the accumulated CF and IL fatigue damage considering probabilities of occurrence is presented in Figure 4.15. Fatigue damage at 90 degrees is generally prevailing along the riser length and has its maximum (0.029 1/year) at TDP. The maximum fatigue in the buoyancy section is 0.017 1/year.

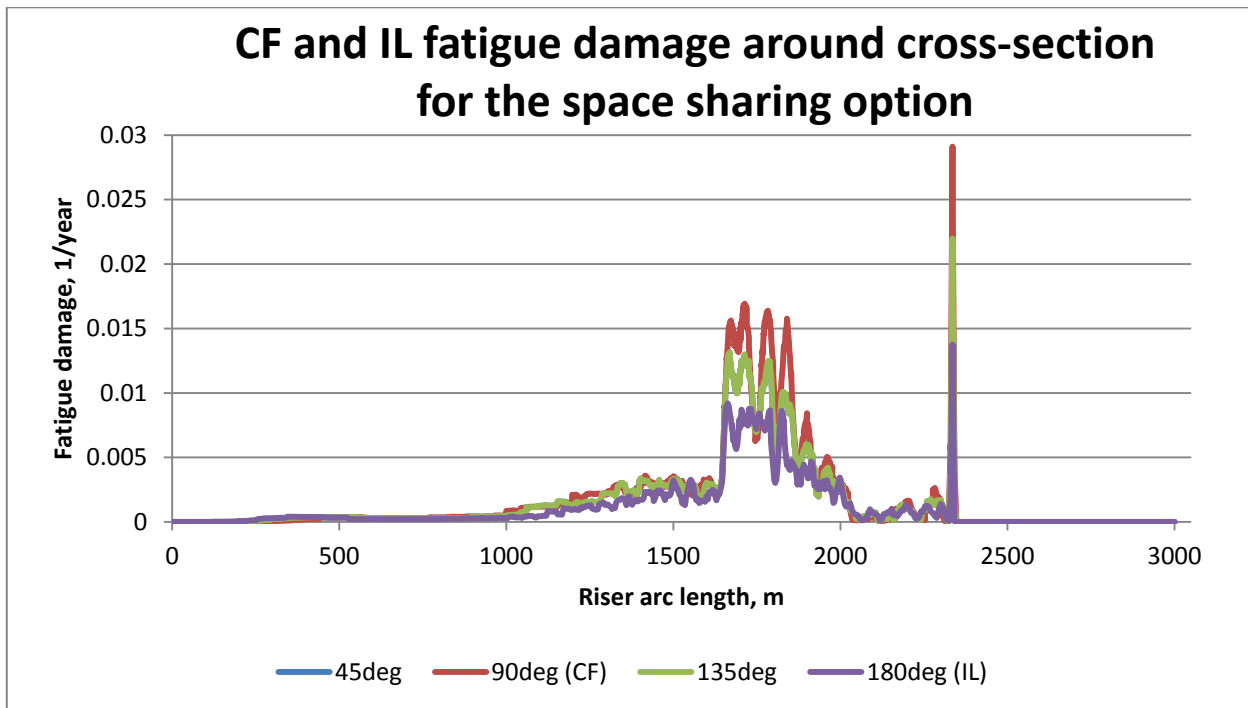


Figure 4.15 Accumulated CF and IL fatigue damage for the space sharing option (including probabilities of occurrence)

The similar picture is seen for the time sharing method (see Figure 4.16). The maximum fatigue damage (0.017 1/year) is observed at TPD. The peak value of fatigue in the buoyancy part is 0.011 1/year.

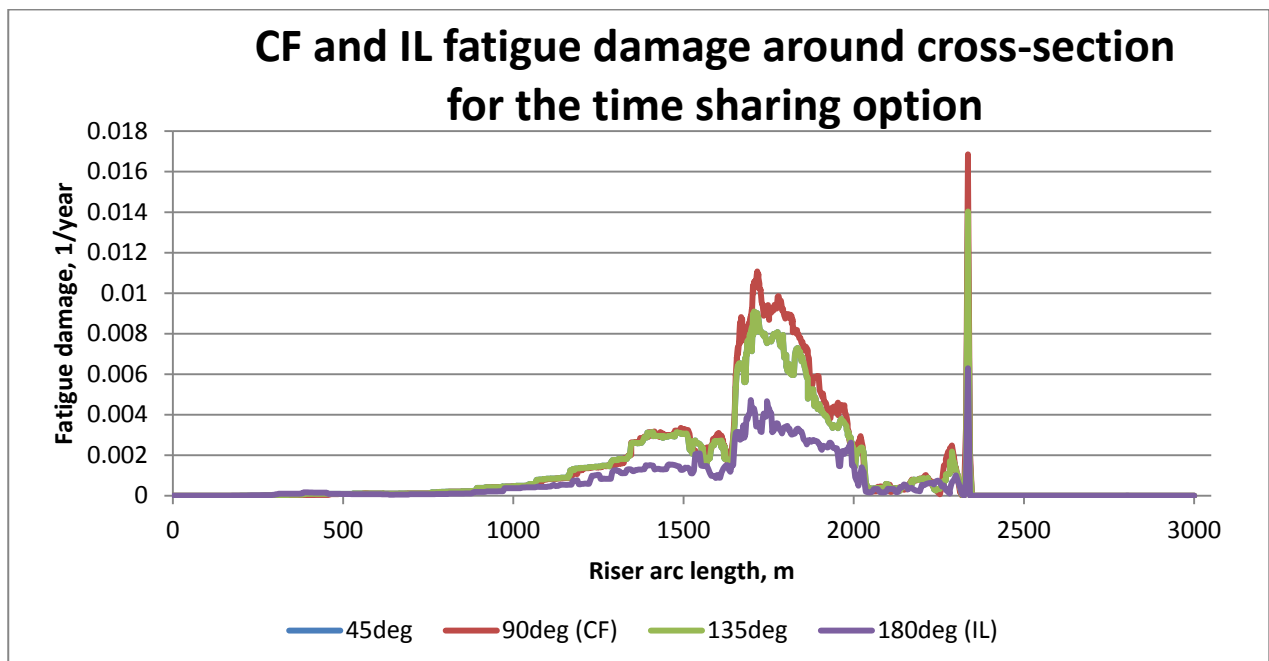


Figure 4.16 Accumulated CF and IL fatigue damage for the time sharing option (including probabilities of occurrence)

Figure 4.17 shows the maximum CF and IL fatigue damage in contrast with the maximum current speed for each profile for the space sharing method. It should be noted that the exact

values of fatigue damage have been taken for these comparisons (probabilities of occurrence are not considered). This has been made to observe the clear response with increasing flow speed.

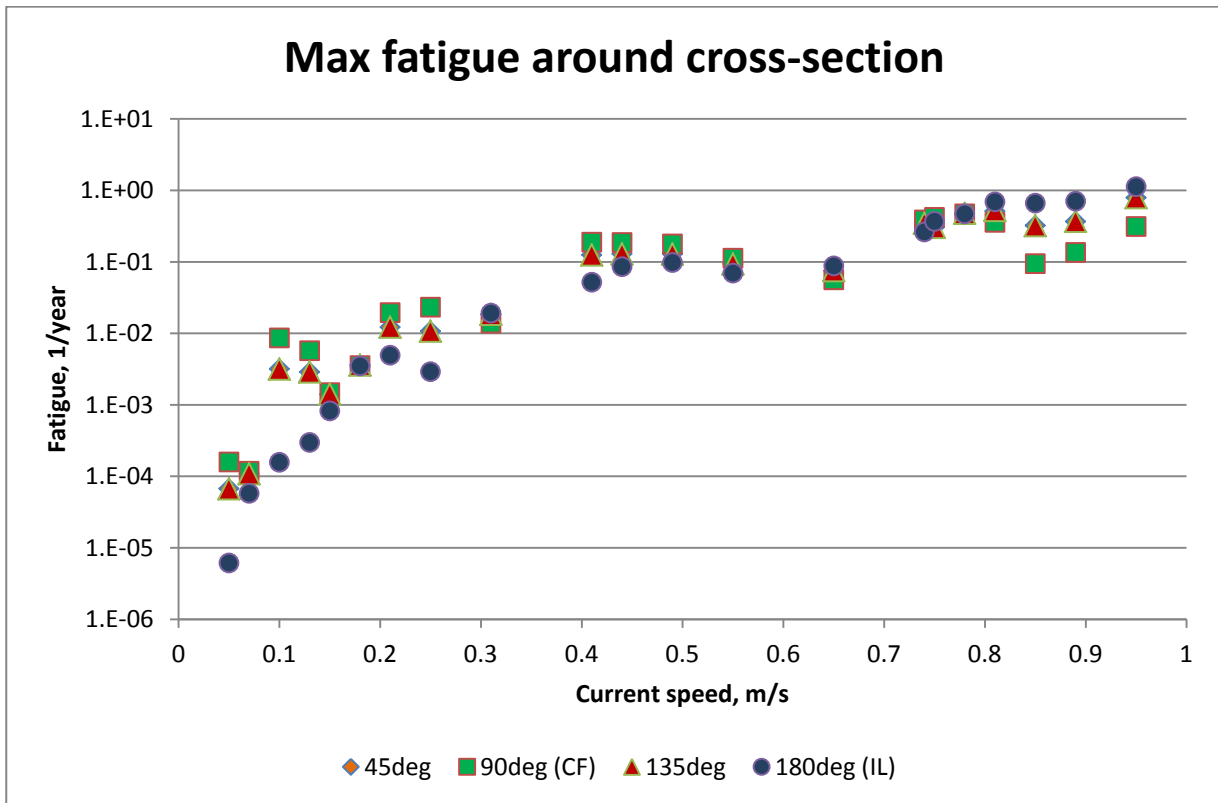


Figure 4.17 Maximum fatigue damage comparison for the space sharing option (excluding probabilities of occurrence)

The CF fatigue damage is primarily dominating at lower current speeds from 0.05 m/s up to 0.8 m/s (82% of cases). The other points (18%) are slightly dominated by the fatigue calculated at 45 or 135 degrees (0.18 m/s) and at 180 degrees (0.3 m/s, 0.65 m/s). However, with increasing current speed (> 0.8 m/s) the IL fatigue damage replaces the CF one and becomes dominating. The fatigue damage calculated from 45 and 135 degrees also starts to prevail over the CF fatigue. The maximum fatigue damage in this case corresponds to the maximum flow speed and is 1.12 1/year. It should be noted, that the fatigue damage generally grows with the growing current speed.

For the time sharing option, CF fatigue is dominating for 90% of all cases. The maximum value is observed at the current speed of 0.89 m/s and is 0.411 1/year. Figure 4.18 shows the maximum fatigue comparison around riser cross-section for the time sharing option. For the point with the flow speed 0.18 m/s (yellow point), the maximum fatigue damage spontaneously decreased. This case will be discussed in the Chapter 6.

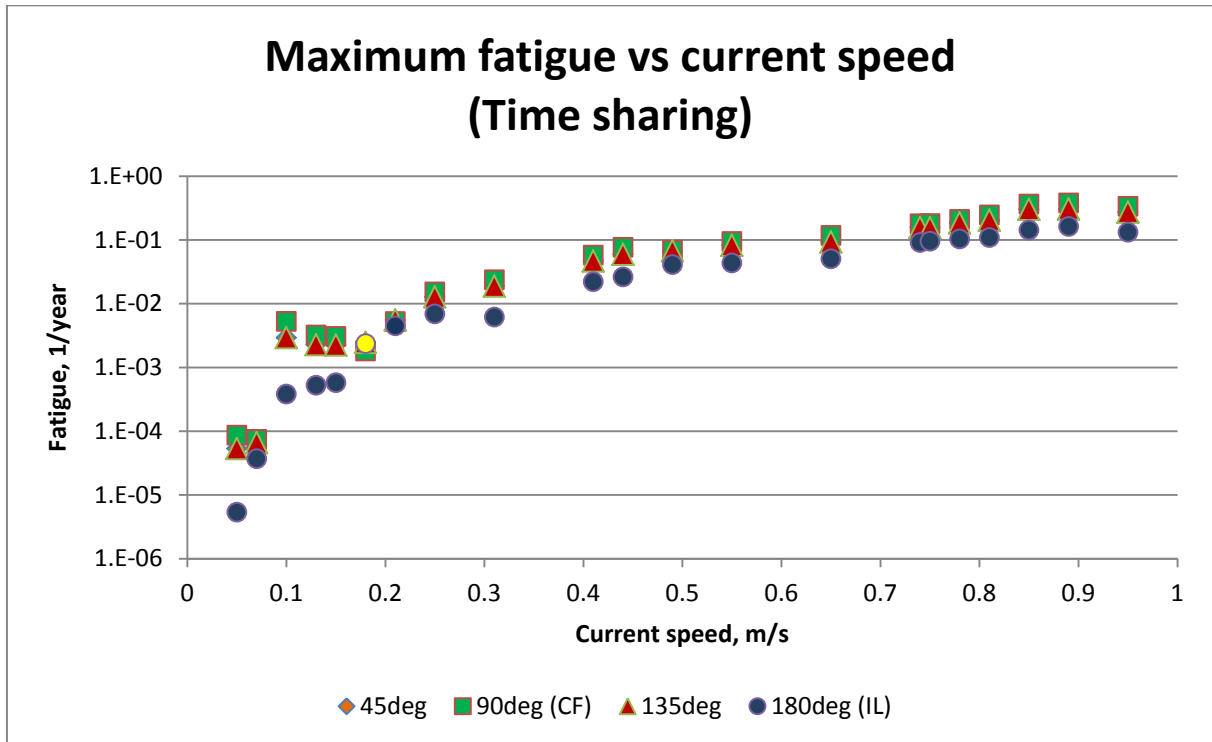


Figure 4.18 Maximum fatigue damage comparison for the time sharing option (excluding probabilities of occurrence)

During the base case analysis, several important observations have been made:

- The maximum fatigue damage results from the space sharing case are in general higher than the results obtained using the time sharing option;
- The vortex shedding frequency of the bare riser is higher than of the buoyancy part since the diameter of bare part is lower. This means that the bare section of the riser excites higher modes, as expected;
- Accumulated fatigue results along the riser length always give two peaks: one is in the buoyancy section and another is at TDP due to the riser-soil interaction forces at the sea bottom;
- Fatigue damage at TDP is relatively more critical for the time sharing option;
- For the non-uniform flow, the maximum CF and IL fatigue is observed mostly at 90 degrees (CF direction). However, in the space sharing method, with increasing current speed IL fatigue becomes more significant;
- Current profile with the maximum speed of 0.18 m/s is critical for both the space and time sharing methods since it shows spontaneous decrease of the maximum fatigue damage.

Chapter 5

Sensitivity study: different buoyancy element arrangement

When the steel lazy wave riser is subjected to vortex-induced vibrations, the vortex shedding process will be different for bare and buoyancy parts due to the difference in diameters. The interaction between these parts can be influenced by several parameters, such as the aspect ratio of the buoyancy element, arrangement of the buoyancy elements, buoyancy elements spacing, etc. These parameters are vital to determine the VIV responses of the SLWR. Thus, there is a challenge to achieve the proper design of SLWR to diminish the VIV responses and hence to obtain the better fatigue life. The buoyancy section is a critical part of the SLWR since both bare and buoyancy parts may experience VIV which leads to rapid accumulation of the fatigue damage. Hence it is important to analyze the vortex-induced forces and VIV responses of different buoyancy element configurations.

Experiments to obtain the set of hydrodynamic data for different staggered buoyancy element configurations of SLWR have been performed in the SINTEF Ocean Company (formerly MARINTEK).

Based on the provided hydrodynamic data (see the next Section), two riser models with staggered buoyancy elements has been made in VIVANA program using the riser model data from the base case. Results have been compared in terms of the maximum fatigue damage around the riser's cross-section. All main observations and conclusions have been made and discussed.

5.1 Hydrodynamic data acquisition

The experiment has been carried out in the Ocean Laboratory of the SINTEF Ocean Company. Two different buoyancy element configurations have been considered as illustrated in Figure 5.1. The only difference between these configurations is the spacing of the buoyancy modules: 1st configuration has the length of the gap between two neighboring

buoyancy elements L_c equal to the length of one buoyancy element L_b (coverage percentage of buoyancy elements is 50%); 2nd configuration has $L_c=2*L_b$ (33% coverage).

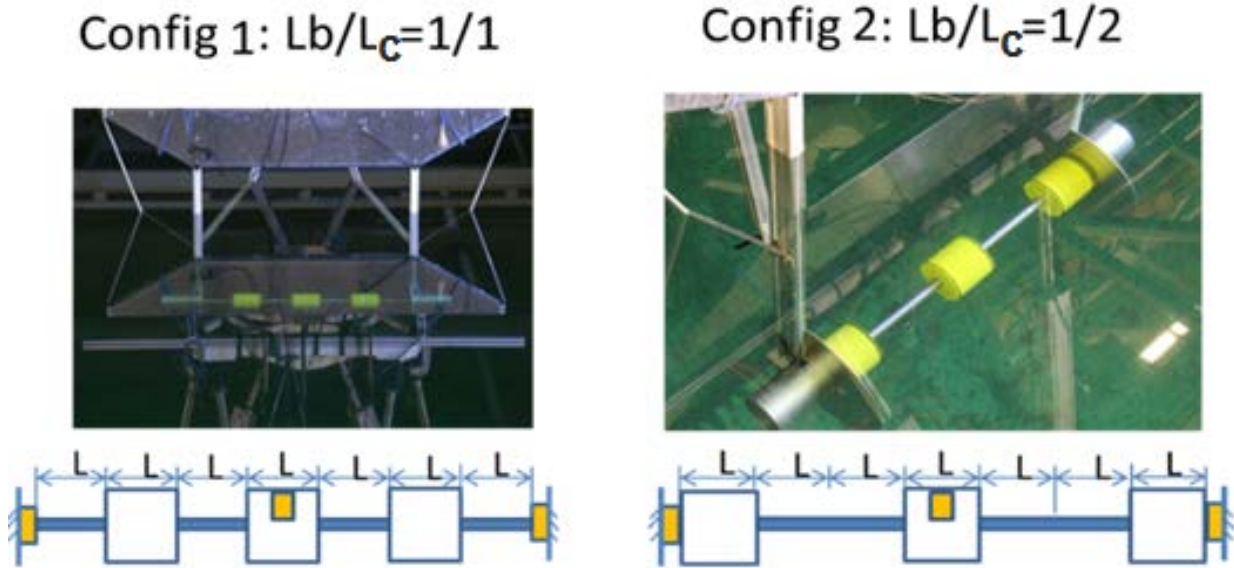


Figure 5.1 Test configurations (Wu et al., 2017)

The experiment consists of two types of tests: stationary test and test with forced CF motions. Force transducers have been used to estimate the hydrodynamic forces. During the tests, the following parameters have been obtained:

- Excitation coefficients;
- Drag coefficients;
- Added mass coefficients.

The riser and buoyancy element materials and geometric data are described in Table 5.1.

Table 5.1 Riser and buoyancy element properties (Wu et al., 2017)

	Riser	Buoyancy element
Material	Steel	ABS material
Length L, m	1.05	0.15
Outer diameter D, m	0.03	0.15
Aspect ratio L/D	35	1
Buoyancy/bare diameter ratio D_b/D_r	5	

The hydrodynamic data obtained from the experiment for both test configurations have been used as input for the VIVANA VIV prediction tool and showed a good prediction against the NDP high mode VIV tests over the flexible cylinder with staggered buoyancy elements (see Section 2.2.2.3; Braaten and Lie, 2005). The input data is summarized in Table 5.2. The detailed results of this experiment can be found in (Wu et al., 2017).

Table 5.2 Summarized input parameters (Wu et al., 2017)

Configuration	Excitation coefficient C_e		Excitation zone \bar{f}		Added mass C_a	
	Riser	Buoyancy	Riser	Buoyancy	Riser	Buoyancy
Lb/Lc=1/1	C_e curve 1	C_e curve 2	0.16-0.22	0.06-0.12	10.0	2.0
Lb/Lc=1/2	C_e curve 1	N/A	0.16-0.22	N/A	10.0	2.0

Based on the obtained hydrodynamic data, the CF excitation force coefficient curves have been made for the bare and buoyancy parts of the riser (see Figure 5.2).

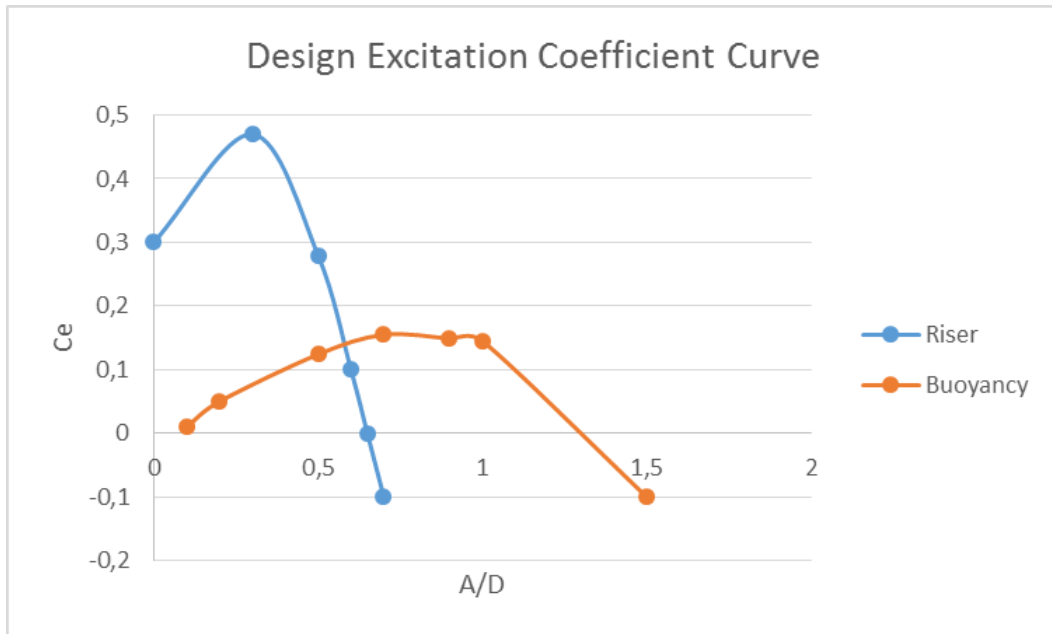


Figure 5.2 Design excitation coefficient curves (Wu et al., 2017)

The major observations have been made based on the results obtained in this experiment (Wu et al., 2017):

- Since the riser has bare and buoyancy parts of different diameters, two vortex shedding processes appear in bare and buoyancy parts;
- As a consequence from the first observation, when the bare part of the riser is excited, the buoyancy section will provide damping (will be outside of the bare part excitation region) and vice versa;
- With the increased spacing between two buoyancy elements (2nd configuration Lb/Lc=1/2), the buoyancy part will be always in damping region (no VIV responses at buoyancy frequency).

5.2 Riser models with staggered buoyancy elements

Based on the experimental results from the previous section, the two riser configurations have been built in VIVANA software. The main objective for this research is to perform the

sensitivity analysis for different staggered buoyancy element configurations in terms of the riser fatigue life. This analysis is made by the comparison of the maximum accumulated fatigue damage between the base case SLWR model and two riser configurations with staggered buoyancy elements.

The 1st and 2nd riser configurations have the same bare riser properties as the riser model from the base case (see Table 4.1). The only difference is in the hydrodynamic data (see Table 5.2) and the geometry of the buoyancy elements. Figure 5.3 illustrates the main features and the schematic drawings of the riser configurations used in the present analysis.


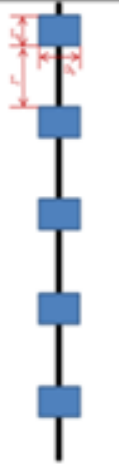
Configuration	1	2
Spacing Ratio (L_c/L_b)	1/1	2/1
Aspect Ratio (L_b/D_b)	1/1	1/1
Diameter Ratio (D_b/D_r)	5/1	5/1
Coverage (%)	50	33
Schematic drawing		

Figure 5.3 The main parameters of the SLWRs with different staggered buoyancy element configurations (Wu et al., 2016)

5.2.1 Static configurations

In order to perform the proper comparison, the new riser configurations should have similar static shapes with base case.

The amount of the buoyancy elements and the total length of the buoyancy section for 1st and 2nd configurations have been adjusted based on the total buoyancy force of the buoyancy section obtained from the base case. Calculated results are summarized in Table 5.3.

Table 5.3 Arrangement of the buoyancy elements

	Base case	1 st configuration (Lc/Lb=1/1)	2 nd configuration (Lc/Lb=2/1)
The length on one buoyancy element, m	3.161	2.295	2.295
Buoyancy element diameter, m	0.977	2.295	2.295
Bare riser outer diameter, m	0.459	0.459	0.459
Number of the buoyancy elements (attached together without gaps)	120	23	23
Number of gaps between two neighboring buoyancy elements	0	22	22
The length of gap, m	0	2.295	4.59
Total length of the buoyancy section, m	379.32	103.275	153.765
The buoyancy force per unit length, kN/m	7.531		

As a result, relatively similar static configurations have been obtained (see Figure 5.4). The discrepancy in shapes corresponds to the different lengths of the buoyancy sections.

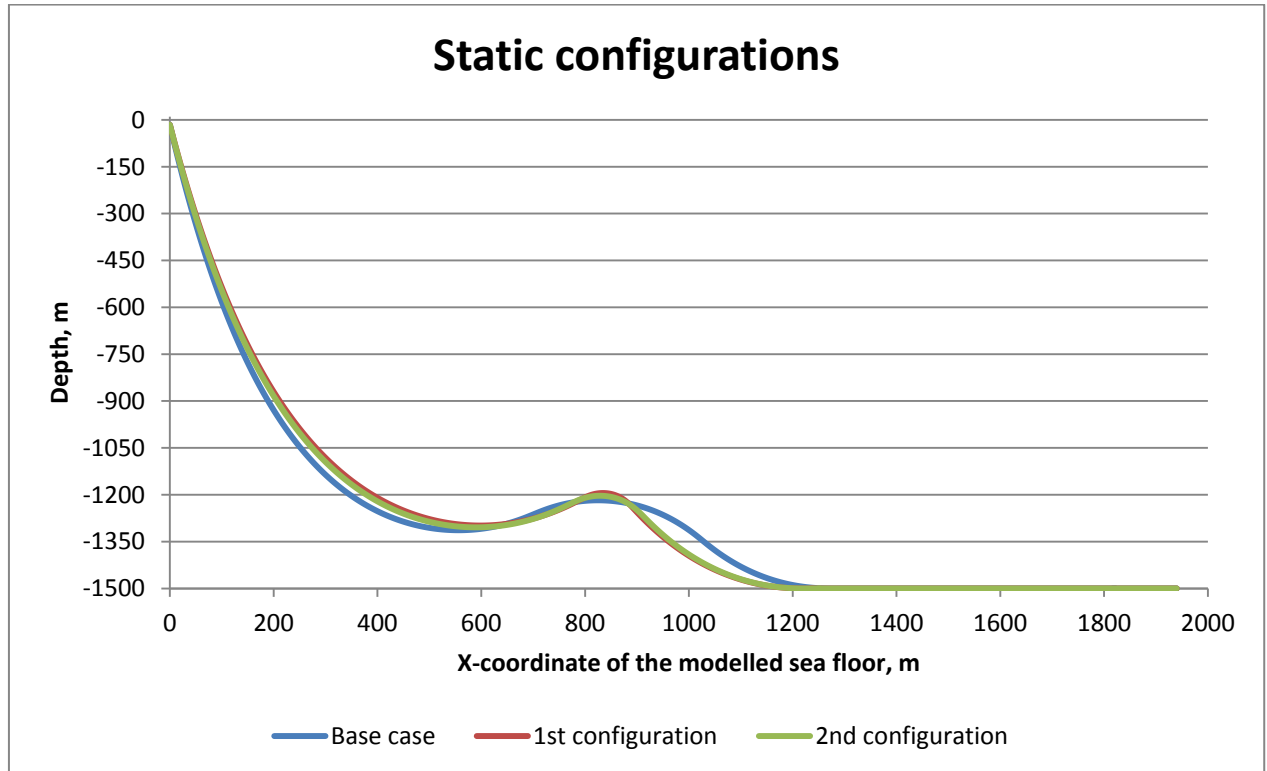


Figure 5.4 Riser static configurations

After the static configurations are similar, the fatigue analysis can be performed (see the next sections).

5.3 Fatigue damage analysis

In this section, the detailed fatigue analysis has been performed for two SLWR configurations obtained in the section above. The main features of this analysis are the following:

- Since the experiment in the SINTEF Ocean Company has been performed for CF motions, only CF hydrodynamic data is available. Thus, the present analysis is performed in pure CF mode;
- Only realistic non-uniform current profiles have been considered in this analysis;
- Both time and space sharing options have been used;
- CF fatigue results have been obtained for all SLWR configurations;
- Fatigue damage comparison (including the probabilities of occurrence) has been made between the 1st, 2nd and the base configurations.

5.3.1 First SLWR configuration

In order to perform the fatigue analysis, the 1st configuration ($L_c/L_b=1$) has been modelled in VIVANA (see Figure 5.5).

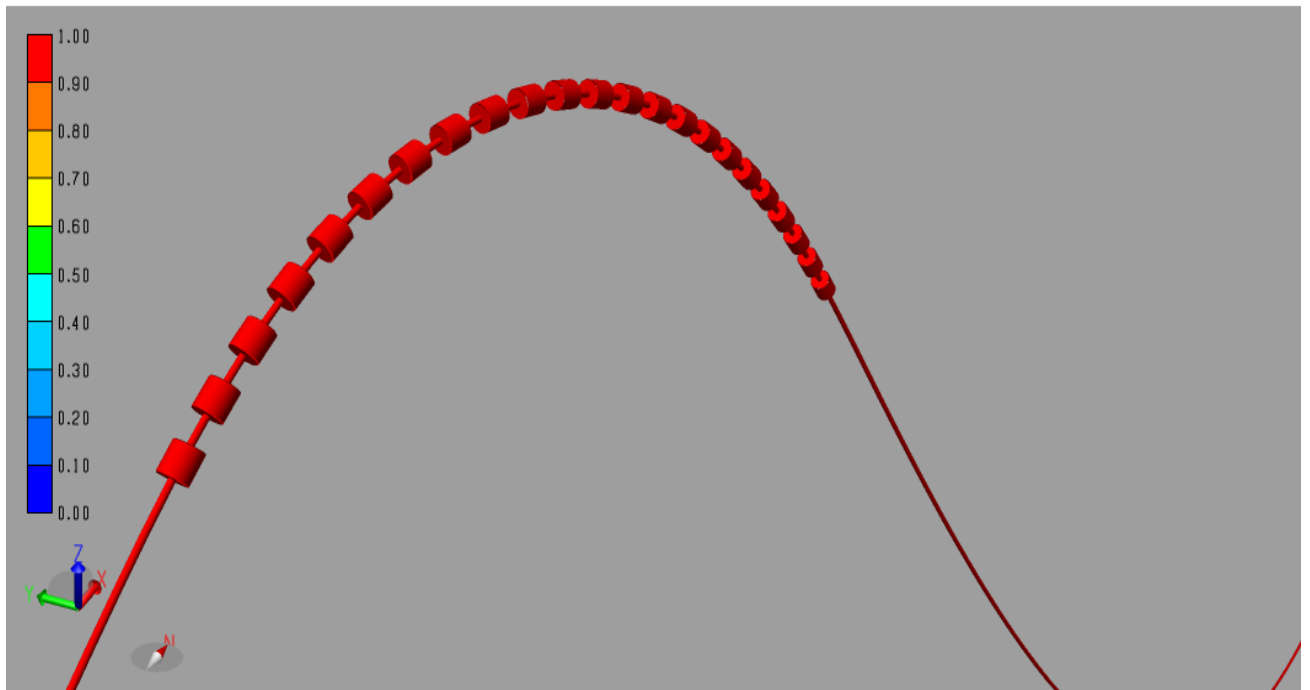


Figure 5.5 The 1st riser configuration modelled in VIVANA

The fatigue damage has been calculated for 21 currents including the probabilities of occurrence. Figure 5.6 illustrates the CF fatigue results against the riser arc length for the space and time sharing. Both options have two prominent peaks in the buoyancy section (absolute maximums) and at TDP. Maximum fatigue damage from the space sharing method is 0.041 1/year and is higher than in the time sharing (0.039 1/year). The bigger TDP fatigue

is also observed in the space sharing case (0.017 1/year), while damage from the time sharing is 0.01 1/year.

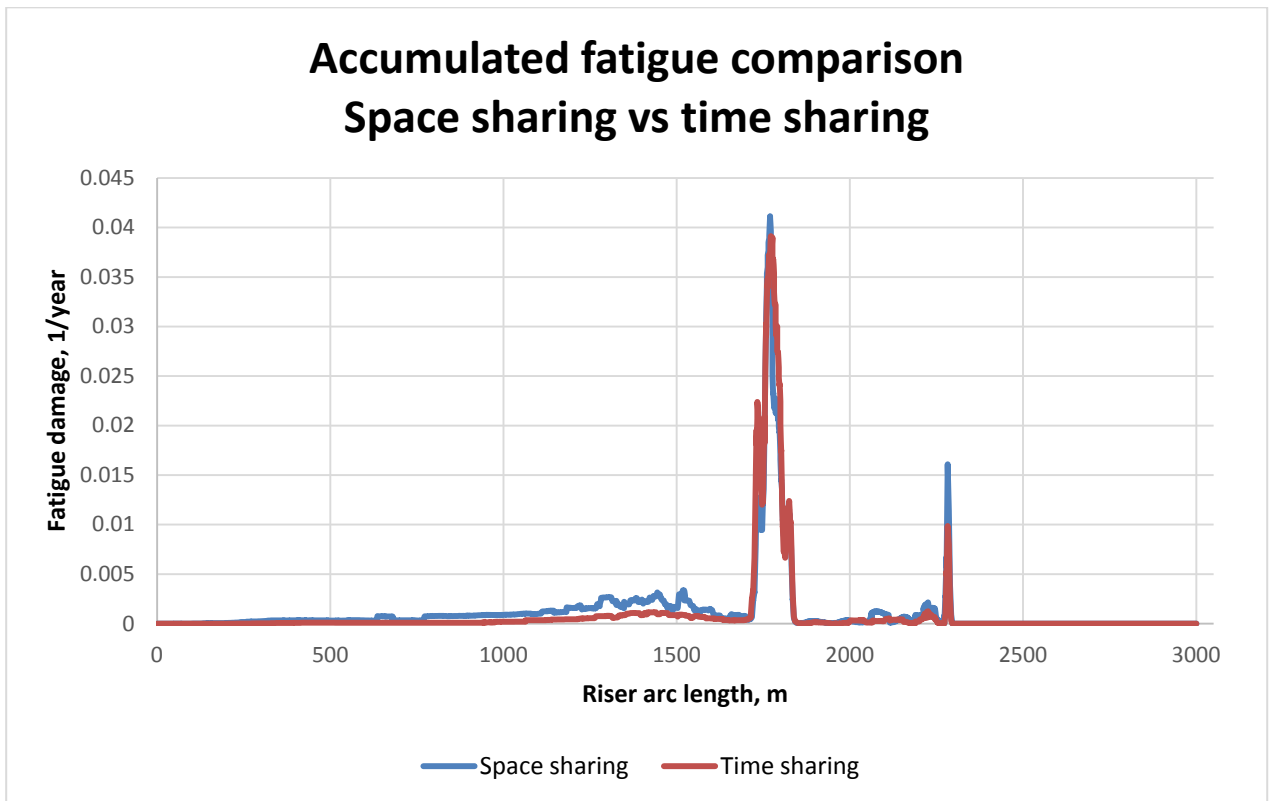


Figure 5.6 Accumulated fatigue damage comparison between the time and space sharing options for the 1st SLWR configuration (including probabilities of occurrence)

Figures 5.7 and 5.8 illustrate the maximum fatigue against cross-section in contrast with maximum current speeds for two options. The same behavior is observed for the both space and time sharing methods. CF fatigue as expected dominates at any current magnitude. Graphs have also showed occurrence of the negligible IL damage even though the analysis has been performed in pure CF motions. Both space and time sharing cases have showed the maximum fatigue damage at the point with current speed 0.75 m/s (2.88 1/year and 2.73 1/year respectively). For clarification, current profiles in this case have been used excluding probabilities of occurrence.

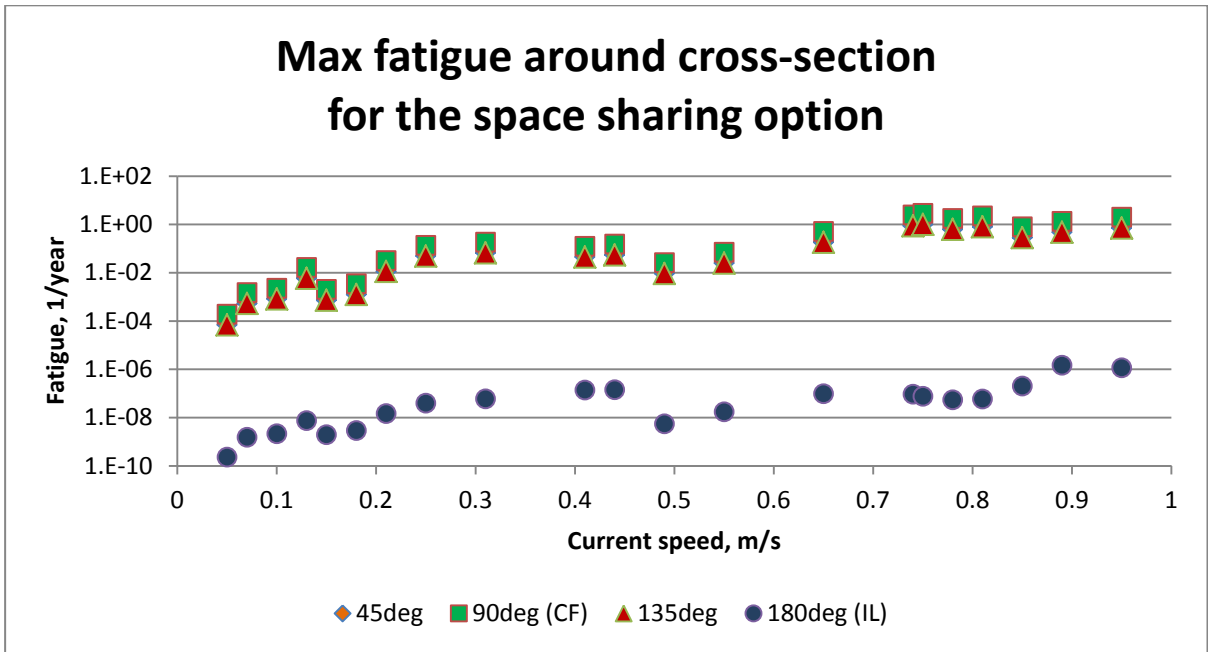


Figure 5.7 Maximum fatigue damage comparison for the 1st configuration using the space sharing method (current are without probabilities of occurrence)

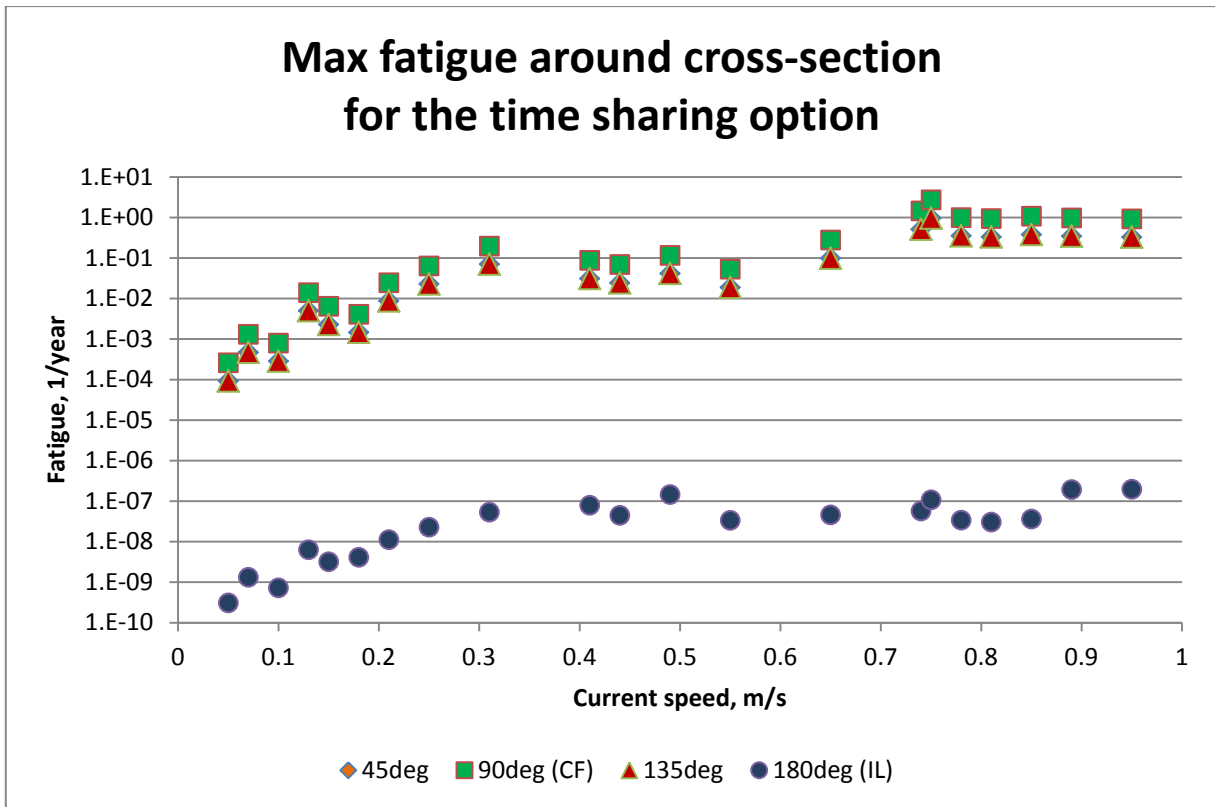


Figure 5.8 Maximum fatigue damage comparison for the 1st configuration using the time sharing method (current are without probabilities of occurrence)

5.3.2 Second SLWR configuration

Figure 5.9 illustrates the 2nd SLWR configuration modelled in VIVANA.

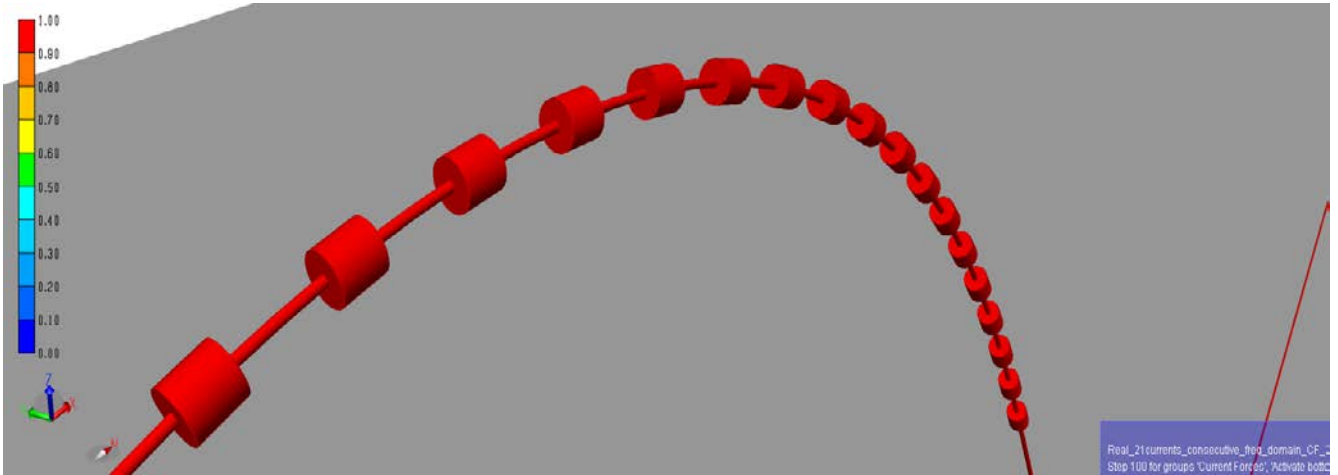


Figure 5.9 The 2nd riser configuration modelled in VIVANA

The fatigue damages have been plotted against the riser arc length for both space and time sharing options (see Figure 5.10). Referring to this figure, the fatigue damage from the space sharing option is approximately 1.7 times larger than the fatigue calculated in the time sharing (in buoyancy section and at TDP). The absolute maximum fatigue for both space and time sharing options is observed in the buoyancy section (0.039 1/year and 0.023 1/year respectively). Fatigue at TDP is 0.017 1/year for the space sharing and 0.01 1/year for the time sharing method.

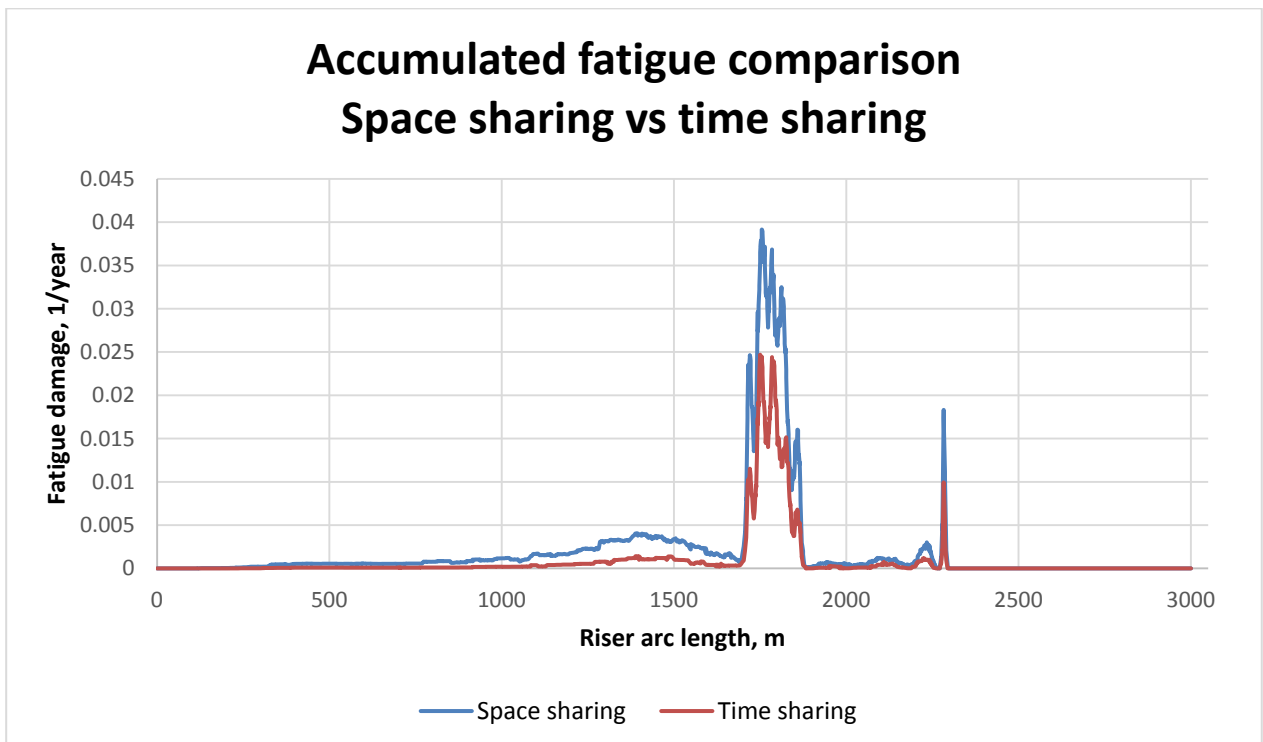


Figure 5.10 Accumulated fatigue damage comparison between the time and space sharing options for the 2nd SLWR configuration (including probabilities of occurrence)

Figures 5.11 and 5.12 show the maximum fatigue damage against the maximum speeds of each current profile. As in the cases with 1st SLWR configuration, CF fatigue damages dominate in each point of the flow speed. Absolute maximum fatigue damage for the space

sharing option is observed at the flow speed of 0.78 m/s and is 2.28 1/year. In the time sharing method, the absolute maximum fatigue corresponds to the flow speed of 0.85 m/s and is 0.7 1/year. It should be noted that the maximum fatigue results for the time sharing option obtained at the flow speeds of 0.81 m/s, 0.85 m/s, 0.89 m/s, 0.95 m/s show quite similar results. This is confusing because the fatigue damage generally increases with increasing flow speed.

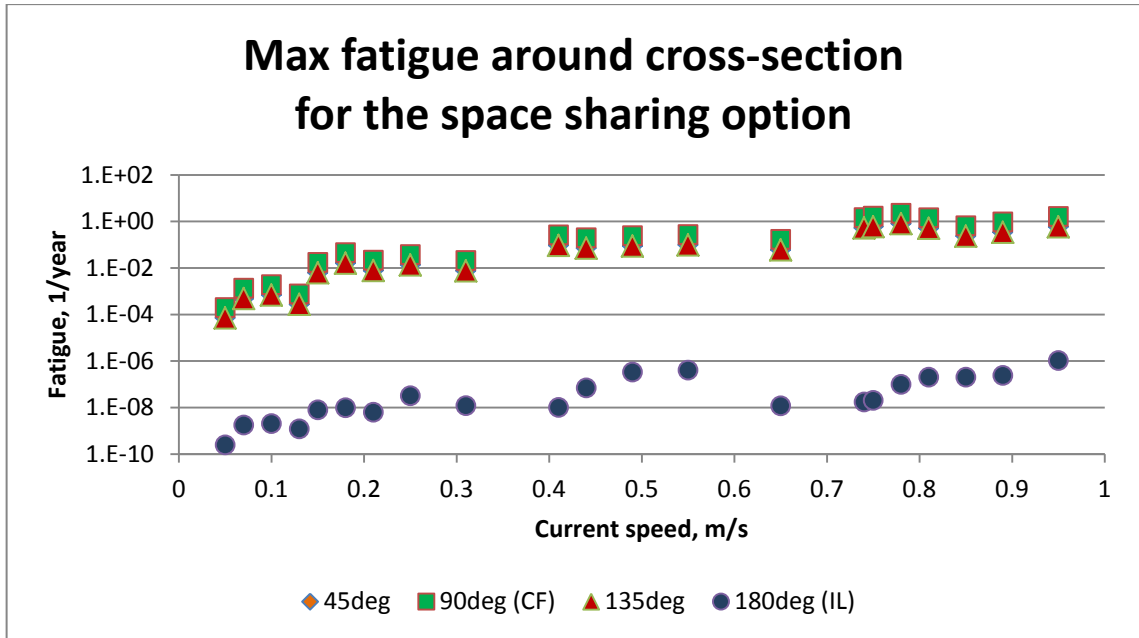


Figure 5.11 Maximum fatigue damage comparison for the 2nd configuration using the space sharing method (current are without probabilities of occurrence)

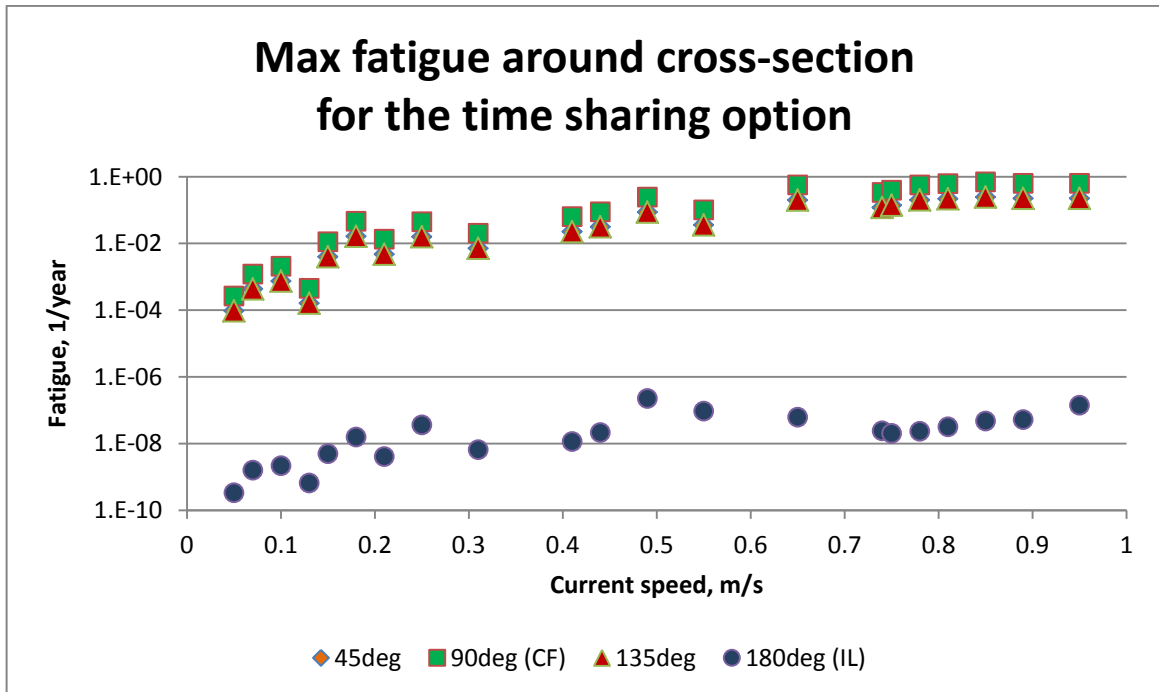


Figure 5.12 Maximum fatigue damage comparison for the 2nd configuration using the time sharing method (current are without probabilities of occurrence)

5.3.3 Fatigue damage comparison

In this section, the fatigue damage comparison has been performed between the base case, 1st and 2nd SLWR configurations. Referring to Figures 4.15, 4.16, 5.6 and 5.10, all necessary data have been summarized in Table 5.4. All presented fatigue data have been obtained including the probabilities of occurrence for each current profile.

Table 5.4 Accumulated CF fatigue damage results

Configuration Parameter	Base case		1 st configuration		2 nd configuration	
	Space sharing	Time sharing	Space sharing	Time sharing	Space sharing	Time sharing
Maximum fatigue damage in the buoyancy section, 1/year	0.016	0.011	0.041 (absolute maximum)	0.039 (absolute maximum)	0.039 (absolute maximum)	0.023 (absolute maximum)
Maximum fatigue damage at TDP, 1/year	0.029 (absolute maximum)	0.017 (absolute maximum)	0.017	0.01	0.017	0.01

Figure 5.13 illustrates comparison between the fatigue damage of the base case, 1st and 2nd configurations obtained in the space sharing option.

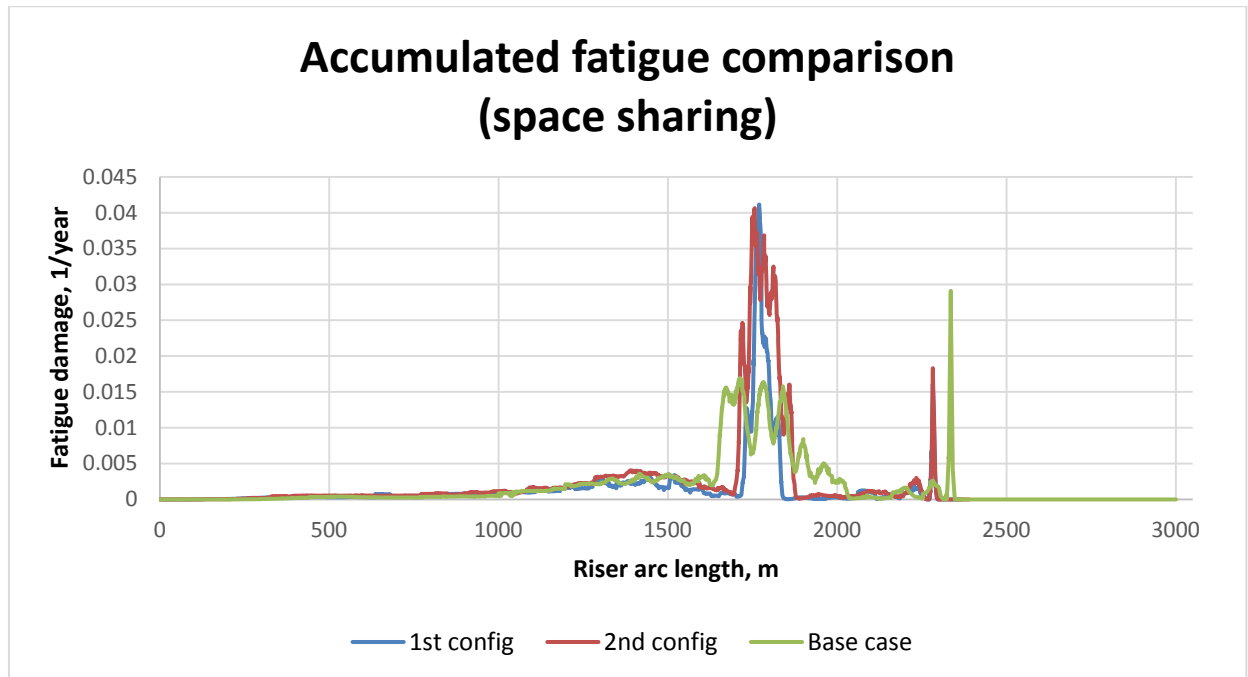


Figure 5.13 CF fatigue damage comparison between the base case, 1st and 2nd SLWR configurations against the riser arc length using the space sharing method

Based on the Figure 5.13, the highest fatigue damage in the buoyancy section is observed in the 1st SLWR configuration. Base case fatigue damage is the smallest in the buoyancy section. However, the maximum fatigue damage at TDP is observed from the base case. The different locations of TDP fatigue peaks between the base case and two SLWR configurations

is due to the difference in the buoyancy section lengths. Longest section belongs to the base case, so TDP is located in the lower part of the riser.

The time sharing option is illustrated in Figure 5.14.

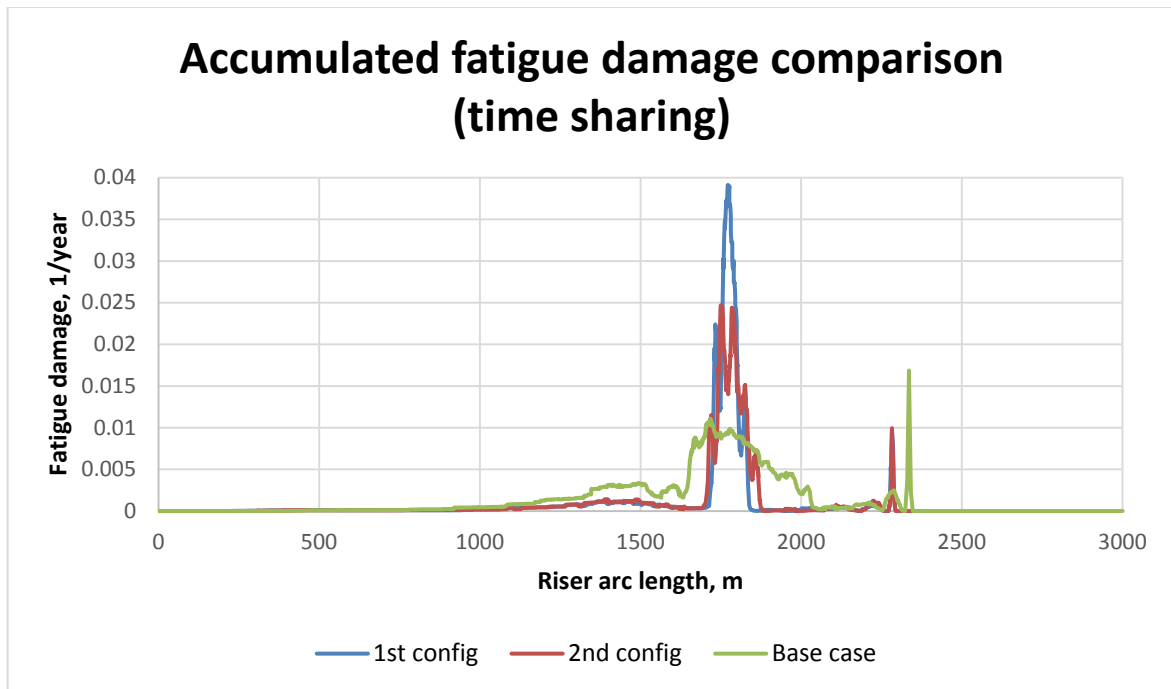


Figure 5.14 CF fatigue damage comparison between the base case, 1st and 2nd SLWR configurations against the riser arc length using the time sharing method

In this case, the maximum fatigue damage in the buoyancy section is observed from the 1st SLWR configuration. The highest TDP fatigue peak is observed from the base case model.

During the sensitivity study, the following key observations have been obtained:

- In the 1st SLWR configuration case, the maximum fatigue damage results against the maximum current speed for both space and time sharing options (see Figures 5.7 and 5.8) showed that the absolute maximum fatigue damage is observed at flow speed of 0.75 m/s (the fatigue damage at maximum flow speed is lower);
- During comparison of the accumulated fatigue damage between the base case, 1st and 2nd SLWR configurations for both space and time sharing options (see Figures 5.13 and 5.14), it has been observed that the maximum fatigue in the buoyancy section belongs to the 1st configuration;
- For both space and time sharing options, the maximum accumulated fatigue damage at TDP is observed for the base case model (see Figures 5.13 and 5.14);
- The CF fatigue damage is generally bigger for the space sharing option.

Chapter 6

Results and discussion

In this chapter, the key findings obtained from the base case analysis (Section 4.2) and from the sensitivity study (Chapter 5) have been thoroughly analyzed and discussed. For more clear explanation, all supporting figures have been attached to confirm the conclusions.

6.1 Discussion of the base case analysis

During the base case analysis, several observations have been made. The key observations are the following:

- 1) For the non-uniform flow, the maximum CF and IL fatigue is observed generally at 90 degrees (CF direction) in both space and time sharing options. However, in the space sharing method, with increasing current speed IL fatigue becomes greater than the CF one (see Figure 4.17);
- 2) In the CF and IL maximum fatigue damage analysis, for both space and time sharing methods, a spontaneous decrease of the maximum fatigue damage is observed in the current profile with the maximum speed of 0.18 m/s (see Figures 4.17 and 4.18).

6.1.1 Increase of the IL fatigue damage

This case has been analyzed in terms of the response frequencies, response amplitudes and mode numbers obtained from VIVANA. Four cases around the maximum flow speed 0.85 m/s have been further investigated in this section. Table 6.1 includes all key data for these cases.

Table 6.1 Key results of selected cases for the analysis (space sharing option)

Current profile number	Max. current speed, m/s	Max. CF response amplitude, m	Dominating CF freq., Hz	Excited CF mode number	Max. IL response amplitude, m	Dominating IL freq., Hz	Excited IL mode number
18	0.81	0.79	0.056	9	0.3	0.111	19
19	0.85	0.22	0.063	10	0.23	0.126	21
20	0.89	0.12	0.063	10	0.26	0.126	22
21	0.95	0.27	0.063	10	0.34	0.126	22

Referring to Table 6.1, at the maximum flow speed of 0.81 m/s, the 9th mode has been excited; the maximum CF response amplitude is bigger than IL one. With increased flow speed, the 10th mode started to dominate causing the significant decrease of the CF response amplitude. However, the maximum IL response amplitude and the IL mode number continued to increase. The maximum response amplitude and mode number correspond to the higher curvature, as shown in the following formula:

$$Curvature = \left(\frac{Mode\ number \cdot \pi}{L} \right)^2 \cdot RMS_{displacement}, \quad (6.1)$$

where L is the riser length, $RMS_{displacement}$ is the root mean square of the displacement, calculated as:

$$RMS_{displacement} = \frac{Max.\ amplitude}{\sqrt{2}}. \quad (6.2)$$

It should be noted that Formulae 6.1 and 6.2 are valid only for the single mode responses (in the present study, the responses are multimodal). However, these equations show the relation between the displacements and curvature and can be used for the particular case as indicators. The curvature is in direct ratio with the fatigue damage (Passano et al., 2014). Thus, with increased maximum IL response amplitude and IL mode number, the maximum fatigue damage is governed by the IL motions.

6.1.2 Influence of the Strouhal number on the response frequency and mode number

As the previous case, this case has been analyzed in terms of the riser's VIV responses. All key parameters have been taken in VIVANA for the space sharing option and summarized in Table 6.2.

Table 6.2 Key analysis results for the space sharing option

Current profile number	Max. current speed, m/s	Max. CF response amplitude, m	Excited mode number	Dominating CF freq., Hz	Max. IL response amplitude, m	Dominating IL freq., Hz	Excited mode number
5	0.15	0.34	7	0.041	0.18	0.027	4
6	0.18	0.7	3	0.019	0.13	0.039	7
7	0.21	0.83	4	0.022	0.15	0.043	8
8	0.25	0.27	12	0.076	0.11	0.057	10

A steep CF mode number decrease is observed for points with the maximum flow speeds 0.18 m/s and 0.21 m/s. The mode number corresponds to the fatigue damage, as it was explained in the first observation. Due to the second power (see Formula 6.1), the influence on fatigue damage is stronger by the mode number than by the response amplitude. Thus, the fatigue

damage values at 90 degrees (CF), 180 degrees (IL) and also at 45 and 135 degrees (as combinations of the CF and IL fatigue) are similar at the point with the flow speed 0.18 m/s (see Figure 4.17).

Such decrease of the mode number is explained by one important observation. Figure 6.1 illustrates the values of the Strouhal number for the first 6 current profiles (with the maximum speeds from 0.05 m/s (1st current profile; the topmost blue curve) to 0.18 m/s (6th current profile; the bottommost yellow curve).

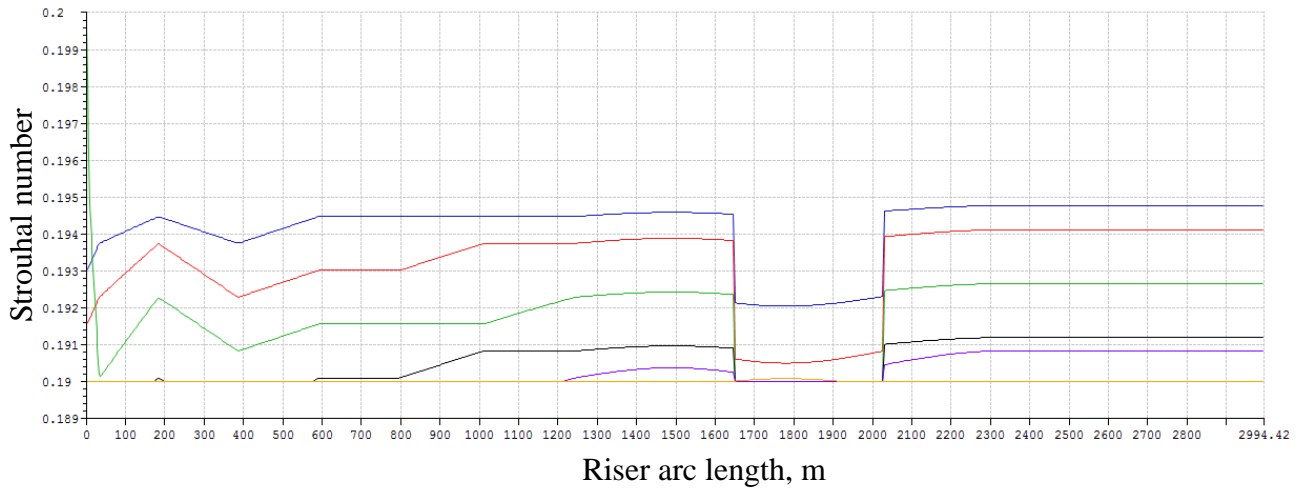


Figure 6.1 Strouhal number values along the riser for first 6 current profiles

In Figure 6.1, the decrease of the Strouhal number is observed from the 1st to the 6th current profile. After the 6th current profile, the behavior of Strouhal number is changed. According to Figure 6.2, from the 7th current profile (the bottommost blue curve; maximum current speed is 0.21 m/s), the value of the Strouhal number increases with increasing current speed. The 21st current profile (maximum current speed is 0.95 m/s) is represented by the topmost green curve.

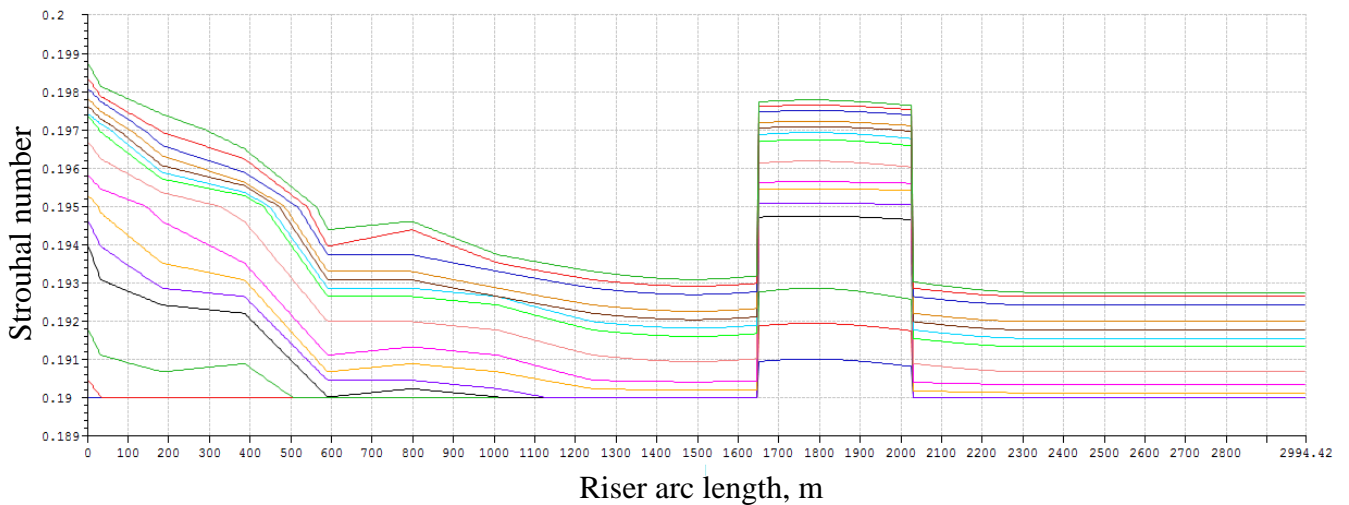


Figure 6.2 Strouhal number values along the riser for points from 7th to the 21st current profile

This phenomenon shows that the Strouhal number is a function of the Reynolds number. For the first 6 cases (see Figure 6.1), with increased current speed the value of the Strouhal number decreases causing lower values of the shedding frequency (see Formula 2.2). Thus, the mode number decrease has been occurred in case with the flow speed 0.18 m/s. Consequently, the maximum fatigue damage has been decreased.

In the time sharing option, similar behavior is observed for the point with the flow speed 0.18 m/s. Thus, the maximum fatigue damage decrease can be explained by the same principle as in the space sharing option.

6.2 Discussion of the sensitivity study

During the sensitivity study, several findings have been made. The following key observations have been analyzed in this section:

- 1) In the 1st SLWR configuration case, the maximum fatigue damage results against the maximum current speed for both space and time sharing options (see Figures 5.7 and 5.8) showed that the absolute maximum fatigue damage is observed at flow speed of 0.75 m/s (the fatigue damage at maximum flow speed is lower);
- 2) During comparison of the accumulated fatigue damage between the base case, 1st and 2nd SLWR configurations, for both space and time sharing options (see Figures 5.12 and 5.13), it has been observed that the maximum fatigue in the buoyancy section belongs to the 1st configuration;
- 3) For both space and time sharing options, the maximum accumulated fatigue damage at TDP is observed for the base case model (see Figures 5.12 and 5.13).

6.2.1 Maximum fatigue damage variations

In this analysis, the key results have been taken from VIVANA for both space and time sharing options. For the space sharing method, four cases with the maximum flow speeds 0.74 m/s, 0.75 m/s, 0.78 m/s and 0.95 m/s have been considered (Table 6.3). For the time sharing option, two cases with the flow speeds 0.75 m/s and 0.95 m/s have been investigated in the present analysis (Table 6.4).

Table 6.3 VIV data for the analysis (space sharing option)

Current profile number	Max. current speed, m/s	Max. CF response amplitude, m	Excited mode number	Dominating CF freq., Hz	The amount of the excitation frequencies along the riser
15	0.7	0.31	18	0.128	8
16	0.7	0.29	19	0.136	1
17	0.7	0.30	20	0.142	7
21	0.9	0.32	22	0.162	9

Table 6.4 VIV data for the analysis (time sharing option)

Current profile number	Max. current speed, m/s	Max. CF response amplitude, m	Excited mode number	Dominating CF freq., Hz	The amount of the excitation frequencies along the riser
16	0.75	0.313	17	0.121	4
21	0.95	0.327	22	0.162	19

Referring to Tables 6.3 and 6.4, cases with the maximum current speed 0.75 m/s have the smallest amount of the excitation frequencies. As it has been observed from Figures 5.13 and 5.14, the maximum fatigue damage for the 1st SLWR configuration for both options is located in the buoyancy zone. Since the cases with 0.75 m/s have the biggest fatigue damage for both the space and time sharing options, it means that the dominating frequencies have excited the most critical parts of the riser (in the buoyancy section). The frequencies from other cases have excited less critical parts of the riser. Thus, the fatigue damage calculated at the point 0.75 m/s is the highest.

6.2.2 Maximum fatigue in the buoyancy section and at TDP

For the space and time sharing options, the maximum fatigue damage in the buoyancy section belongs to the 1st SLWR configuration; the base case model has showed the highest fatigue damage at TDP (see Figures 5.13 and 5.14).

In order to perform the present analysis, the stress amplitudes data have been taken from VIVANA for all 21 current profiles. Considering the probabilities associated with each current profile, the stress amplitudes have been calculated for both space and time sharing methods. Obtained results have showed that for both space and time sharing options, the maximum stress amplitudes in the buoyancy section and at TDP are observed from the 1st configuration and the base case respectively. The stress amplitudes are in the direct ratio to the fatigue damage (Passano et al., 2014). Thus, the riser model corresponded with larger stress amplitudes will show a larger fatigue damage.

Chapter 7

Conclusion and recommendations for future work

This master's thesis is devoted to VIV investigation of different SLWR configurations including the elastic spring soil model. The present work has been performed using the two options: space sharing and time sharing. There is an uncertainty in determination of the frequency behavior around the structure and in time. Thus, the two different options have been used for the excitation zone identification. Both of them are sort of simplifications based on the structure's responses observed from experiments. So, the main purpose of using the space and time sharing methods is to evaluate the sensitivity of the fatigue damage results for each option. Thus, the following observations have been made during the present work:

- Generally, the space sharing option shows the higher fatigue results than the time sharing option;
- The fatigue damage peak at TDP is relatively more significant for the time sharing option;
- In the analysis with combined CF and IL motions, the CF fatigue damage primarily dominates for the time sharing option;
- In the CF and IL fatigue analysis using the space sharing method, for lower current speeds (from 0.05 m/s to 0.8 m/s), the CF fatigue damage is primarily dominates. However, with increased flow speed (> 0.8 m/s), the IL fatigue damage starts to dominate.

In order to investigate the fatigue performance, the 1st and 2nd SLWR configurations with staggered buoyancy elements have been modelled in VIVANA software and compared to the SLWR configuration from the base case. The length of the buoyancy section of both SLWR configurations with staggered buoyancy elements has been adjusted to have similar static shape with the base case model. The analysis results have shown a decrease of the fatigue damage peak at TDP for both configurations compared to the base case. However, the fatigue damage in the buoyancy section is much higher for both 1st and 2nd configurations causing less riser fatigue life. Such peak is governed by the high concentration of the bending stresses in the buoyancy section due to its relatively small bending radius. Consequently, both SLWR configurations with staggered buoyancy elements based on the base case model have shown degraded fatigue performance and should be modified.

The base case VIV analyses including combined CF and IL motions have shown the domination of the fatigue damage calculated at 45 and 135 degrees and the IL fatigue damage (mostly for the uniform flow but also at some points of the sheared flow) which agrees well with the observation of Baarholm et al. (2006). It may be concluded that for long risers, the maximum fatigue damage may be observed from the IL responses or from the combination of the CF and IL responses.

In the present work, the fatigue damage comparison between SLWR configurations has been performed in pure CF motions since the only CF hydrodynamic data have been obtained from experiment at the SINTEF Ocean Company.

Based on the experience from the present analyses, the following recommendations are proposed for further research:

- In order to obtain total hydrodynamic forces acting on the riser, the VIV analysis should be performed including all hydrodynamic data for both CF and IL motions;
- In order to obtain more realistic model, different riser-soil interaction models can be considered in the analysis, e.g. the model with spring and damper which includes non-linear soil effects;
- In order to obtain the optimal fatigue performance, different staggered buoyancy element configurations can be considered, including:
 - Different spacing ratio, L_c/L_b ;
 - Different aspect ratio, L_b/D_b ;
 - Different lengths of the buoyancy section;
 - Different buoyancy element materials;
- The VIV suppression devices such as strakes, fairings, shrouds, etc. can be used in the analysis to achieve longer fatigue life;
- To take into consideration the effect of the Reynolds number since it affects the mode number, response frequency, response amplitude and, as a result, the fatigue damage (Swithenbank et al., 2008).

References

- Achenbach, E., Heinecke, E. (1981). On vortex shedding from smooth and rough cylinders in the range of Reynolds number 6×10^3 to 5×10^6 . *Journal Fluid Mechanics*, (pp. 109, 239–251).
- Aronsen, K. H. (2007). An experimental investigation of in-line and combined in-line and cross-flow vortex induced vibrations. (2007:253), Norwegian University of Science and Technology, Faculty for Engineering Science and Technology, Marine Technology, Trondheim.
- Baarholm, G.S., Larsen, C.M., and Lie, H. (2006). On fatigue damage accumulation from in-line and cross-flow vortex-induced vibrations on risers, *Journal of Fluid and Structures*, 22, 109-127.
- Blevins, R.D. (1990). *Flow-Induced Vibration*. Krieger Publishing Company, Krieger drive, Florida, USA.
- Braaten, H. and Lie, H. (2005). NDP Riser High Mode VIV Tests Main Report. Norwegian Marine Technology Research Institute, Trondheim, Norway.
- Chakrabarti, S.K. (2005). *Handbook of offshore engineering*. Volume 2. Offshore Structure Analysis, Inc., Plainfield, Illinois, USA.
- Cheng, J., and Cao, P. (2013): Design of Steel Lazy Wave Riser for Disconnectable FPSO. Offshore Technology Conference, Houston, Texas, USA.
- Dahl, J. M. (2008). Vortex induced vibrations of a circular cylinder with combined in-line and cross-flow motions. PhD thesis, Massachusetts Institute of Technology, Cambridge, MA, USA.
- Gopalkrishnan, R. (1993). Vortex-Induced Forces on Oscillating Bluff Cylinders. PhD thesis, Department of Ocean Engineering, Massachusetts Institute of Technology, Cambridge, MA, USA.
- Huang, K., and Chen, H.-C. (2007): Riser VIV Analysis by a CFD Approach. International Offshore and Polar Engineering Conference, Lisbon, Portugal.
- Jauvtis, N., and Williamson, C.H.K. (2004). The effect of two degrees of freedom on vortex-induced vibration at low mass and damping. *Journal of Fluid Mechanics*, vol. 509, 23 - 62.
- Jhingran, V., Zhang, H.P., Lie, H., Braaten, H., and Vandiver, J.K. (2012): Buoyancy Spacing Implications for Fatigue Damage due to Vortex-Induced Vibrations on a Steel Lazy Wave Riser (SLWR). Offshore Technology Conference, OTC23672, Houston, USA.
- Kenny, J. P. (1993). Structural analysis of pipeline spans. Offshore Technology Information, HMSO.
- Larsen, C.M., Vandiver, J.K., Vikestad, K. and Lie, H. (1997). Vortex Induced Vibrations of Long Marine Risers - Experimental Investigations of Multi-Frequency Response, BOSS, pp. 455-468.
- Larsen, C. M., Koushan, K. and Passano, E. (2002). Frequency and time domain analysis of vortex induced vibrations for free span pipelines. OMAE02-28064, 21st International Conference on Offshore Mechanics and Arctic Engineering, Oslo.

- Larsen, C.M., and Passano, E. (2006): Time and frequency domain analysis of catenary risers subjected to vortex induced vibrations. OMAE 2006-92149, Hamburg.
- Larsen, C. M. (2011). VIV-A short incomplete introduction to fundamental concepts. Retrieved from Trondheim, Norway.
- Li., S., and Nguyen., C. (2010). Dynamic Response of Deepwater Lazy-Wave Catenary Riser. Paper presented at the Deep Offshore Technology International, Amsterdam, Netherlands.
- Li, M., Chen, W., and Zhang, L. (2011): A Finite Element Study of Multi-Mode VIV of Slender Riser Experiencing Non-Uniform Flow. 30th International Conference on Ocean, Offshore and Arctic Engineering OMAE2011-49296, Rotterdam, Netherlands.
- Lie, H., Braaten, H., Jhingran, V., Sequeiros, O., Vandiver, K. (2012): Comprehensive riser VIV model tests in uniform and sheared flow. 31st International Conference on Ocean, Offshore and Arctic Engineering OMAE2012, Rio de Janeiro, Brazil.
- Lienhard, I. H. (1966). Synopsis of lift, drag and vortex frequency data for rigid circular cylinders. Washington State University, College of Engineering, Research Division Bulletin 300.
- Link: <https://en.bardotgroup.com/collections/surf-packages-a-global-offer-epc>.
- Passano, E., Larsen, C.M., Lie, H., and Wu, J. (2014): VIVANA - Theory Manual Version 4.4.
- Rao, Z., Vandiver, J. K., and Jhingran, V. (2015). Vortex induced vibration excitation competition between bare and buoyant segments of flexible cylinders. *Ocean Engineering*, 94, 186-198.
- Sarpkaya , T. (1978). Fluid forces on oscillating cylinders. *ASCE Journal of Waterways, Port, Coastal and Ocean Division* 104, pp. 275-290.
- Shi, C., Manuel, L., Tognarelli, M. A., and Botros, T. (2010). On the vortex-induced vibration response of a model riser and location of sensors for fatigue damage prediction. *Proceedings of the 29th International Conference on Ocean, Offshore and Arctic Engineering, OMAE2010-20991*, Shanghai, China.
- Soni, P.K. (2008). On the Interaction between Inline and Cross-flow Vortex Induced Vibrations. PhD thesis, CeSOS/Department of Marine Technology, NTNU, Trondheim, Norway.
- Sumer, B. M. and Fredsøe, J. (2006). *Hydrodynamics around cylindrical structures* (Rev. ed. Vol. 26). New Jersey: World Scientific.
- Swithenbank, S. B., Larsen, C. M., Vandiver, J. K. and Lie, H. (2008). Reynolds number dependence of flexible cylinder VIV response data (Vol. 5, pp. 503-511).
- Trim, A. D., Braaten, H., Lie, H. and Tognarelli, M. A. (2005). Experimental Investigation of Vortex Induced Vibration of long Marine Risers. *Journal of Fluids and Structures*, (Vol. 21, pp. 335-361).
- Vandiver, J.K., Jong, J.-Y. (1987): The relationship between in-line and cross-flow vortex-induced vibration of cylinders, *Journal of Fluid Structures*, 281-299.
- Vikestad, K. (1998). Multi-frequency response of a cylinder subjected to vortex shedding and support motions. Ph.D. thesis, Faculty of Marine Technology, NTNU, Trondheim.
- Wu, J., Lekkala, M. R. and Ong, M. C. (2016). Prediction of riser VIV with staggered buoyancy elements. Paper presented at the International Conference on Ocean, Offshore and Arctic Engineering OMAE2016, Busan, Korea.

- Wu, J., Lie, H., Constantinides, Y., Baarholm, R. (2016): NDP riser VIV model test with staggered buoyancy elements. 35th International Conference on Ocean, Offshore and Arctic Engineering, OMAE2016-54503, Busan, South Korea.
- Wu, J., Lie, H., Fu, S., Baarholm, R., Constantinides, Y. (2017). VIV responses of riser with buoyancy elements: forced motion test and numerical prediction. 36th International Conference on Ocean, Offshore and Arctic Engineering, OMAE2017-61768, Trondheim, Norway.
- Yin, D. (2013). Experimental and Numerical Analysis of Combined In-line and Cross-flow Vortex Induced Vibrations. PhD thesis, Department of Marine Technology, NTNU, Trondheim, Norway.

Appendix

Appendix A. Input files

The following VIVANA input files (.stask files) have been used in the present work:

- Space_sharing_sheared_1st_config_pureCF;
- Space_sharing_sheared_2nd_config_pureCF;
- Space_sharing_sheared_base_case_CFandIL;
- Space_sharing_sheared_base_case_pureCF;
- Space_sharing_uniform_1st_config_pureCF;
- Space_sharing_uniform_2nd_config_pureCF;
- Space_sharing_uniform_base_case_CFandIL;
- Space_sharing_uniform_base_case_pureCF;
- Time_sharing_sheared_1st_config_pureCF;
- Time_sharing_sheared_2nd_config_pureCF;
- Time_sharing_sheared_base_case_CFandIL;
- Time_sharing_sheared_base_case_pureCF;
- Time_sharing_uniform_1st_config_pureCF;
- Time_sharing_uniform_2nd_config_pureCF;
- Time_sharing_uniform_base_case_CFandIL;
- Time_sharing_uniform_base_case_pureCF.

For example, the file Space_sharing_sheared_2nd_config_pureCF means:

- Analysis is made using the space sharing option;
- Sheared current profiles have been used;
- Analysis is made for the 2nd SLWR configuration with staggered buoyancy elements;
- Only pure CF motions have been considered in this analysis.

All for VIVANA input files have been uploaded on the flash drive and given to my supervisors.

Appendix B. Working files

VIVANA interface screenshots have been made for all riser models. They include all types of data used in this program. Apart from that, the Excel files containing key data for all graphs made in the present work have been prepared. These files have been also given to my supervisors.

Appendix C. Hydrodynamic data

In this section, all hydrodynamic data for the riser models performed in thesis is presented. For all cases, only CF hydrodynamic data is used. The CF and IL analysis for the base case has been made with default hydrodynamic parameters in VIVANA.

Water temperature for all cases is 20 °C. Table C.1 includes excitation zone properties for the base case, 1st and 2nd SLWR configurations.

Table C.1 Excitation zone properties

Configuration \ Parameter	Sections	Minimum non-dimensional frequency	Maximum non-dimensional frequency
Base case	Bare/Buoyancy	0.125	0.3
1 st configuration	Bare	0.16	0.22
	Buoyancy	0.06	0.12
2 nd configuration	Bare	0.16	0.22
	Buoyancy	0.001*	0.002*

* Since the buoyancy section in the 2nd configuration is always in damping (Wu et al., 2017), small range of non-dimensional frequency has been taken to prevent positive excitation

Table C.2 represents the added mass properties for all riser models.

Table C.2 Added mass properties

Configuration \ Parameter	Sections	Non-dimensional frequency	Added mass coefficient
Base case	Bare/Buoyancy	0.02	1
		1.0	1
1 st configuration	Bare	0.16	10
		0.22	10
	Buoyancy	0.06	2
		0.12	2
	Bare riser parts outside the buoyancy section	0.02	1
1.0		1	
2 nd configuration	Bare	0.16	10
		0.22	10
	Buoyancy	0.001*	2
		0.002*	2
	Bare riser parts outside the buoyancy section	0.02	1
		1.0	1

* Since the buoyancy section in the 2nd configuration is always in damping (Wu et al., 2017), small range of non-dimensional frequency has been taken to prevent positive excitation

Table C.3 represents the excitation coefficient properties for the base case.

Table C.3 Excitation coefficient properties for the base case

Non-dimensional frequency	A/D ratio for $C_e=0$	A/D ratio for $C_e=C_e \text{ max}$	$C_e \text{ max}$	C_e for A/D=0
0.12	0.2	0.1	0.1	0.05
0.125	0.4	0.2	0.1	0.06
0.135	0.5	0.27	0.1	0.08
0.14	0.55	0.35	0.14	0.11
0.15	0.6	0.45	0.2	0.18
0.16	0.7	0.5	0.35	0.24
0.165	0.8	0.5	0.5	0.3
0.17	0.9	0.43	0.8	0.4
0.175	0.82	0.4	0.7	0.2
0.18	0.78	0.4	0.5	0.15
0.185	0.75	0.4	0.55	0.16
0.19	0.65	0.4	0.6	0.17
0.2	0.58	0.38	0.65	0.2
0.21	0.55	0.35	0.6	0.25
0.25	0.4	0.2	0.35	0.2
0.3	0.2	0.1	0.2	0.15
0.31	0.18	0.09	0.1	0.15

Tables C.4 and C.5 represent the excitation coefficient properties for the bare and buoyancy parts of the 1st configuration respectively.

Table C.4 Excitation coefficient properties for the bare part of the 1st configuration

Non-dimensional frequency	A/D ratio for $C_e=0$	A/D ratio for $C_e=C_e \text{ max}$	$C_e \text{ max}$	C_e for A/D=0
0.16	0.65	0.299	0.47	0.3
0.17	0.65	0.299	0.47	0.3
0.18	0.65	0.299	0.47	0.3
0.19	0.65	0.299	0.47	0.3
0.2	0.65	0.299	0.47	0.3
0.21	0.65	0.299	0.47	0.3
0.22	0.65	0.299	0.47	0.3

Table C.5 Excitation coefficient properties for the buoyancy part of the 1st configuration

Non-dimensional frequency	A/D ratio for $C_e=0$	A/D ratio for $C_e=C_e \text{ max}$	$C_e \text{ max}$	C_e for A/D=0
0.06	0.0981	0.695	0.1571	0.0
0.07	0.0981	0.695	0.1571	0.0
0.08	0.0981	0.695	0.1571	0.0
0.09	0.0981	0.695	0.1571	0.0
0.1	0.0981	0.695	0.1571	0.0
0.11	0.0981	0.695	0.1571	0.0
0.12	0.0981	0.695	0.1571	0.0

Tables C.6 and C.7 represent the excitation coefficient properties for the bare and buoyancy parts of the 2nd configuration respectively.

Table C.6 Excitation coefficient properties for the bare part of the 2nd configuration

Non-dimensional frequency	A/D ratio for $C_e=0$	A/D ratio for $C_e=C_e \text{ max}$	$C_e \text{ max}$	C_e for A/D=0
0.16	0.65	0.299	0.47	0.3
0.17	0.65	0.299	0.47	0.3
0.18	0.65	0.299	0.47	0.3
0.19	0.65	0.299	0.47	0.3
0.2	0.65	0.299	0.47	0.3
0.21	0.65	0.299	0.47	0.3
0.22	0.65	0.299	0.47	0.3

Table C.6 Excitation coefficient properties for the buoyancy part of the 2nd configuration

Non-dimensional frequency	A/D ratio for $C_e=0$	A/D ratio for $C_e=C_e \text{ max}$	$C_e \text{ max}$	C_e for A/D=0
0.001*	0.0981	0.695	0.1571	0.0
0.002*	0.0981	0.695	0.1571	0.0
* Since the buoyancy section in the 2 nd configuration is always in damping region (Wu et al., 2017), small range of non-dimensional frequency has been taken to prevent positive excitation				

For all cases considered in the present work, hydrodynamic damping properties, Strouhal number properties and IL hydrodynamic coefficients have been taken default in VIVANA.

Appendix D. Current data

In this section, the current data used in the present work are presented. Both uniform flow and the realistic current profiles have been used for the analyses. Each current profile has an associated probability of occurrence.

The uniform flow speed 0,4 m/s has been used for all uniform flow analyses. Table D.1 represents 21 current profiles.

Table D.1 Realistic current profiles

Probability of occurrence	Water depth, m	-20	-50	-200	-400	-600	-800	-1000	-1200	-1500
	Current profile									
0.075	1	0.05	0.04	0.03	0.04	0.03	0.03	0.03	0.03	0.026
0.075	2	0.07	0.06	0.04	0.06	0.05	0.05	0.04	0.04	0.035
0.1	3	0.11	0.09	0.06	0.08	0.07	0.07	0.07	0.06	0.055
0.1	4	0.13	0.11	0.09	0.11	0.09	0.09	0.08	0.08	0.075
0.1	5	0.15	0.14	0.11	0.13	0.11	0.11	0.1	0.09	0.08
0.1	6	0.18	0.16	0.14	0.16	0.13	0.13	0.12	0.11	0.1
0.1	7	0.21	0.19	0.17	0.19	0.15	0.15	0.14	0.13	0.12
0.1	8	0.25	0.23	0.21	0.22	0.17	0.17	0.16	0.15	0.14
0.1	9	0.31	0.28	0.26	0.27	0.2	0.2	0.19	0.17	0.155
0.06	10	0.41	0.37	0.34	0.33	0.23	0.24	0.23	0.21	0.205
0.02	11	0.44	0.41	0.36	0.35	0.25	0.25	0.24	0.22	0.215
0.02	12	0.49	0.45	0.39	0.37	0.26	0.27	0.26	0.24	0.235
0.02	13	0.55	0.51	0.44	0.39	0.28	0.29	0.28	0.25	0.245
0.015	14	0.65	0.6	0.5	0.44	0.32	0.32	0.31	0.28	0.26
0.005	15	0.74	0.68	0.54	0.49	0.35	0.35	0.34	0.31	0.29
0.002	16	0.75	0.71	0.56	0.5	0.36	0.36	0.35	0.32	0.3
0.002	17	0.78	0.73	0.58	0.52	0.37	0.37	0.35	0.33	0.31
0.002	18	0.81	0.76	0.61	0.53	0.38	0.38	0.36	0.34	0.32
0.0015	19	0.85	0.8	0.64	0.56	0.4	0.4	0.38	0.36	0.34
0.00075	20	0.89	0.82	0.68	0.6	0.41	0.43	0.39	0.37	0.35
0.00075	21	0.95	0.86	0.75	0.63	0.43	0.44	0.4	0.38	0.355